Properties and Sensor Performance of Zinc Oxide Thin Films

by

Yongki Min

B.S. Metallurgical Engineering
Yonsei University, 1988
M.S. Metallurgical Engineering
Yonsei University, 1990

Submitted to the Department of Materials Science and Engineering
in Partial Fulfillment of the Requirements for the Degree of

Doctor of Philosophy in Electronic, Photonic, and Magnetic Materials
at the

Massachusetts Institute of Technology
September 2003

© 2003 Massachusetts Institute of Technology
All rights reserved

Signature of Author: ______________________________
Department of Materials Science and Engineering
August 21, 2003

Certified by: ______________________________
Harry L. Tuller
Professor of Ceramics and Electronic Materials
Thesis Advisor

Accepted by: ______________________________
Harry L. Tuller
Professor of Ceramics and Electronic Materials
Chairman, Committee for Graduate Students

Properties and Sensor Performance of Zinc Oxide Thin Films

by

Yongki Min

Submitted to the Department of Materials Science and Engineering on August 21, 2003
in Partial Fulfillment of the Requirements for the Degree of Doctor of Philosophy
in Electronic, Photonic and Magnetic materials

ABSTRACT

Reactively sputtered ZnO thin film gas sensors were fabricated onto Si wafers. The atmosphere dependent electrical response of the ZnO micro arrays was examined. The effects of processing conditions on the properties and sensor performance of ZnO films were investigated. Using AFM, SEM, XRD and WDS, the O_2/Ar ratios during sputtering and Al dopant were found to control the property of ZnO films. Subsequent annealing at 700 °C improved the sensor response of the films considerably although it had only minor effects on the microstructure. DC resistance, I-V curves and AC impedance were utilized to investigate the gas response of ZnO sensors.

ZnO films prepared with high O_2/Ar ratios showed better sensitivity to various gases, a feature believed to be related to their lower carrier density. Al doped ZnO showed measurable sensitivity even with lower resistance attributable to their porous microstructure. AC impedance identified two major components of the total resistance including Schottky barriers at the Pt-ZnO interfaces and a DC bias induced constriction resistance within the ZnO films.

Time dependent drift in resistance of ZnO films has been observed. Without applied bias, the ZnO films showed a fast and a slow resistance change response when exposed to gases with varying oxygen partial pressure with both response components dependent on operating temperature. Even at the relatively low operating temperatures of these thin film sensors, bulk diffusion cannot be discounted. The oxygen partial pressure dependence of the sensor resistance and its corresponding activation energy were related to defect process controlling the reduction/oxidation behavior of the ZnO.

In this study, time dependent DC bias effects on resistance drift were first discovered and characterized. The DC bias creates particularly high electric fields in these micro devices given that the spacing of the interdigited electrodes falls in the range of microns. The high electric field is believed to initiate ion migration and/or modulate grain boundary barrier heights, inducing resistance drift with time. Such DC bias resistance induced drift is expected to contribute to the instability of thin film micro array sensors designed for practical applications. Suggestions for stabilizing sensor response are provided.

Thesis Supervisor: Harry L. Tuller
Title: Professor of Ceramics and Electronic Materials

Acknowledgments

I would like to express my special gratitude and appreciation to my thesis advisor, Professor Harry L. Tuller. Without his insightful guidance and encouragement, this thesis would never have been accomplished. He has been always with me, giving a lot of help with his cordial heart.

I appreciate Professor Martin A. Schmidt, Professor Caroline A. Ross and Professor Richard L. Smith for comments and suggestions for improving my thesis work.

I also thank the other members of the Tuller group including Tsachi, Todd, Huankiat, Dilan, Josh and Scott, for their friendship and collaboration. They made my life at MIT enjoyable.

I am grateful to Dr. Jürgen Wöllenstein at Fraunhofer Institute Physical Measurement Techniques for providing me with the micro array sensor platform and cooperating thin film sensor research. Many individuals have provided valuable technical discussion and assistance, including Dr. Jürgen Fleig, Dr. Avner Rothschild, and Dr. Il-Doo Kim.

Most of all, I would like to special thank my family for their endless support. My parents are always giving me courage with their love. I also appreciate my mother-in-law for her support. Next, I am expressing my gratitude to my sisters and brother. I extend my thanks to my wife, Seungwan, and my beloved boys, Kyungjei and Kyungkyu. Without them, this thesis would never have come to fruition.

This work was supported by NSF-DMR-0228787

Biographical Note

Education

2003 - Ph.D., Materials Science and Engineering, MIT, Cambridge, MA, USA
Thesis title: Properties and Sensor Performance of Zinc Oxide Thin Films
1990 - M.S., Metallurgical Engineering, Yonsei University, Seoul, KOREA
Thesis title: Characterization of Defects in Sputtered AlN Protective Thin Film for Magneto-Optical Disk Applications
1988 - B.S., Metallurgical Engineering (*Summa Cum Laude*), Yonsei University, Seoul, KOREA

Work Experience

1992 – 1997: Advanced Display & MEMS Research Center, Daewoo Electronics Co., LTD, KOREA
1988 – 1989: Materials Design Laboratory, Korea Institute Science and Technology (KIST), KOREA

Publications

1. Yongki Min, Harry L. Tuller, Stefan Palzer, Jürgen Wöllenstein, Harald Böttner, "Gas response of reactively sputtered ZnO films on Si-based micro array", Sensors and Actuators B **93** (2003) p.435-441
2. J. Wöllenstein, J. A. Plaza, C. Cané, Y. Min, H. Böttner, H.L. Tuller, "A novel single chip thin film metal oxide array", Sensors and Actuators B 93 (2003) p.350-355
3. S.G. Kim, K.H. Hwang, Y.J. Choi, Y.K. Min, J.M. Bae, "Micromachined Thin-Film Mirror Array for Reflective Light Modulation", Annals of the CIRP 46 (1997) p.455-458
4. Harry L. Tuller, Theodore Moustakas and Yongki Min, "Novel method for p-type doping of wide band gap oxide semiconductors", Applied for US Patent (2002)
5. Yong-Ki Min and Myung-Jin Kim, "Array of thin film actuated mirrors for use in an optical projection system and method for the manufacture thereof", US Patent No. 6, 030, 083 (2000)
6. Yong-Ki Min, "Method for manufacturing a thin film actuated mirror array", US Patent No. 5, 937, 271 (1999)
7. Yong-Ki Min, "Array of thin film actuated mirrors and method for the manufacture thereof", US Patent No. 5, 930, 025 (1999)
8. Yong-Ki Min, "Thin film actuated mirror array in an optical projection system and method for manufacturing the same", US Patent No. 5, 886, 811 (1999)
9. Yong-Ki Min and Myung-Jin Kim, "Array of thin film actuated mirrors for use in an optical projection system and method for the manufacture thereof", US Patent No. 5, 835, 293 (1998)
10. Yong-Ki Min and Min-Sik Um, "Method for forming an electrical connection in a thin film actuated mirror", US Patent No. 5, 834, 163 (1998)
11. Yong-Ki Min and Yoon-Joon Choi, "Thin film actuated mirror array in an optical projection system and method for manufacturing the same", US Patent No. 5, 815, 305 (1998)
12. Yong-Ki Min, "Thin film actuated mirror array having spacing member", US Patent No. 5, 808, 782 (1998)
13. Yong-Ki Min, "Thin film actuated mirror array for use in an optical projection system", US Patent No. 5, 757, 539 (1998)
14. Yong-Ki Min, "Thin-film actuated mirror array and method for the manufacture thereof", US Patent No. 5, 754, 331 (1998)
15. Yong-Ki Min, "Method for the manufacture of an electrodisplacive actuator array", US Patent No. 5, 735, 026 (1998)
16. Yong-Ki Min, "Array of electrically independent thin film actuated mirrors", US Patent No. 5, 708, 524 (1998)
17. Yong-Ki Min, "Low temperature formed thin film actuated mirror array", US Patent No. 5, 706, 121 (1998)
18. Yong-Ki Min, "Method for forming an array of thin film actuated mirrors", US Patent No. 5, 690, 839 (1997)
19. Yong-Ki Min, "Array of thin film actuated mirrors for use in an optical projection system", US Patent No. 5, 627, 673 (1997)

Table of Contents

TITLE ... 1
ABSTRACT ... 2
ACKNOWLEDGMENTS ... 3
BIOGRAPHICAL NOTE ... 4
TABLES OF CONTENTS ... 5
LIST OF FIGURES ... 7
LIST OF TABLES ... 14

1. INTRODUCTION ... 15

2. BACKGROUND ... 19
2.1 Operation principles of the semiconducting gas sensor ... 19
2.1.1 Bulk conductivity changes in semiconducting oxides ... 19
2.1.2 Surface conductivity changes in semiconducting oxides ... 21
2.2 Sensor requirements and characteristics ... 25
2.3 Thin film gas sensors ... 27
2.4 Zinc oxide ... 34
2.4.1 Properties of ZnO ... 34
2.4.2 Defect chemistry ... 38
2.4.3 Sputtered ZnO thin films ... 42
2.4.4 ZnO gas sensors ... 46

3. EXPERIMENTAL PROCEDURE ... 50
3.1 Processing ... 50
3.1.1 Semiconducting oxide film preparation ... 50
3.1.2 Micro array gas sensors ... 52
3.2 Physical and chemical analysis ... 58
3.3 Electrical measurements for gas sensor performance ... 59

4. RESULT 62
4.1 Physical and chemical analysis 62
4.2 Gas sensor performance 74
4.2.1 Sensor response 74
4.2.2 Current-voltage characteristics 81
4.2.3 AC impedance response 89
4.3 Time dependent sensor performance 96
4.3.1 Time dependent response 96
4.3.2 Time dependent DC bias effect 101

5. DISCUSSION 113
5.1 The influence of processing conditions on the property of ZnO films 113
5.2 The influence of processing conditions on sensor performance 116
5.3 The electrical characteristics of ZnO thin film micro array sensors 121
5.4 Time dependent sensor performance 130

6. CONCLUSION AND SUMMARY-KEY FINDING 140
7. FUTURE WORK 143
REFERENCE 144

List of Figures

Figure

1.1. Schematic of a feedback control system with sensors and actuators capable of translating other forms of energy (in this example, chemical) into and from electrical energy, the language of the microprocessor. 15

2.1 Grains of semiconductor, to show how the inter-grain contact resistance appears 22
2.2 Influence of particle size and contacts on resistances and capacitances in thin films are shown schematically for a current flow I from left to right. 23
2.3 Schematic models for grain-size effects 24
2.4 The intersection of the three rings creates a new field of sensor and actuator devices with exceptional functionality and versatility 27
2.5 Schematic view of gas sensing reaction in (a) Compact layer and (b) Porous layer 28
2.6 Schematic of a compact layer with geometry and energy band representation; Z_0 is the thickness of the depleted surface layer; Zg is the layer thickness and eV_S the band bending. (a) A partly depleted compact layer ("thicker") and (b) A completely depleted layer ("thinner") 29
2.7 Schematic of a porous layer with geometry and surface energy band with necks between grains; Z_n is the neck diameter; Z_0 is the thickness of the depletion layer and eV_S the band bending. (a) A partly depleted necks and (b) A completely necks 29
2.8 (a) 2 x 2 micro array on Si/SiO_2-bulk substrate (b) Sensor responses of the different sensors of the multi sensor-array during exposure to H_2 (100 ppm), CO (50 ppm), NO_2 (1 ppm) and NH_3 (50 ppm) in synthetic air with 50% relative humidity, respectively at the operating temperature of 420 °C 30
2.9 (a) Top view of a suspended microhotplate structure, (b) Schematic of the various layers comprising the structure and (c) Temperature programmed response of tin oxide microhotplate sensors to a series of organic vapors 31
2.10 Commercial semiconducting gas sensors based on micromachining techniques; (a) Multi-sensor mounted on a standard TO-5 package, (b) Schematic drawing, (c) and (d) Gas sensing microsystem module 32
2.11 3-D view and cross section of the proposed gas sensor array with CMOS-circuitry 33
2.12 T-X diagram for condensed Zn-O system at 0.1 MPa 35

Figure

2.13 Many properties of zinc oxide are dependent upon the wurtzite hexagonal, close-packed arrangement of the Zn and O atoms, their cohesiveness and void space 36

2.14 The Ellingham diagram for oxides 37

2.15 Various types of point defects in crystalline materials 38

2.16 Phase diagram of $ZnO-Al_2O_3$ system 44

3.1 Deposition rates of sputtered ZnO thin films 51

3.2 (a) Top view of zinc oxide thin film array with four sensing elements (765 x 685 μm). The chip size is 9 mm^2. The layout shows the interdigital electrodes, heater and temperature sensor which are composed of Pt/Ta films. (b) Pt/Ta interdigited bottom electrodes with 18 μm distance (c) Schematic of ZnO gas sensor structure 53

3.3 Process steps for Pt/Ta metallization (1) Si/SiO_2 wafer, (2) aluminium layer by e-beam evaporation, (3) spin coated photoresist, (4) photoresist patterned by photolithographic process, (5) wet etched aluminium layer, (6) deposition of Pt/Ta multi layers, (7) lift off process, and (8) removal of the sacrificial aluminium layer 54

3.4 A photo of mounted multi oxide micro array sensor with four gas sensing elements; SnO_2, WO_3, CTO and V_2O_5 55

3.5 (a) A schematic cross sectional view of the mounted sensor chip and (b) a photo of the mounted sensor chips 56

3.6 (a) Top view of micromachined micro array with four sensing elements and (b) Pt interdigited electrode with distance 20 μm 57

3.7 Micro array gas sensors with micromachined membrane platform and glass bridge (a) A schematic of micro hotplate gas sensor, (b) bottom view (c) top view 57

3.8 Schematic cross sectional view of test chamber (a) and cover (b), and photos of the mounted sensor chip and test chamber (c) and (d) 59

3.9 Gas sensor measurement setup 61

4.1 Optical microscopy images of micro array sensor with patterned ZnO films 62

4.2 SEM photographs of the ZnO film on Pt electrode (a) Before annealing and (b) After 700 °C annealing in synthetic air for 12 hours 62

4.3 X-ray diffraction patterns of pure ZnO films (a) $Ar:O_2$ = 7:3, (b) $Ar:O_2$ = 5:5, (c) $Ar:O_2$ = 3:7, and (d) reference from ZnO powder 64

Figure

4.4 Characteristic parameters given by XRD from ZnO (002) planes. (a) Spacing and (b) Full width at half maximum (FWHM) 65
4.5 X-ray diffraction patterns of (a) Al doped ZnO films and (b) reference from ZnO powder 67
4.6 Characteristic parameters given by XRD from Al doped ZnO films. (a) Spacing and (b) Full width at half maximum (FWHM) 68
4.7 AFM images of ZnO films on Si based micro array after annealing at 500 and 700 °C for 12 hours (a) 2 dimensional view (1 μm x 1 μm) and (b) 3 dimensional view (1 μm x 1 μm) 69
4.8 SEM images of Al doped ZnO films after annealed at 700 °C for 12 hours (a) Planar view (Tilt=0°) and (b) Tilted view (Tilt=52°) 71
4.9 SEM images of Al doped ZnO films on SiO_2 coated Si wafer after 700 °C annealed for 12 hrs. Each images shows the cross sectional view after etched continuously by Ga ion beam (t_1 and t_2) 71
4.10 O/Zn ratios of ZnO films onto micro arrays measured by WDS 72
4.11 Gas responses of sputtered ZnO micro array sensors to H_2 (100 ppm), CO (50 ppm), NO_2 (2 ppm) and NH_3 (50 ppm) in air (50% R.H., 25 °C) at 420 °C 75
4.12 Gas responses of sputtered ZnO micro array sensors to H_2 (10, 20, 50 and 100 ppm), NO_2 (1, 2 and 5 ppm) and CO (10, 20, 50 and 100 ppm) (a) Ar:O_2 = 7:3 and (b) Ar:O_2 = 3:7......... 76
4.13 Temperature dependent sensitivity of ZnO micro arrays to (a) 100 ppm H_2, (b) 5 ppm NO_2, and (c) 100ppm CO.......... 76
4.14 Resistance of undoped ZnO films during heating in air.......... 77
4.15 Gas responses of ZnO films with Ar:O_2 = 5:5 and 3:7 to CH_4 (130, 1000 ppm), NO_2 (2, 5ppm), CO (10, 50, 100 ppm) and NH_3 (20, 100, 200 ppm) in synthetic (50% R.H., 25 °C) at 460 °C. ZnO films were annealed at 700 °C for 12 hours 78
4.16 Gas response of undoped ZnO and Al doped ZnO micro array sensors to H_2 (100 ppm), CO (50 ppm), NO_2 (2 ppm) and NH_3 (50 ppm) in synthetic air at 420 °C.......... 79
4.17 Sensor responses of different gas sensitive films onto micro arrays during exposure to H_2 (100 ppm), CO (50 ppm), NO_2 (1 ppm) and NH_3 (50 ppm) in synthetic air with 50% relative humidity, respectively. The operating temperature was 420 °C 80
4.18 Current-voltage (I-V) curves of ZnO (Ar:O_2 = 7:3) micro array sensor measured at 300°C. I-V characteristics were observed from 0V to –2V, 0V, 2V to 0V with different sweep rates of 100 mV/sec and 10 mV/sec 81

Figure

4.19 Current-voltage (I-V) curves of ZnO ($Ar:O_2$ = 7:3) micro array sensors measured at 460°C. I-V characteristics were observed from 0V to –2V, 0V to 2V with different sweep rates of 100 mV/sec and 10 mV/sec 82

4.20 Current-voltage (I-V) curves of Al doped ZnO micro arrays measured at 420°C. I-V characteristics were observed from 0V to –2V, 0V to 2V with different sweep rates of 100 mV/sec and 10 mV/sec 83

4.21 Current-voltage (I-V) curves of multi oxide micro arrays. The voltage sweep rates were 100mV/sec and 10 mV/sec, and sweep direction was 0V to –2V, 2V, to 0V........ 84

4.22 Current-voltage (I-V) curves of ZnO ($Ar:O_2$ = 5:5) micro arrays measured at 460°C in several oxygen contents in argon. I-V characteristics were observed from 0V to –2V, 0V to 2V with different sweep rates of 100 mV/sec and 10 mV/sec........ 85

4.23 Gas responses and sensitivity of ZnO ($Ar:O_2$ = 7:3) micro arrays to 100 ppm CO and H_2 at 460°C using I-V measurements. I-V characteristics were observed from 0V to –2V, 0V to 2V with sweep rates of 100 mV/sec 86

4.24 Current-voltage (I-V) curves of the ZnO film ($Ar:O_2$ = 5:5) onto micro array chip measured at room temperature in open atmosphere. I-V characteristics were observed from 0V to –3V, 0V, 3V to 0V, or 0V to 3V, 0V, -3V to 0V with different sweep rates (100 mV/sec and 10 mV/sec)........ 87

4.25 Current-voltage (I-V) curves of ZnO film ($Ar:O_2$ = 5:5) onto micro array chip measured at room temperature in open atmosphere after ethyl alcohol treatment. I-V characteristics were observed from 0V to –3V, 0V, 3V to 0V, or 0V to 3V, 0V, -3V to 0V with different sweep rates (100 mV/sec and 10 mV/sec)........ 88

4.26 The AC impedance spectra of ZnO ($Ar:O_2$ =3:7) micro arrays in air at 460 °C with applied DC bias 0, 1 and 2V........ 89

4.27 The AC impedance spectra of ZnO ($Ar:O_2$ = 3:7) micro arrays in air at 460 °C measured at DC biases, following 40 min of DC biases pretreatment........ 90

4.28 AC impedance spectra of ZnO ($Ar:O_2$ =3:7) micro arrays in air at 460 °C without biases after DC bias pretreatments for 40 min........ 91

4.29 AC impedance spectra of SnO_2 and CTO micro arrays in air at 420 °C. The spectra were measured at DC 1V bias following the DC 1V pretreatment for 40 min........ 92

Figure

4.30 AC impedance spectra of ZnO ($Ar:O_2$ = 3:7) micro arrays exposed to the different oxygen contents in argon at 420 °C. The spectra were obtained without DC bias following repeated measurements every 5 min for 17 hours 93

4.31 AC impedance spectra of ZnO ($Ar:O_2$ = 7:3) micro arrays exposed in air to CO (100 ppm), NO_2 (10 ppm) and H_2 (100 ppm) at 420°C without applied DC biases during measurements . 94

4.32 Responses of ZnO ($Ar:O_2$ = 3:7) micro arrays exposed 100 ppm H_2 in air at 460°C with applied DC biases of 0, 1 and 2V 95

4.33 Resistance changes of ZnO micro arrays in oxygen/argon mixtures and dry air at the temperature of 420º C. The AC impedance spectra were utilized without biases. The ZnO was exposed to (a) 1% O_2 in Ar, (b) 0.1% O_2 in Ar, and (c) Ar following dry air or (d) dry air following Ar. The response is expressed as the ratio of resistance between oxygen/argon mixtures and dry air 97

4.34 Relation of resistance of ZnO ($Ar:O_2$ = 5:5) micro array and oxygen contents in argon. The resistance was measured by AC impedance spectra without biases at 420º C for 17 hours 98

4.35 Resistances of ZnO ($Ar:O_2$ = 3:7) measured in oxygen/argon mixtures at the temperatures of 380, 420 and 460º C. The ZnO was exposed from 10% oxygen to the oxygen/argon mixtures of 1, 0.1 and 0.01% for 5 hours 99

4.36 Resistance of ZnO ($Ar:O_2$ = 3:7) in oxygen/argon mixtures. The resistance was measured by AC impedance spectra without biases after the exposure of 5 hours........ 100

4.37 Resistance of ZnO ($Ar:O_2$ = 3:7) with operating temperatures. The resistance was measured from AC impedance spectra without biases after the 20 hours of the exposure to 10% and 0.01% oxygen in argon 100

4.38 Resistance drifts of ZnO ($Ar:O_2$ = 7:3) micro array in dry air at 460º C. AC impedance spectra was performed in every 5 min for 2 hours each set of measurements. DC 1V bias was applied during the measurements of 2 hours. Between first and second measurements, ZnO was left at 460 °C without applied biases for 24 hours........ 101

4.39 Resistance drift of ZnO ($Ar:O_2$ = 5:5) micro array in dry air at the temperature of 420º C. The AC impedance spectra were utilized with DC biases of 0, 1 or –1V during the pretreatment and measurement 103

4.40 Time dependent DC bias effects of ZnO ($Ar:O_2$ = 5:5) micro array in dry air at the temperature of 420º C. (a) AC spectra at each experiment regime and (b) Resistance drifts with DC 1V bias 104

Figure

4.41 Resistance drifts of ZnO ($Ar:O_2$ = 5:5) in dry air at 420º C. The AC impedance spectra were utilized with DC 0.2V bias during pretreatment and measurement 105
4.42 AC spectra of Al doped ZnO micro array at each experiment regime in dry air at the temperature of 420º C. The AC impedance spectra were utilized with DC 1V bias 106
4.43 Resistance drifts of SnO_2 micro array onto micromachined platform in dry air at 400º C. The AC impedance spectra were utilized with DC 1V bias 107
4.44 Resistance drifts of CTO micro array in dry air at 420º C. The AC impedance spectra were utilized with DC 1V bias 107
4.45 Resistance drift of ZnO ($Ar:O_2$ = 5:5) in 100 ppm H_2 of dry air at 420º C. The AC impedance spectra were utilized with DC 1V bias 108
4.46 The resistance drift of ZnO micro array in oxygen/argon mixtures at 420º C. The AC impedance spectra were utilized with DC biases of 0, 1 or –1V during pretreatment and measurement. (a) In 1% O_2 in Ar and (b) In 0.1% O_2 in Ar 109
4.47 Observed AFM images of ZnO micro array ($Ar:O_2$ = 3:7) during polarization DC 5V was applied to micro array in 2 hours at 500 °C for polarizing ZnO micro array 110
4.48 AFM images of ZnO micro array ($Ar:O_2$ = 3:7) during applying DC voltage to interdigited electrodes 111

5.1 Schematic representation of the structure of sputtered ZnO films.. 115
5.2 Schematic comparison of relative influence of adsorbed gases on the depletion layer width of ZnO prepared with different O_2/Ar ratios 116
5.3 Schematic dimensions of ZnO micro arrays including ZnO film, two Pt/Ta interdigited electrodes and SiO_2 layer 117
5.4 Schematic view of gas sensing reaction in (a) Undoped ZnO films (compact layer) and (b) Al doped ZnO films (porous layer) for ZnO micro array sensors 120
5.5 Schematic elementary contributions for current flow and equivalent circuits of ZnO thin films on micro array.. 122
5.6 Energy band diagrams for ideal MS contacts between a metal and n-type semiconductor: $\Phi_M > \Phi_S$ system (a) an instant after contact formation, (b) under equilibrium condition, formed Schottky diode (c) Carrier activity when $V_A > 0$, (d) Carrier activity when $V_A < 0$ and (e) Deduced general form of the I-V characteristics 123
5.7 Simplified equivalent circuit of ZnO micro array sensors with buried Pt electrodes 124

Figure

5.8 Equivalent circuits of ZnO micro array sensors with buried Pt electrodes during AC impedance spectra measurement 126
5.9 Model for DC bias effect on ZnO films: Depletion induced at reverse biased electrode on right combines with gas induced depletion layer from surface to form the constriction resistance R_2.. 127
5.10 Modulation of grain boundary barrier by DC bias (a) Without bias, (b) Applying a DC bias, and (c) After removal of DC bias 129
5.11 Typical sensor response of Figaro sensor 130
5.12 Response of ZnO with oxygen atmosphere with oxygen adsorption/desorption on surface (1), oxygen exchange on surface (2) and oxygen migration in ZnO (3).. 131
5.13 One dimensional diffusion model in reduction environment with the profile of oxygen concentrations.. 133
5.14 Model for time dependent DC bias effect on the resistance of ZnO micro arrays: The constriction resistance R_2 will be increased with time since the DC bias would initiate the ion migration inside ZnO and will modify the electronic status of each electrode region 137
5.15 Conductivity profile in a Fe doped $SrTiO_3$ single crystal obtained at 144 °C. Electric field (1 kV/cm) was applied via two electrodes for 90 min at 220 °C 139

List of Tables

Table

2.1 Zn-O crystal structure data 34

2.2 Properties of zinc oxide 36

2.3 Previous research on ZnO gas sensors 49

3.1 Deposition conditions for undoped ZnO thin films 50

3.2 Key components of the micro array ZnO gas sensor 55

3.3 Test gases for gas response and polarization effect measurements 60

4.1 XRD parameters of ZnO films deposited with various Ar/O_2 ratios 65

4.2 Calculated stresses in the plane and strains along the c-axis of ZnO films 66

4.3 XRD parameters and calculated strains of Al doped ZnO films 67

4.4 Average roughness (Ra, nm) of ZnO films on micro arrays by AFM 70

4.5 Atomic ratios of Zn, O and Al in ZnO films by WDS observation 72

4.6 Conditions of AC impedance spectra measurements 102

5.1 Gas responses of Al doped ZnO and ZnO with Ar:O_2 = 3:7 at 420 °C 120

1. Introduction

Many industrial and commercial activities involve the monitoring and control of the environment, with applications ranging from domestic gas alarms and medical diagnostic apparatus to safety, environmental, and chemical plant instrumentation. The largest barrier to achieve improved process or environmental control often lies at the interface between the system and the environment to be monitored, i.e. the sensor. Without sensors, significant advances in control and instrumentation will not be possible.

Figure 1.1 shows the standard operation of a feedback control system, in which the sensor and the actuator translate other forms of energy (in this example, chemical) into and from electrical energy, the language of the microprocessor. Unlike control electronics, sensors must interact with, and often are exposed directly to the environment. Even apparently benign atmospheres may contain corrosive or contaminating species, which can seriously interfere with sensor function and make sensor design and development a painstaking and expensive business. Thus, sensor technology has continued to lag, particularly with regard to achieving adequate sensitivity, selectivity, selectivity, reproducibility, and stability at reasonable cost [1, 2].

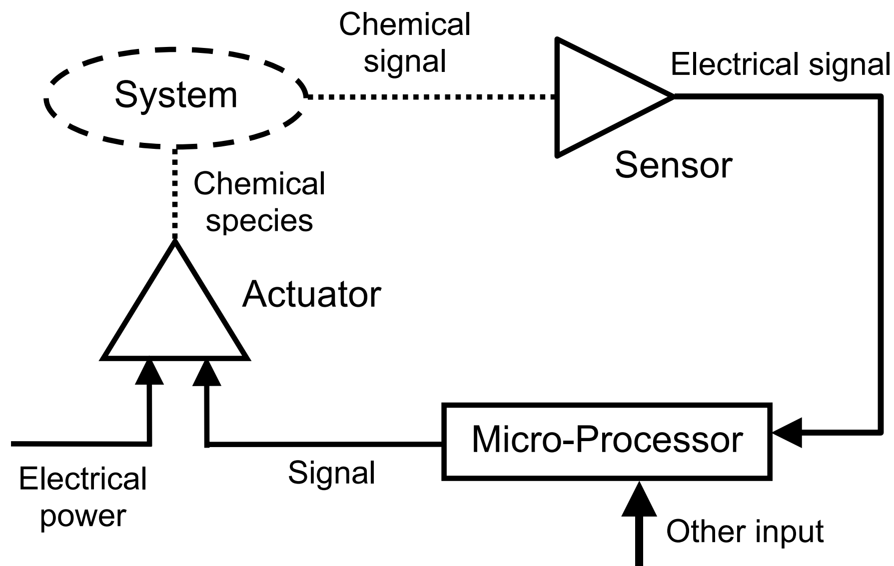

Figure 1.1 Schematic of a feedback control system with sensors and actuators capable of translating other forms of energy (in this example, chemical) into and from electrical energy, the language of the microprocessor [2].

Gases are key targets in many industrial and domestic activities requiring improved levels of measurement or control. This has been stimulated by a series of clean air laws, which have or are being legislated on the international, national, state and local levels. These often require in-situ continuous monitoring of air quality and the rates of emissions of specific chemical species. In particular, the efficiency of internal combustion engines in automobile and their level of emissions can now be optimized with in-situ exhaust gas sensors.

Three major types of gas sensors have been developed for commercial applications. The first is the ZrO_2-Y_2O_3 solid oxide electrolyte-based potentiometric sensor for automobile exhaust monitoring. The second, the current limiting sensor, also using the ZrO_2-Y_2O_3 solid electrolyte but in the ion pump mode, is designed to operate under lean burn conditions in automobiles. The final one is the semiconducting gas sensor, which uses conductance variations for detecting low concentration of gases.

Among the various types of gas sensors, semiconducting gas sensors are promising candidates for sensor development given their sensitivity to many gases of interest and the ability to fabricate them readily in many configurations, e.g. as single crystals, thick and thin films. Thin film technology, in particular, is being actively applied in the development of semiconducting gas sensor devices given that such sensors depend largely on gas-surface interactions. Thin film gas sensors have potential advantages of fast response times, and importantly, the potential for miniaturization via integration with IC-based technology leading to low power consumption, higher reliability via batch fabrication, and improved selectivity through use of arrays and reduced cost. The small size of semiconductor sensors fabricated on Si substrate allows for integration with Si-based microelectronic circuits and micro-electro-mechanical systems (MEMS), thus further enhancing their performance by the development of "smart sensors" that incorporate on-chip electronics for data acquisition and signal processing [3, 4]. In particular, the development of gas sensors based on micromachined structures is a rapidly growing area, enabling fabrication of arrays of sensor elements coupled with reduced power consumption and improved selectivity via low thermal mass membranes [2, 5-8].

In 1962, porous semiconducting ceramics, ZnO and SnO_2, were first demonstrated as gas sensing devices. Although conductometric gas response measurements were

originally made on ZnO, SnO_2 has received the majority of attention in recent decades for commercial gas detectors given that it offers high sensitivity at lower operating temperature [1]. However, in spite of extensive activity for commercial gas sensors, the fundamental understanding of these sensing properties remains poor since an empirical optimization of sensor performance has been the focus of most investigators. To meet recent demands for gas sensors capable of detecting environmentally important gases and odors with sub-ppm levels, the establishment of new design concepts based on a more fundamental basis is necessary. In this work, a more fundamental understanding of gas sensing mechanisms of semiconducting oxide thin films has been pursued since the advent of micro array gas sensors using thin films and micromachining technology has stimulated an interest in mechanisms operative in thin film sensors. Specifically, the influence of thin film processing conditions and DC applied bias on the properties and gas sensing performance of semiconducting thin films on micro array platforms was investigated. This enabled a more detailed understanding of the role of stoichiometry and electromigration of ions on the performance and stability of thin film semiconducting sensors.

In this study, among the various semiconducting oxide materials, ZnO has been chosen as the key gas sensing material since it has been widely studied and is easily fabricated as high quality films by sputtering, compatible with Si-based IC processes. In 1959, Heiland reported on the gas sensitive behavior of ZnO's electrical conductivity [1]. Since then, many fundamental investigations concerning the gas sensitive nature of ZnO single crystals [9, 10], polycrystalline ceramics [11], thick films [12, 13] and thin films [14, 15, 16] have been performed. Zinc oxide is a II-VI compound semiconductor with a wide direct bandgap of 3.4 eV at room temperature [17]. It is a widely used material in various applications such as piezoelectric devices, varistors, surface acoustic wave (SAW) devices and transparent conductive oxide electrodes [18, 19].

For the investigation of gas sensor performance of sputtered ZnO films, micro arrays were fabricated onto bulk silicon wafers with interdigited Pt electrodes and integrated Pt heater and temperature sensor. Reactive magnetron sputtering was used to deposit ZnO films by use of a Zn metal target, under varied oxygen partial pressure to obtain films with controlled composition and microstructure. The effects of the sputter processing

condition, Al dopant and post deposition annealing on the physical and chemical properties of the ZnO films were investigated using AFM, FIB-SEM, XRD and WDS.

The atmosphere dependent electrical response of ZnO films sputtered onto micro-arrays in response to changes in the concentrations of reducing and oxidizing gases was examined and compared to other gas sensor materials (with focus on SnO_2) on micro arrays. DC resistance, I-V curves and AC impedance spectra were observed to investigate the gas response of ZnO films on micro arrays. AC impedance measurements were used to assist in identifying the individual contributions to the sensor response from the grains, grain boundaries and oxide/electrode interfaces. In this study, particular emphasis was placed on examining the time dependent and field induced drift/degradation effects of gas sensor performance of micro array sensors, which would impact the stability of thin film sensors for practical application. These drift/degradation phenomena are suspected to be related to surface gas adsorption/desorption and ion migration, or the modulation of grain boundary barrier height in the ZnO film due to high electric field between electrodes.

2. Background

2.1 Operation principles of the semiconducting gas sensor

Semiconducting oxides are known to exhibit sensitivity to various gases [1, 20, 21]. At elevated temperatures, typically above 900 ºC, this results from atmosphere induced changes in stoichiometry. This type of oxygen sensor involves the high temperature bulk reactions between point defects in the oxides and oxygen (O_2) in the gas phase. At considerably lower temperatures, typically below 400 ºC, conductivity changes in semiconducting oxides such as SnO_2 and ZnO, are tied to adsorption/desorption phenomena which impact primarily surface or grain boundary conductivity, the latter only for porous polycrystalline materials [1, 21]. The surface reactions, in n-type semiconductors, involve adsorbed negatively charged molecular (O_2^-) or atomic (O^-) oxygen species. The majority of semiconducting oxide sensors are primarily of the latter type, given the ability to adapt them to sense a broad variety of gases as well as the reduced demands on lower temperature packaging. In recent years, there has been a trend away from bulk porous ceramics to thin films given the ability to miniaturize devices and integrate them with silicon technology.

2.1.1 Bulk conductivity changes in semiconducting oxides

The change in stoichiometry of semiconducting oxides as a function of the oxygen activity of their environment, particularly at elevated temperatures, is well known. This change in stoichiometry affects the electrical conductivity, σ, of the materials. The change in conductivity can be represented by the relation [1],

$$\sigma = \sigma_o \exp(-E_A/kT)\, p(O_2)^{1/n} \qquad (2.1)$$

where k denotes Boltzmann's constant, T is the temperature in degrees Kelvin, E_A is an activation energy of bulk conduction and the term $p(O_2)$ is the partial pressure of the oxygen gas. The activation energy can be broken down into contributions arising from the energy required to form the ionic defects and their subsequent ionization thereby forming charge carriers in the conduction or valence band. The sign and value of n (see Eq. 2.1) depend on the nature of the point defects arising when oxygen is removed from the lattice. Some semiconducting oxides such as TiO_2 [22, 23], Ga_2O_3 [24, 25], $BaTiO_3$

[26], and $SrTiO_3$ [20, 27] have been actively investigated as high temperature oxygen sensors.

When a TiO_2 oxygen sensor, for example, is exposed to the low oxygen pressure environment at temperatures high enough to create defects, the reduction of TiO_2 is believed to occur resulting in the formation of Ti interstitials, $Ti_i^{\bullet\bullet\bullet\bullet}$. The reaction is given by

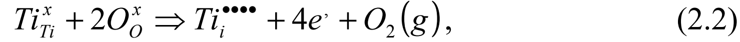

$$Ti_{Ti}^{x} + 2O_O^{x} \Rightarrow Ti_i^{\bullet\bullet\bullet\bullet} + 4e' + O_2(g), \tag{2.2}$$

with the charge neutrality being,

$$4 \cdot [Ti_i^{\bullet\bullet\bullet\bullet}] = n. \tag{2.3}$$

The equilibrium constant of the reduction reaction (2.2) is

$$K_R = [Ti_i^{\bullet\bullet\bullet\bullet}] \cdot n^4 \cdot p(O_2). \tag{2.4}$$

When equation (2.3) and (2.4) are combined,

$$n = 4 \cdot [Ti_i^{\bullet\bullet\bullet\bullet}] = (4K_R)^{1/5} \cdot p(O_2)^{-1/5} \tag{2.5}$$

Therefore, the reduction of TiO_2 by formation of Ti interstitial defects has a dependence on oxygen pressure of n = -5.

Regardless of the actual compensation mechanism, the important point for practical applications is that the conductivity of semiconducting oxides exhibits a useful $p(O_2)$ dependence. Virtually all modern automobiles have a feedback system in which an oxygen gas sensor is used to measure the $p(O_2)$ of the exhaust stream, and provides an electrical input via the microprocessor to the fuel injection system to optimize the air/fuel ratios to maintain minimal emissions as driving conditions change.

In an actual oxygen sensor, the conductivity of polycrystalline TiO_2 exposed to the exhaust gas is continuously monitored. In order to shorten the response time, a porous TiO_2 element is desirable. This increases the surface area for gas exchange, and decreases the effective cross section across which the nonstoichiometry must change [22].

One potential difficulty presented by this resistive oxygen sensor is that the conductivity is temperature as well as $p(O_2)$ dependent, due to the fact that defect chemical equilibrium constants are exponentially dependent on temperature. Since a range of operating temperatures is encountered in use, some form of temperature compensation is necessary for the sensor output to be accurate. One engineering solution

is to incorporate a heater to keep the sensor at a constant temperature above that of the exhaust temperature. Another is to utilize a dense TiO_2 specimen as a reference, which operates at the same temperature as the porous sensor, but does not equilibrate quickly with the gas stream. A comparison of the resistivities of the two polycrystalline elements then allows the oxygen pressure dependence of conductivity in the porous TiO_2 to be isolated [22].

2.1.2 Surface conductivity changes in semiconducting oxides

Sintered, porous pellets of SnO_2 show a substantial conductivity change when small concentrations of a combustible gas are present in a large excess of oxygen. The mechanism of bulk conductivity change cannot explain this observation, since the oxygen partial pressure would not sensibly be changed in this circumstance. The assumption, therefore, is that surface processes, which are not at equilibrium with the bulk, control the conductance [1]. The most widely accepted explanation for this is that negatively charged oxygen adsorbates play an important role in detecting gases such as H_2 and CO. Actually, several kinds of oxygen adsorbates, such as O_2^-, O^- and O^{2-}, are known to cover the surface of semiconducting oxides in air. Yamazoe et al [28] reported that oxygen showed the formation of four kinds of oxygen species on SnO_2 surfaces which desorb around 80 °C (O_2), 150 °C (O_2^-), 560 °C (O^- or O^{2-}) and above 600 °C (a part of lattice oxygen) respectively. Of these, O^- is the most reactive with reducing gases in the temperature range of 300-500 °C, in which most semiconductor gas sensors are operated. The variation in surface coverage of O^- therefore is believed to dominate the sensor response. In the case of n-type semiconducting oxides, the formation of this oxygen adsorbate builds space charge regions on the surfaces of the oxide grains, resulting in an electron-depleted surface layer due to the oxygen adsorbates as follows:

$$O_2\,(g) + 2e' = 2O^-\,(s) \qquad (2.6)$$

The resistance of an n-type semiconducting oxide gas sensor in air is therefore high, due to the development of a potential barrier. The space charge layer (W) can be defined using Poisson's equation as follows [1]:

$$W = \frac{Q_S}{e \cdot N_D} = [\frac{2 \cdot K \cdot \varepsilon_O \cdot \Delta\phi_S}{e \cdot N_D}]^{1/2} \qquad (2.7)$$

Here, Q_S and N_D are surface charge and the number of ionized donor states per unit volume, and K, ε_O, and $\Delta\phi_S$ denote the static dielectric constant of the oxide, the permittivity of the vacuum, and the surface potential barrier height. With typical values ($K\varepsilon_O \sim 10^{-12}$ F/cm, $N_D \sim 10^{18} - 10^{20}$ cm^{-3} and $\Delta\phi_S \sim 1V$), the space charge layer thickness is generally around 1 – 100 nm [1].

Figure 2.1(a), for example, shows a schematic of a few grains of porous semiconducting oxide and the space charge region around the surface of each grain and at inter-grain contacts. The space charge region, being depleted of electrons, is more resistive than the bulk. The band model of Figure 2.1(b) shows potential barriers formed at inter-grain contacts [29].

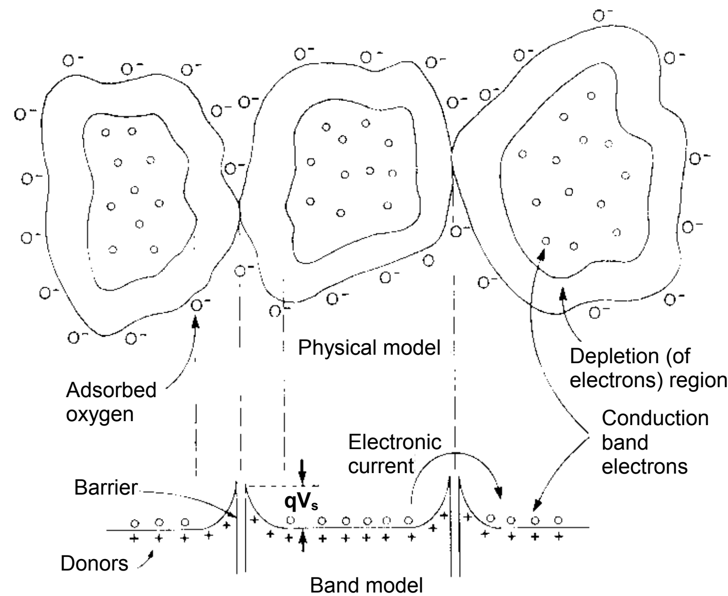

Figure 2.1 Grains of semiconductor, to show how the inter-grain contact resistance appears [29].

When the sensor is exposed to an atmosphere containing reducing gases at elevated temperatures, the oxygen adsorbates are removed by the reduction reaction, so that the steady-state surface coverage of the adsorbates is lowered. For example, if the sensor is exposed to H_2 atmosphere, the reaction will be as follows:

$$O^-(s) + H_2 \rightarrow H_2O + e' \quad (2.8)$$

During this process, the electrons trapped by the oxygen adsorbates return to the oxide grains, leading to a decrease in the potential barrier height and drop in resistance. Figure

2.2 shows the change of the potential barrier in air and reducing gas environments due to the variation of the space charge region at each grain boundary, contact and surface of semiconducting oxide [30]. These resistance changes exposed to reducing gases are used as the measurement parameter of the semiconductor gas sensor.

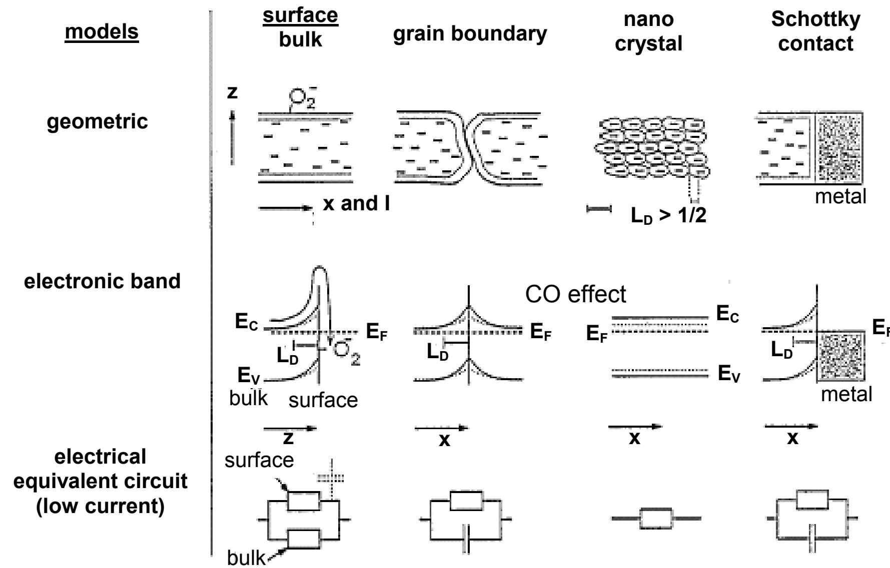

Figure 2.2 Influence of particle size and contacts on resistances and capacitances in thin films are shown schematically for a current flow I from left to right [30].

One of the most important factors affecting sensing properties is the actual grain or crystallite size D of the sensor materials in conjunction with the space charge depth L. Three kinds of resistance-control models have been proposed, which assume that a sensor consists of a chain of uniform crystallites of size D connected mostly with each other through necks and sometimes by grain boundaries, as shown in Figure 2.3. When D is less than 2L, the grain resistance dominates the resistance of the whole chain and in turn, the sensor resistance, so that grains themselves (grain control) control the sensitivity. Among the three models, grain control is the most sensitive condition. Thus, smaller grain sizes would be more sensitive than larger ones [31].

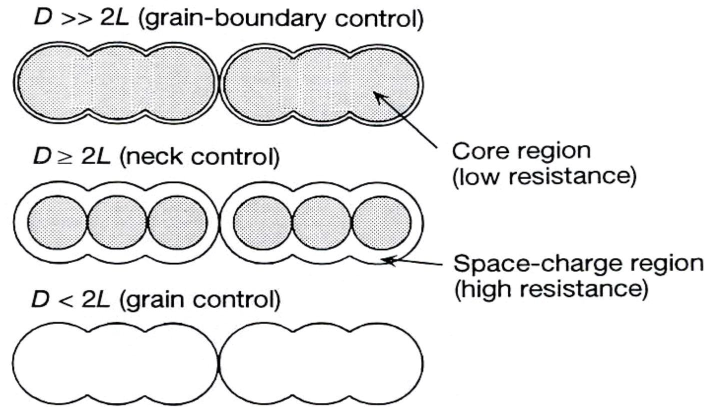

Figure 2.3 Schematic models for grain-size effects [31]

For most conventional semiconducting oxide materials, the particle size is considerably greater than the depth of the space charge, and electrical conduction is controlled by the grain boundaries. However, nanocrystalline materials can be produced which offer greatly reduced grain size, so that the depletion layer has similar dimensions to the particle radius. Under these conditions, oxygen adsorption will result in grains fully depleted of conduction-band electrons. Therefore, these materials can be potentially used to produce highly sensitive gas sensors [20, 23, 31].

Since the charge carriers in p-type semiconducting oxides are positive holes, the resistance in air is low because of the formation of negatively charged oxygen adsorbates, and the extraction of electrons from the bulk eventually enhances the concentration of holes in the grain surface. Then, the consumption of oxygen adsorbates by reaction with reducing gases leads to an increase in resistance, which is the reverse of the case for n-type semiconducting oxides. Conversely, the adsorption of oxidizing gases on p-type semiconducting oxides results in a decrease in resistance. Recently, as a p-type semiconducting oxide gas sensor, the titanium substituted chromium oxide (CTO ($Cr_{2-x}Ti_xO_{3+z}$) has been actively investigated due to its stability of performance over the short and long term, and weak sensitivity to humidity [32, 33, 34]. In this study, CTO was also examined as an element of a thin film micro array.

2.2 Sensor requirements and characteristics

Ever increasing industrialization makes it necessary to constantly monitor and control air pollution in the environment, in factories, laboratories, hospitals and general technical installations. The following list gives both constraints and requirements for an ideal chemical sensor [35]: chemically selective, reversible, fast, highly sensitive, durable, non-contaminating, non-poisoning, simple operation, small size (portable), simple fabrication, relative temperature insensitivity, low noise and low manufacturing costs.

When considering the semiconducting oxide sensor, the measured principal parameter is resistance (conductance, simply the reciprocal of resistance). All the operating characteristics of the sensor are derived from this simple measurement. This is both the strength and the weakness of semiconducting sensors. The strength is related to the fact that the resistance is a simple and easily measured parameter, but the weakness is that resistance is a second-order parameter, which is not a good indicator of the exact processes taking place. This is why the basic understanding of elementary steps of chemical sensing is still immature in contrast to the success in empirical research, development work and widespread practical applications [1, 30].

The key characteristics of gas sensor performance are sensitivity, selectivity, response time and stability. First, the sensitivity is defined as

$$\text{(Conductance in gas – Conductance in air)/Conductance in air} \qquad (2.9)$$

expressed as a percentage for a given concentration of a gas. This is the easiest parameter to handle when considering adsorption of donor gases on n-type semiconducting oxides [1]. Sensitivity is sometimes simply defined as (resistance in reducing gas)/(resistance in air) and (resistance in air)/(resistance in oxidizing gas) for n-type semiconductors for convenience. Using this definition of sensitivity, the sensitivity is easily calculated from the measured resistance values. Thus, it is very convenient to compare the sensitivities in each reducing and oxidizing gas environment. The gas sensitivity of semiconducting oxides has been intensively investigated because of recent demands for detection of environmentally important gases and odors with sub-ppm levels. Recently, nanocrystalline materials have been fabricated to improve sensitivity [31]. In this study,

the influence of thin film processing conditions on the sensitivity of ZnO micro arrays was investigated.

The selectivity is usually defined as the (sensitivity to gas 1)/(sensitivity to gas 2) for equivalent concentrations of both gases, or, sometimes, for the concentration of the gases known to be involved in the application of interest [1]. Semiconducting sensors often exhibit poor selectivity since their operation depends, in most cases, on the reaction of reducing gases with adsorbed oxygen. Recently, sensors with arrays and MEMS structures have been developed which exhibit improved selectivity using pattern recognition techniques [2].

The response time is usually defined as the time taken to achieve 90% of the final change in resistance following the change of gas concentration. However, response times are often expressed as 50% or 70% of the final time, since the response is often very fast initially, followed by a long drawn out tail before reaching steady value. The response time is an important parameter since it can determine the applicability of the sensor; unfortunately, it is probably the most difficult parameter to measure. It requires special gas flow systems which are designed to ensure that step changes in gas concentration are faster than the response time of the sensor, especially when dealing with highly adsorptive and reactive gases [1]. In this work, the slow response, on the scale of hours, following an initial fast response was observed in ZnO micro array sensors. This slow response was characterized by monitoring changes in the electrical conductivity.

Change over long operation times of both base line and sensitivity are important for the utilization of sensors. These determine the frequency at which calibration checks should be carried out and the frequency at which sensors may have to be replaced. They can only be determined over long periods of time since harsh conditions used to accelerate aging could result in changes of stoichiometry of the sensor materials. Several long period tests showed that degradation in microstructure was related to the stability of sensor performance [36, 37]. In this study, ZnO micro arrays showed time dependent resistance drifts induced by DC bias. This resistance drift, first reported in this study, was systematically investigated in an attempt to identify its source.

2.3 Thin film gas sensors

Thin film semiconducting oxide gas sensors offer various potential advantages via integration with IC-based technology and micromachined structures. Figure 2.4 illustrates that the intersection of microelectronics, micromechanics and electroceramics may lead to unique new microsystems, which include sensing, actuating, and signal processing functions [2]. Thus, the integration of semiconducting oxide thin films with microelectronics and MEMS would provide opportunities for developing unique sensor systems.

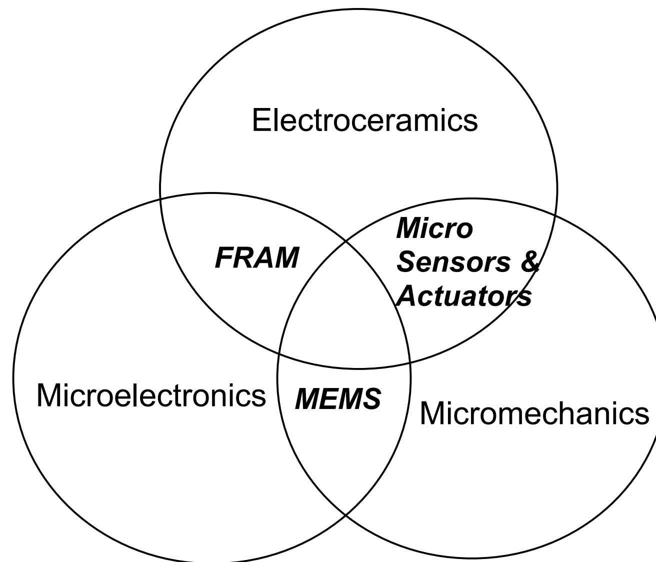

Figure 2.4 The intersection of the three rings creates a new field of sensor and actuator devices with exceptional functionality and versatility [2]

The thin film sensor mainly consists of sensor layer, electrodes, heater and substrate. Usually, the heater is separated from the sensing layer and electrodes by an electrical insulating layer. The gas sensing performance can take place at different sites of the sensing layer depending on its morphology. The morphology of the sensing layer can be simply divided into compact and porous ones. First, in compact sensing layers, gases cannot penetrate into the layer and the gas sensing reaction is confined to the surface of the sensing layer. This compact layer is usually obtained with one of a number of thin film deposition techniques. Second, in the porous layer, gases can access all of the volume of the sensing layer, and the gas sensing reaction can therefore take place at the

surface of individual grains, at grain-grain boundaries and interface between grains and electrodes. Figure 2.4 shows the gas interaction in the compact and porous layers [21].

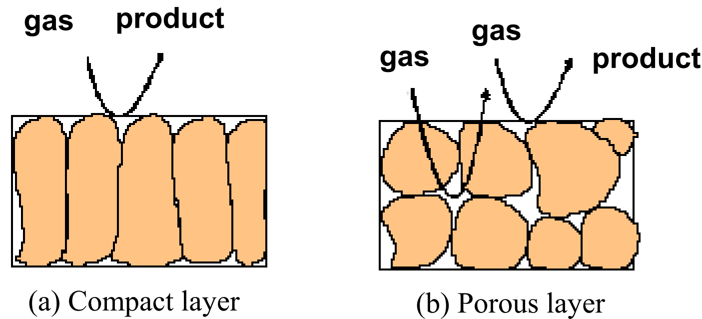

Figure 2.5 Schematic view of gas sensing reaction in (a) Compact layer and (b) Porous layer [21]

For compact layers, the sensing layer can be completely or partly depleted depending on the relation between film thickness and depletion layer as shown in Figure 2.6 [21]. When the film thickness (Zg) is smaller than the depletion layer thickness (Z_0), the compact sensing layer will be completely depleted. When the film thickness is larger than the depleted layer ($Zg > Z_0$), the sensing layer will be partly depleted and two resistances occur in parallel. One is influenced by surface reaction with the higher resistance value (layer Z_0) and the other one has the bulk resistance value (layer $Zg – Z_0$). Thus, the partly depleted layer can be treated as a conductive layer with a gas reaction dependent thickness. For the completed depleted layer, the exposure to reducing gases can act as a switch to the partly depleted layer. It is also possible that exposure to oxidizing gases acts a switch from partly to completely depleted layer.

For porous layers, the situation is more complicated because of the presence of necks between grains. Figure 2.7 shows the porous sensing layer with partly and completely depleted neck areas [21]. The possible switching role of reducing and oxidizing gases in compact layers is valid for porous layers since the depletion layer of the neck contact is also influenced by the atmosphere.

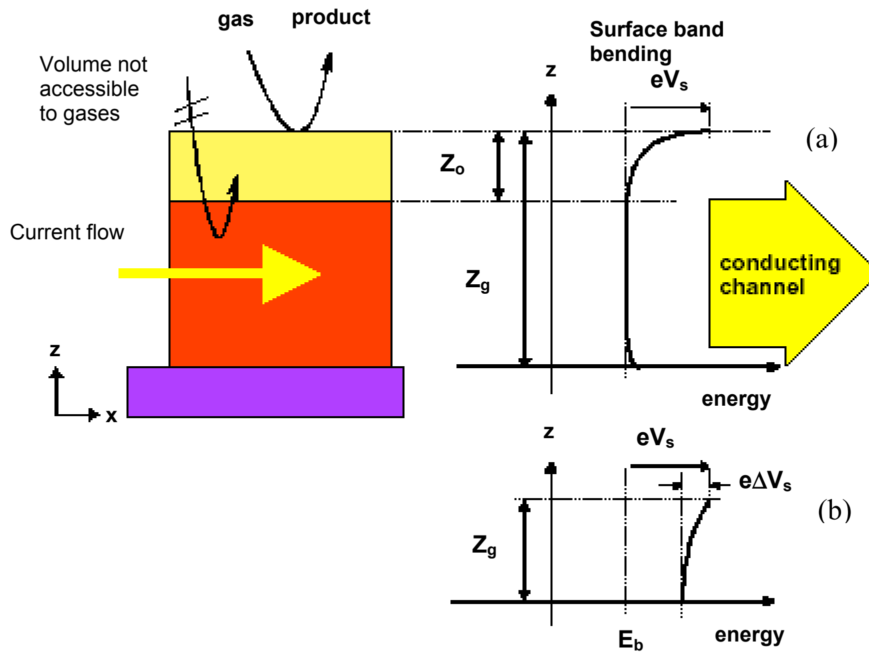

Figure 2.6 Schematic of a compact layer with geometry and energy band representation; Z_0 is the thickness of the depleted surface layer; Zg is the layer thickness and eV_S the band bending. (a) A partly depleted compact layer ("thicker") and (b) A completely depleted layer ("thinner") [21]

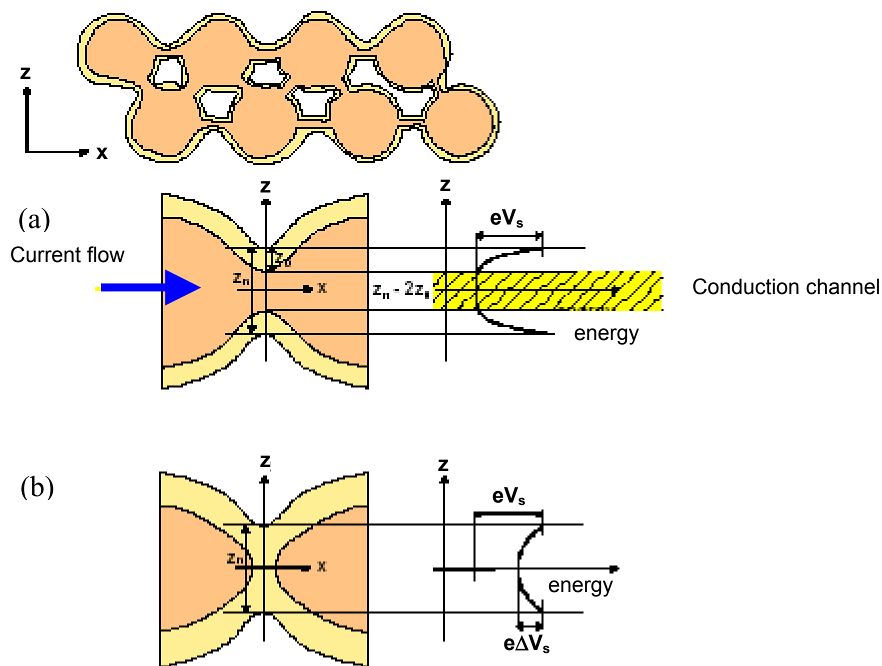

Figure 2.7 Schematic of a porous layer with geometry and surface energy band with necks between grains; Z_n is the neck diameter; Z_0 is the thickness of the depletion layer and eV_S the band bending. (a) A partly depleted necks and (b) A completely necks [21]

Thin film technology offers the opportunity to integrate a number of sensor elements in a micro array. Figure 2.8 (a) shows, as example, a schematic of a four-sensor thin film array fabricated on a thin silicon wafer of area 3 mm^2. Each gas sensing layer is deposited onto interdigited electrodes which allows for ready measurement. This array includes an integrated resistive heater and temperature sensor in addition to the four gas sensitive films. Given the high thermal conductivity of silicon and the small area, the temperature of the four sensors is maintained at virtually the same temperature with a reduced expenditure of power (about 2W). The resistance changes induced in five semiconducting oxide sensors during exposure to H_2, CO, NO_2 and NH_3, respectively at 420 °C are illustrated in Figure 2.8 (b). Four of the films (CTO ($Cr_{2-x}Ti_xO_{3+z}$), catalyst modified SnO_2, WO_3, and V_2O_5) were examined together on an array of the type illustrated in Figure 2.8 (a). The fifth film, ZnO, was located in another array but measured in parallel with the other four. Each oxide film exhibits a different response to the gases. For example, p-type CTO shows an opposite gas response compared to the other n-type oxides. Only ZnO exhibits a measurable response to NO_2 while V_2O_5 exhibits sensitivity to NH_3 alone. The distinctive response of the various films, taken together, provides means for analyzing the composition of gas mixtures via pattern recognition analysis techniques provided improved selectivity [38].

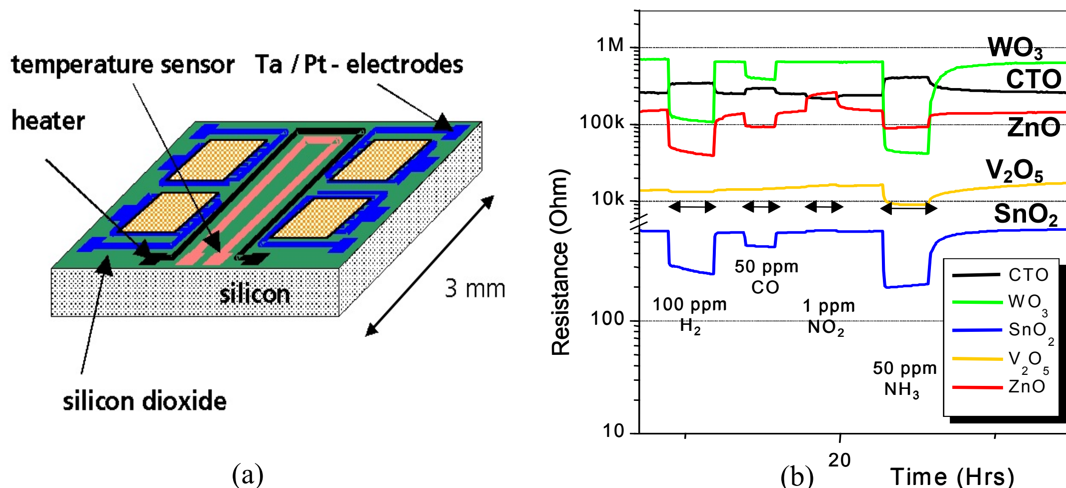

(a) (b)

Figure 2.8 (a) 2 x 2 micro array on Si/SiO_2-bulk substrate (b) Sensor responses of the different sensors of the multi sensor-array during exposure to H_2 (100 ppm), CO (50 ppm), NO_2 (1 ppm) and NH_3 (50 ppm) in synthetic air with 50% relative humidity, respectively at the operating temperature of 420 °C [38].

In combination with MEMS technology, micro array gas sensors could have very low power consumption and highly improved selectivity using microhotplates based on thin membranes (3-10 μm) with low thermal mass. Semancik et al [8] reported the use of micromachined, low mass (~0.2 μg) suspended microhotplates to rapidly cycle the temperature of sensor films on these structures at millisecond thermal rise and fall times as shown in Figure 2.9. Such cycling enables kinetic differentiation of chemical species by their unique temperature-response signature. Figure 2.9(c) shows the temperature-programmed response of tin oxide microsensors to a number of different solvents, demonstrating that distinct thermal signatures are achieved for each solvent. The use of microhotplate arrays having a various different sensing films provides further capability for identifying and distinguishing each gas element, since no two films compositions respond identically to the same gases.

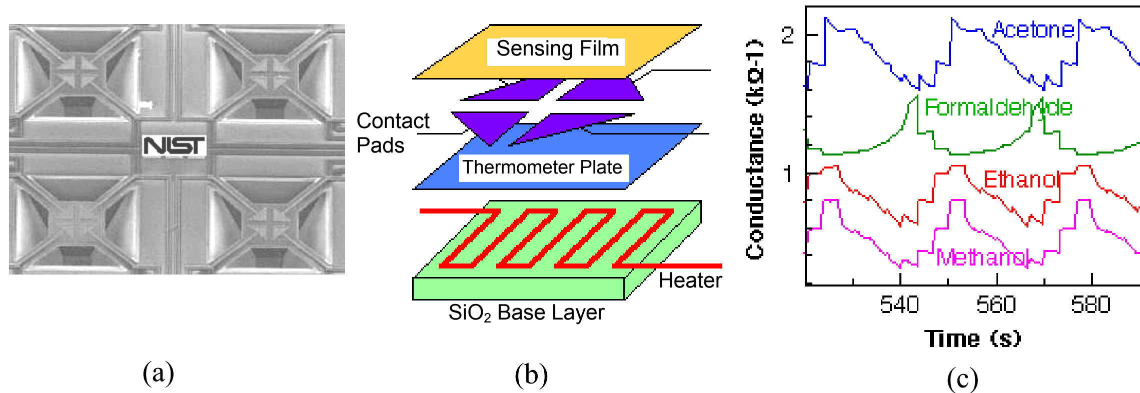

Figure 2.9 (a) Top view of a suspended microhotplate structure, (b) Schematic of the various layers comprising the structure and (c) Temperature programmed response of tin oxide microhotplate sensors to a series of organic vapors [8]

Figure 2.10 shows a commercially available semiconductor gas sensor manufactured using standard microelectronic and silicon micromachining techniques (Microsens SA, Switzerland). The sensitive layer consists of SnO_2-Nb_2O_5 deposited by magnetron sputtering (thickness 100 – 400 nm) with low stress silicon nitride used as the insulating membrane (0.8 μm). Power consumption for maintaining the sensor at 400 °C is around 40 mW using a Pt heater. Figure 2.10 (c) and (d) show the gas sensing module for portable systems. The module consists of two semiconductor gas sensors, a temperature

sensor and an 8-bit micro-controller, which performs data acquisition, processing and communication functions.

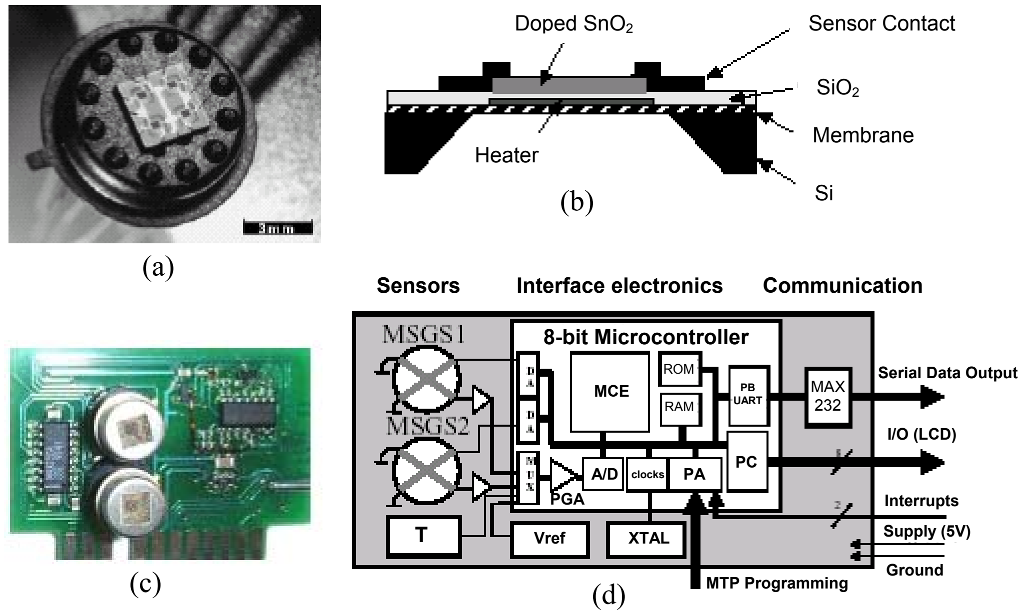

Figure 2.10 Commercial semiconducting gas sensors based on micromachining techniques; (a) Multi-sensor mounted on a standard TO-5 package, (b) Schematic drawing, (c) and (d) Gas sensing microsystem module (Microsens SA, Switzerland, www.microsens.ch)

Micromachined platforms with dielectric membranes are promising structures for next generation gas sensors due to low power consumption and high selectivity. However, such micromachined thin membrane platforms are fragile and perhaps difficult to integrate into commercial devices. Figure 2.11 shows an example of smart sensor arrays that incorporate on-chip electronics and micromachined gas sensor arrays, with robust design and excellent thermal isolation of the membrane from the surrounding wafer using glass [38]. This proposed smart sensor relies on the integration of micromachined gas sensors and CMOS driving and analysis circuits on a single chip. This will be possible due to the thermal decoupling of the sensing layers and the CMOS device, which guarantees a temperature under the critical 160 °C limit. The CMOS device is not covered by glass to prevent overheating and electrical failure during the glass to silicon anodic bonding step, but its structure is strengthened by glass walls [38].

.

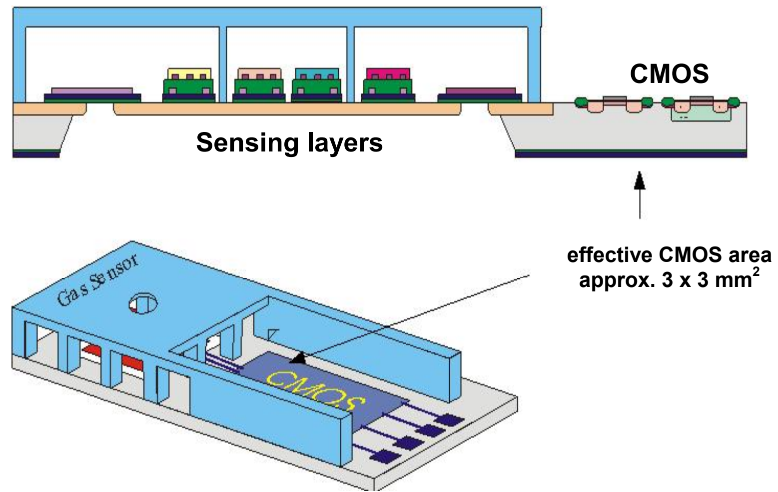

Figure 2.11 3-D view and cross section of the proposed gas sensor array with CMOS-circuitry [38]

2.4 Zinc oxide

2.4.1 Properties of ZnO

Zinc oxide is an interesting II-VI compound semiconductor with a wide direct bandgap of 3.4 eV at room temperature [17]. It is a widely used material in various applications such as gas sensors, UV resistive coatings, piezoelectric devices, varistors, surface acoustic wave (SAW) devices and transparent conductive oxide electrodes [18, 19]. Recently, ZnO has also attracted attention for its possible application in short-wavelength light emitting diodes (LEDs) and laser diodes (LDs) because the optical properties of ZnO are similar to those of GaN [39, 40, 41].

Figure 2.12 shows the phase diagram of the Zn-O binary system [42]. The equilibrium solid phase of the condensed Zn-O system at 0.1 MPa hydrostatic pressure are the hexagonal closed packed (hcp) Zn with a very narrow composition range, the hexagonal compound, ZnO (49.9 to 50.0 at. % O), with a narrow but significant composition range, and the cubic peroxide, ZnO_2 (~66.7 at. % O), with unknown composition range. Even though the existence of ZnO_2 has been reported, the nature and temperatures of the transformation are unknown. At elevated hydrostatic pressures, a face centered cubic (fcc) modification of ZnO is stable. Also, it has been reported that ZnO can exist metastably at room temperature in either of two cubic modifications with structures of ZnS (sphalerite) and NaCl (rock salt) types [43]. Table 2.1 summarizes data related to Zn-O crystal structures.

Table 2.1 Zn-O crystal structure data [43]

	Stable phases at 0.1 MPa			Other phases	
	Zn	ZnO (I)	ZnO_2	ZnO (II)(a)	ZnO (III)
Composition, at.% O	~0	49.9 to 50.0	~66.7	~50	~50
Pearson symbol	*hP*2	*hP*4	*cP*12	*cF*8	*cF*8
Space group	$P6_3/mmc$	$P6_3mc$	*Pa*3	*Fm*3(-)*m*	*F*4(-)3*m*
Prototype	Mg	ZnO (wurtzite)	FeS_2 (pyrite)	NaCl	ZnS (sphalerite)

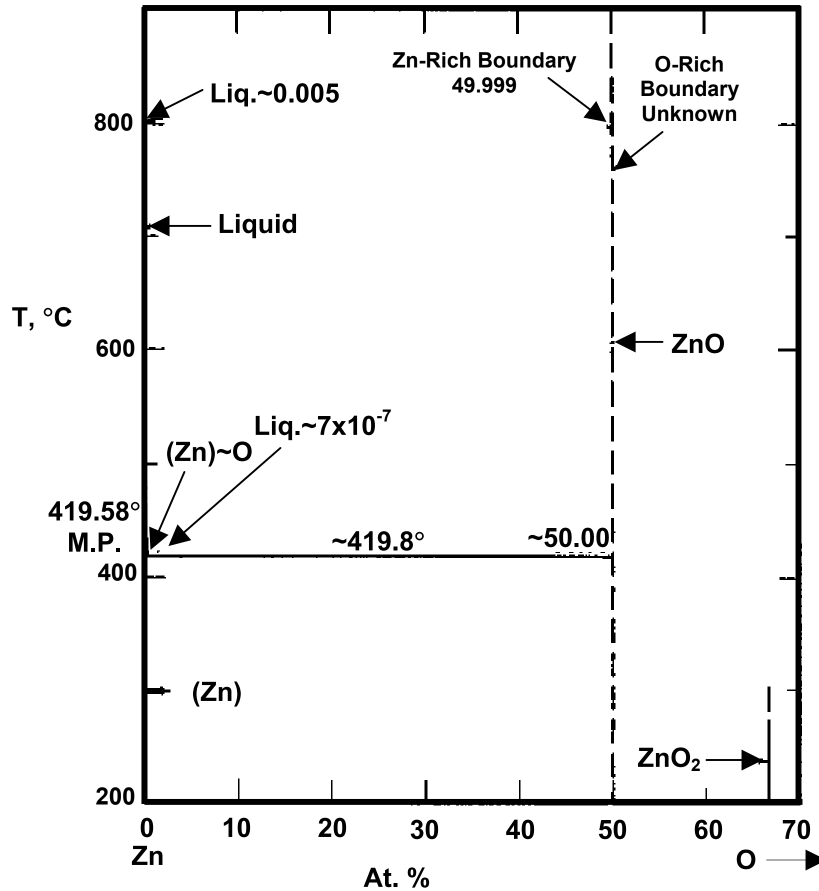

Figure 2.12 T-X diagram for condensed Zn-O system at 0.1 MPa [42]

ZnO crystals are composed of alternate layers of zinc and oxygen atoms disposed in a wurtzite hexagonal close-packed structure with a longitudinal axis (c-axis) as shown in Figure 2.13. The oxygen atoms (ions) are arranged in close hexagonal packing, with zinc ions occupying half the tetrahedral interstitial positions with the same relative arrangement as the oxygen ions. In this crystal structure, both zinc and oxygen ions are coordinated with four ions of the opposite charge, and the binding is strong ionic type. Owing to the marked difference in size, these ions fill only about 44% of the volume in a ZnO crystal leaving some relatively large open spaces (0.095 nm). Typical properties of ZnO are listed in Table 2.2 [44, 45, 46] and Ellingham diagram including ZnO is shown in Figure 2.14 [47].

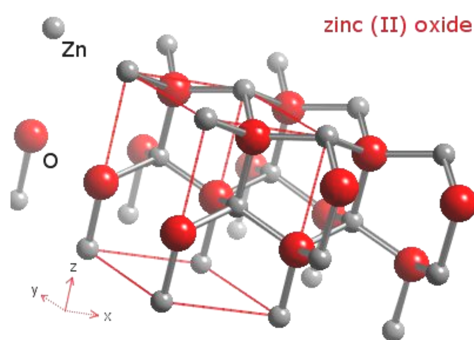

Figure 2.13 Many properties of zinc oxide are dependent upon the wurtzite hexagonal, close-packed arrangement of the Zn and O atoms, their cohesiveness and void space (www.webelements.com).

Table 2.2 Properties of zinc oxide

Crystal structure	Hexagonal, wurtzite
Molecular weight	Zn:65.38, O:16 and ZnO:81.38
Lattice constant	a = 3.246 Å, c = 5.207 Å
Density	5.67 g/cm^3 or 4.21 x 10^{19} ZnO molecules/mm^3
Cohesive energy	E_{coh} = 1.89 eV
Melting point	T_m = 2250 °K under pressure
Heat of fusion	4, 470 cal/mole
Thermal conductivity	25 W/mK at 20 °C
Thermal expansion coefficient	4.3 x 10^{-6} / °K at 20 °C 7.7 x 10^{-6} / °K at 600 °C
Band gap at RT	3.37 eV
Refractive index	2.008
Electron and hole effective mass	m_e^* = 0.28, m_h^* = 0.59
Debye temperature	370 °K
Lattice energy	964 kcal/mole
Dielectric constant	ε_0 = 8.75, ε_∞ = 3.75
Exciton binding energy	E_b = 60 meV
Pyroelectric constant	6.8 Amp./sec/cm^2/°K x 10^{10}
Piezoelectric coefficient	D_{33} = 12 pC/N

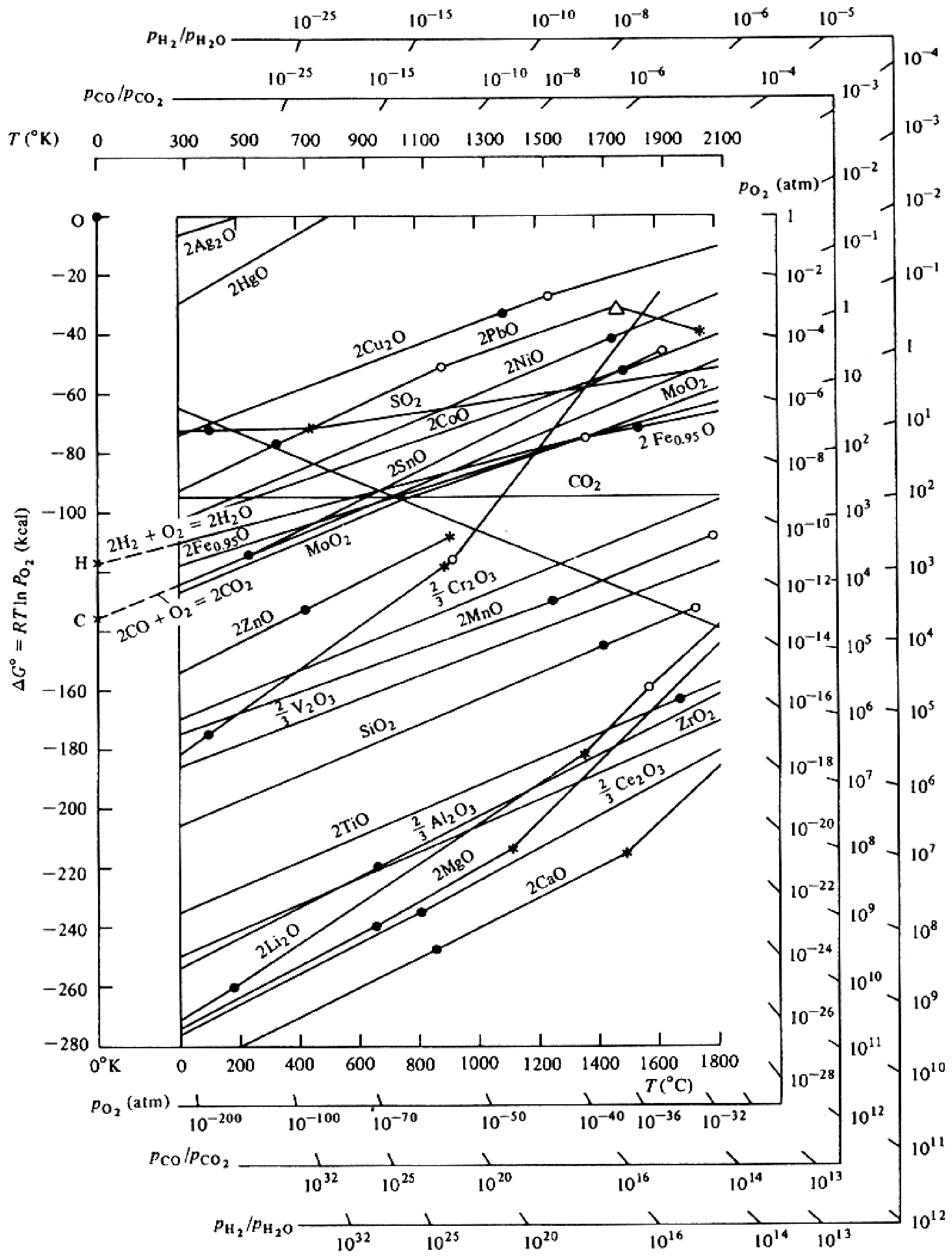

Figure 2.14 The Ellingham diagram for oxides [47]

Pure zinc oxide, carefully prepared in a laboratory, is a good insulator; however, it can be increased in electrical conductivity many fold by special heat treatments and by the introduction of specific impurities into the crystal lattice. ZnO can even be made to exhibit metallic conductivity as for transparent electrodes similar to ITO. In general, 0.5-1% additions of trivalent cations (e.g. Al and Cr) decrease the resistivity of ZnO by about 10 orders of magnitude. [46].

2.4.2 Defects chemistry

Many properties of crystals, most particularly electrical, are determined by imperfections, e.g. defects. Point defects are defined as deviations from the perfect atomic arrangement: missing ions, substituted ions, interstitial ions and their associated valence electrons as shown in Figure 2.15. A principal difference between point defects in ionic solids and those in metals is that in the former, all such defects can be electrically charged. Ionic defects are point defects that occupy lattice atomic positions, including vacancies, interstitial and substitutional solutes. Electronic defects are deviations from the ground state electron orbital configuration of a crystal, formed when valence electrons are excited into higher orbital energy levels. Such an excitation may create an electron in the conduction band and/or an electron hole in the valence band of the crystal. In terms of spatial positioning, these defects may be localized near atom sites, in which case they represent changes in the ionization state of an atom, or may be delocalized and move freely through the crystal.

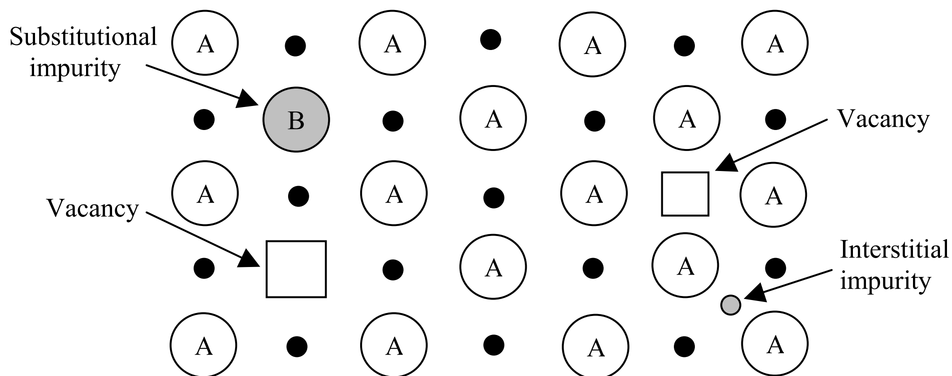

Figure 2.15 Various types of point defects in crystalline materials

An equivalent way to view the formation of defects is as a chemical reaction, for which there is the equilibrium constant. Defect chemical reactions for the formation of defects within a solid must obey mass, site and charge balance. In this respect they differ somewhat from ordinary chemical reactions, which must obey only mass and charge balance. Site balance means that the ratio of cation to anion sites of the crystal must be preserved, although the total number of sites can be increased or decreased.

For example, the Schottky disorder for NaCl and Frenkel disorder for ZnO, respectively, can be written using Kröger-Vink notation as:

$$null = V_{Na}^{'} + V_{Cl}^{\bullet} \quad (2.10)$$

and

$$Zn_{Zn}^{X} = Zn_{i}^{\bullet\bullet} + V_{Zn}^{''} \quad (2.11)$$

where null indicates the creation of defects from a perfect lattice. The respective mass-action equilibrium constants are:

$$K_{Schottky} = [V_{Na}^{'}] \cdot [V_{Cl}^{\bullet}] \quad (2.12)$$

and

$$K_{Frenkel} = [Zn_{i}^{\bullet\bullet}] \cdot [V_{Zn}^{''}] \quad (2.13)$$

The brackets denote concentration, usually given in mole fraction. Writing the equilibrium constant as the product of concentrations implies that the thermodynamic activity of each defect is equal to its concentration. The free energies for these quasichemical reactions are simply the Schottky or Frenkel formation energy, and the equilibrium constant is given by:

$$K_{Schottky} = K_{S}^{\circ} \exp\left(-\frac{\Delta \mathrm{H}_{S}}{kT} \right) \quad (2.14)$$

and

$$K_{Frenkel} = K_{F}^{\circ} \exp\left(-\frac{\Delta \mathrm{H}_{F}}{kT} \right) \quad (2.15)$$

The equilibrium constant is a function of temperature only and the product of the cation and anion vacancy concentrations is a constant at fixed temperature. Furthermore, when only intrinsic defects are present, the concentration of anion and cation vacancies must be equal for charge neutrality considerations,

$$[V_{Na}^{'}] = [V_{Cl}^{\bullet}] = K_S^{\circ 1/2} \exp\left(-\frac{\Delta H_S}{2kT}\right) \quad (2.16)$$

and

$$[Zn_i^{\bullet\bullet}] = [V_{Zn}^{''}] = K_F^{\circ 1/2} \exp\left(-\frac{\Delta H_F}{2kT}\right) \quad (2.17)$$

In Kröger-Vink notation, free electrons and holes do not themselves occupy lattice sites. The process of forming intrinsic electron-hole pairs is excitation across the bandgap, which can be written as the intrinsic electronic reaction:

$$null = e^{'} + h^{\bullet} \quad (2.18)$$

The equilibrium constant for this reaction is:

$$K_e = n \cdot p = [e^{'}] \cdot [h^{\bullet}] = Nc \cdot Nv \cdot \exp\left(-\frac{E_g}{kT}\right) \quad (2.19)$$

where Nc and Nv are the density of state of conduction band and valence band, respectively, and E_g is the energy band gap of materials.

When electrons and holes are tightly bound to an ion, or otherwise localized at a lattice site, the whole is considered to be one ionic defect. Thus, the valence state of defects such as vacancies and interstitials can vary. For instance, an oxygen vacancy can in principle take on different valence states ($V_O^{\bullet\bullet}, V_O^{\bullet}$, and V_O^X), as can cation interstitials, e.g., $Zn_i^{\bullet\bullet}, Zn_i^{\bullet}$ and Zn_i^x in the wurtzite structure compound ZnO.

Equilibration of ionic solids with an ambient gas plays an important role in determining defect structure. For example, the reduction of ZnO can be written as the removal of oxygen to the gas phase leaving behind doubly charged oxygen vacancies or cation interstitials:

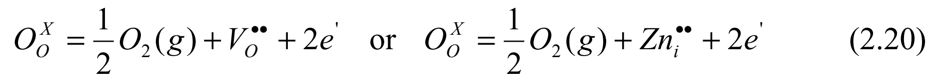

$$O_O^X = \frac{1}{2} O_2(g) + V_O^{\bullet\bullet} + 2e^{'} \quad \text{or} \quad O_O^X = \frac{1}{2} O_2(g) + Zn_i^{\bullet\bullet} + 2e^{'} \quad (2.20)$$

The equilibrium constant for the creation of double ionized oxygen vacancies is:

$$K_R = n^2 \cdot [V_O^{\bullet\bullet}] \cdot P_{O_2}^{1/2} = K_R^0 \cdot \exp\left(-\frac{E_R}{kT}\right) \quad (2.21)$$

In ZnO, the electron is a major electronic charge carrier. Thus, the conductivity of ZnO is:

$$\sigma \propto n = 2 \cdot [V_O^{\bullet\bullet}] = 2 \cdot (2K_R^0)^{1/3} \cdot \exp\left(-\frac{E_R}{3kT}\right) \cdot P(O_2)^{-1/6} \qquad (2.22)$$

With background acceptor,

$$[A'] = 2 \cdot [V_O^{\bullet\bullet}] \qquad (2.23)$$

The conductivity of ZnO is:

$$\sigma \propto n = \{(2K_R^O)^{1/2} \cdot \exp\left(-\frac{E_R}{2kT}\right) \cdot P(O_2)^{-1/4} \cdot [A']^{-1/2} \qquad (2.24)$$

Also, the reduction of ZnO can be expressed by creating single charged oxygen vacancies or cation interstitials:

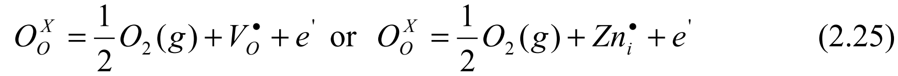

$$O_O^X = \frac{1}{2}O_2(g) + V_O^{\bullet} + e' \text{ or } O_O^X = \frac{1}{2}O_2(g) + Zn_i^{\bullet} + e' \qquad (2.25)$$

The equilibrium constant for the creation of single ionized oxygen vacancies is:

$$K_R = n \cdot [V_O^{\bullet}] \cdot P_{O_2}^{1/2} = K_R^0 \cdot \exp\left(-\frac{E_R}{kT}\right) \qquad (2.26)$$

Thus, the conductivity of semiconducting ZnO in which single ionized oxygen vacancies are dominant is:

$$\sigma \propto n = [V_O^{\bullet}] = (K_R^0)^{1/2} \cdot \exp\left(-\frac{E_R}{2kT}\right) \cdot P(O_2)^{-1/4} \qquad (2.27)$$

With background acceptor,

$$[A'] = [V_O^{\bullet}] \qquad (2.28)$$

The conductivity of ZnO is:

$$\sigma \propto n = \{K_R^O) \cdot \exp\left(-\frac{E_R}{kT}\right) \cdot P(O_2)^{-1/2} \cdot [A']^{-1} \qquad (2.29)$$

Thus, investigating the conductivity of ZnO in reducing environments can assist in determining the valence state of defects and the activation energy for releasing electrons.

Substituted foreign atoms can also enhance the semiconducting properties of ZnO. In the presence of selected metallic vapors at elevated temperatures, the foreign metallic atom replaces a portion of the Zn atoms. The zinc atoms, on release from their lattice positions, diffuse to the crystal surface where they are vaporized. This substitution process can substantially alter the crystal properties, depending upon the nature,

concentration and valence of the foreign atom. Optical and electrical properties are two of the several areas that can be readily modified.

Quantitative investigations concerning the diffusion of defects have been performed in sintered and single crystal ZnO [47, 49]. The diffusion of Zn in ZnO was observed during heating in a zinc vapor environment with the use of radioactive zinc. The diffusion coefficient of zinc was reported as 2~3 x 10^{-10} cm^2/sec in sintered tablets and around 4 x 10^{-11} cm^2/sec in single crystal at 1000 ºC [47]. The oxygen diffusion in ZnO was utilized by a gaseous exchange and a depth profile techniques. Tomlins et al [49] measured the diffusivity and activation energy of the oxygen vacancy in single crystal ZnO by analyzing the oxygen diffusion profile by secondary ion mass spectrometry (SIMS). They estimated the intrinsic activation energy of oxygen diffusion as 3.6-4.2 eV (Schottky formation enthalpy + migration enthalpy) and the diffusion coefficient at around 3 x 10^{-15} cm^2/sec at 1000 ºC. Also, they reported that diffusion of oxygen is slightly faster along the c-axis than along the a-axis direction of ZnO. (e.g. for ZnO from 3M, D (a-axis) ~ 4 x 10^{-7} *exp*(-2.22 eV/kT) cm^2/sec for and D (c-axis) ~ 9 x 10^{-6} *exp*(-2.52 eV/kT) cm^2/sec at 1000 ºC).

2.4.3 Sputtered ZnO thin films

In past years, many workers have investigated thin film fabrication processes for ZnO, including sputter deposition, chemical vapor deposition, evaporation, and sol-gel depositions. Among these processes, sputter deposition received much attention for the preparation of ZnO thin films for its advantages; low substrate temperatures (down to room temperature), good adhesion of films on substrates, high deposition rates, good thickness uniformity and high density, good controllability and long-term stability of the process, and easy fabrication of alloys and compound materials with different vapor pressures [50].

In most ZnO devices, the crystalline quality of the film is a key property. For example, ZnO films should have highly c-axis preferred orientation for application of longitudinal bulk wave transducers and SAW filters [51]. The crystalline quality, in particular the preferred orientation, depends on sputtering parameters and the nature of the substrate. Under optimized conditions, the c-axis orientation is frequently observed in

sputtered polycrystalline films even on a glass substrate. This is reasonably understood since the c-plane of the ZnO crystallites corresponds to the densest packed plane. The effect of sputtering parameters on the crystalline quality of ZnO films has been widely studied for piezoelectric, electronic, and photonic applications.

Lee et al [51] reported the dependence of the preferred orientation and grains size of sputtered ZnO films on film thickness. In general, the c-axis was well oriented normal to the substrate with thickness of less than 0.55 μm. However, as the film thickness increased, the (002) peak was reduced while other peaks such as (101), (110) and (112) appeared. For the thickness of 4.4 μm, the intensity of the (101) peak became as strong as that of (002) peak.

Chou and Liu [52] investigated the effect of excess Zn on the structure of ZnO films deposited by DC reactive sputtering with a Zn metal target. When oxygen was gradually increased, the color of the films changed from dark brown to yellowish brown, and finally to transparent due to the increase of O content in the films. Also, the XRD patterns changed from weakly crystallized to a highly oriented (002) ZnO structure as the Zn content decreased.

Zhang et al [53] also showed a significant increase in the film crystalline with the increase of the O_2/Ar gas ratio during sputtering due to a decrease in sputtering rate. Highly c-axis ZnO films were deposited onto silicon substrates by RF magnetron sputtering using a Zn metal target with 200 °C heating of the substrate. As the O_2/Ar gas ratio was increased, the intensity of the peak was increased and the value of FWHM was decreased (0.36° at $O_2/Ar = 2$ and 0.30° at $O_2/Ar = 3$). The effect of sputtering pressure on the crystallinity was also investigated [54, 55]. Zhu et al [55] observed that the decrease of sputtering pressure improved the crystalline quality because depositing particles with high kinetic energy resulted in high surface mobility.

Barker et al [56] deposited two ZnO films at room temperature with 90 and 180W of sputtering power respectively. Although the ZnO (002) peaks are similar, the film at lower power gave noticeably better crystallinity and less stress. Increasing the sputtering power obviously increased the atom flux at the substrate. This caused a decrease in the time available for adatoms to locate preferentially in the low-energy sites associated with the crystal before being immobilized by subsequently arriving atoms. The decrease in

adatom mobility also resulted in an increase of stress in the film. The adatom mobility can be improved by heating the substrate during sputtering. Thus, the ZnO film with higher substrate temperature shows better crystalline quality [57, 58].

Yoshino et al [59] investigated the effect of substrate on sputtered ZnO films using Al, Au, Ni, Cu and glass substrates. ZnO films on glass, Au and Al showed good c-axis orientation, while the orientation of films on Ni and Cu was rather disordered. Also, the orientation of ZnO films was disordered when the substrate surface was rough.

Gupta et al [60] studied the influence of post-deposition annealing on the structural and optical properties of ZnO films deposited at room temperature. As deposited ZnO films on quartz substrates exhibited compressive stress. The increase of post annealing temperature reduced this compressive stress and improved the crystallinity. After annealing at 400 ºC for 1 hour in air, the film became almost stress free, while annealing above 400 ºC induced tensile stress in the films as well as grain growth.

Doping with foreign elements is another method for controlling the properties of ZnO films. ZnO films doped with Al are important as a transparent electrode in flat panel displays given its high conductivity and good transparency. Thus, Al doped ZnO thin films have been intensively investigated to optimize the sputtering process conditions in order to obtain highly conducting, transparent, smooth and crystalline films. Figure 2.16 shows the phase diagram of the ZnO and Al_2O_3 binary system including ZnO-Al_2O_3 ($ZnAl_2O_4$) [61]. Most sputtered Al doped ZnO films show only a ZnO component since less than 2 wt% of Al is normally added as the n-type dopant.

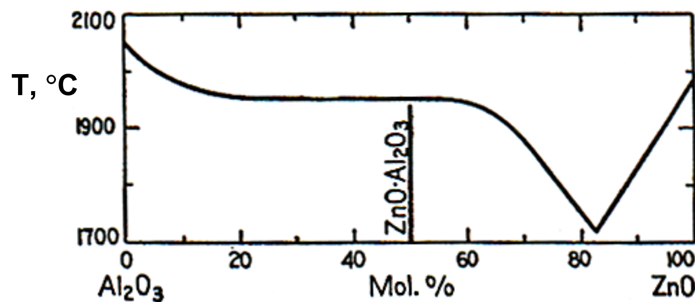

Figure 2.16 Phase diagram of ZnO-Al_2O_3 system [61].

The influence of the O_2/Ar ratio during sputtering on the properties of Al doped ZnO thin films were reported by Tsuji et al [62]. ZnO with 3 wt.% Al_2O_3 was used as a target and the ratio of O_2/Ar was varied from 0% to 3%. By adding a small amount of O_2 gas, the peak related to c-axis orientation from the (002) plane became weaker and the (100) and (101) peaks stronger. Meng et al [63] reported that the existence of Al_2O_3 grains deteriorated the c-axis orientation of sputtered ZnO thin films when using a Zn-Al alloy target.

Sieber et al [64] reported the microscopic characterization of reactively sputtered ZnO films with different Al-doping levels using co-sputtering from separate Zn and Al targets. At low Al concentration, typical columnar structure was observed. As the Al doping level increased, fine crystallites appeared on the substrate surface and columnar grains started growing onto them. Finally, the structure of ZnO films was changed to fine crystalline while the columnar structure was no longer found at the higher Al doping level (8.6 at%).

Haug et al [65] investigated the influence of deposition conditions on Al doped ZnO films using RF magnetron sputtering from a ZnO plus 2 wt% Al_2O_3 target. It was observed that ZnO films grown at high power density lose their strong preferred orientation in (002) direction and the (100) and (101) peaks appear At high power, the growth rate was high and donor type defects are produced due to the impinging ionized species which lowered the resistivity of ZnO films. Post annealing of these films removed the defect type donors leading to increased resistivity.

Sputtered Al doped ZnO thin films were also investigated to optimize their electrical and optical properties for transparency electrode applications. Ellmer [50] summarized the electrical properties of sputtered Al doped ZnO films based on a review of the literature; resistivity (ρ): $1.4 \times 10^{-4} \sim 7.7 \times 10^{-4}$ Ωcm, charge carrier concentration (N): $2.6 \times 10^{20} \sim 1.3 \times 10^{21}$ cm^{-3}, and mobility (μ): $10 \sim 60$ cm^2/Vs. The electrical properties of sputtered pure ZnO films were less investigated. Subramanyam et al [66] reported the electrical property of ZnO films deposited by reactive sputtering under highly reducing sputtering conditions. They obtained the following; resistivity (ρ): $3.2 \times 10^{-1} \sim 6 \times 10^{-2}$ Ωcm, charge carrier concentration (N): $7.8 \times 10^{17} \sim 5.4 \times 10^{18}$ cm^{-3}, and mobility (μ): $12.2 \sim 16.8$ cm^2/Vs. Mahmood et al [67] also report on RF reactive sputtered ZnO with a ZnO

target and 20% of oxygen ratio during sputtering; charge carrier concentration (N): 7.2 x 10^{20} cm^{-3} and mobility (μ): 57 ~ 131 cm^2/Vs. The electron mobility measured in sputtered polycrystalline ZnO films is still lower than the highest reported value for a bulk single crystal (230 cm^2/Vs) [68].

2.4.4 ZnO gas sensors

In 1959, Heiland reported on the gas sensitive behavior of ZnO's electrical conductivity [69]. The conductivity of thin layers of ZnO, for example, increased by orders of magnitude in vacuum and decreased in an atmosphere even at 500 ºK. From then, the detection of hydrogen, oxygen and hydrocarbon by means of surface conductivity changes on ZnO crystals and thin films has been proposed and demonstrated [69]. Although, SnO_2 has been intensively investigated fundamentally and commercially, ZnO is still attractive due to its easy fabrication in thin film form with various methods [15, 70-73] and its improved sensor performance by addition of dopants [14, 16, 74-80].

Bott et al [10] investigated the electrical conductivity changes of ZnO single crystals in CO, CH_4, and H_2 in air mixtures at 300 –500 °C using a constant voltage source. The ZnO single crystal sensors were sensitive to H_2 and CO with the maximum sensitivity at the temperature of around 400 °C but insensitive to CH_4. The ZnO sensors had the response time of about 2 min. They also observed the change of conductivity with the polycrystalline thick film and compressed disc type of ZnO [81]. CH_4 had much greater effects on the conductance of polycrystalline oxide than on those of single crystals.

The ZnO thick film sensor was investigated by Rao et al [13]. They prepared the calcined powders of undoped and doped ZnO with Pd, Fe and Ru for thick film NH_3 sensors. The Pd-ZnO exhibited good sensitivity and response time to NH_3 at room temperature.

The gas responses of chemically deposited ZnO films were investigated by Mitra et al [15]. A high sensitivity was observed for 3% vol. H_2 at the temperature of 150 °C. However, the sensor exhibited very poor recovery characteristics due the surface reduction of ZnO. The ZnO sensor showed higher sensitivity to liquid petroleum gas (LPG) in the 0.4-1.6 vol.% concentration in air.

As discussed in chapter 2.1, the grain or crystallite size is one of the most important factors affecting sensing properties, especially sensitivity. Some groups have fabricated nano grain sized ZnO and tested it for gas sensitivity. Dong et al [70] prepared nanometer ZnO by the arc plasma method and showed that nano-ZnO exhibits higher sensitivity compared to coarse-grained ZnO and lower operating temperatures (200 – 300 °C). The nano-ZnO exhibited higher sensitivities to LPG and C_2H_2 than to H_2 and CO, and nano-ZnO with Fe and Ag additives showed high sensitivity and excellent selectivity to H_2 against C_2H_2, CO and LPG, and the response time with less than 15 sec at 150 °C. Xu et al [71] also investigated the grain size effect on the sensor responses to H_2, C_4H_{10} and C_2H_5OH. It is reported that the smaller grain size of pure ZnO has higher gas sensitivity.

The effect of film thickness on sensor performance was investigated by Chang et al [72]. They fabricated ZnO films using rf reactive sputtering on a SiO_2/Si wafer with variable thickness (65 nm to 390 nm). The best sensitivity and fastest response were obtained with the thinnest film (65 nm).

Dopants in ceramic materials usually affect the physical and electrical properties. Dopant elements commonly segregate to grain boundaries in polycrystalline ceramics and prohibit grain growth in subsequent annealing. Electrically, dopants generate ionic and electronic defects. These defect processes impact the position of the Fermi energy level which in turn is expected to influence the gas sensitivity of the semiconducting oxides. Thus, nonstoichiometric ZnO prepared by various fabrication methods and with various dopants have been investigated to reveal the influences of composition on gas sensitivity.

One of the important dopants for sensor performance of ZnO is aluminum (Al), which acts as a donor. Nanto et al [14, 74] reported that an Al doped ZnO gas sensor could be applied to the fish processing industry. Doping a sputtered ZnO thin film with Al was effective in improving the sensitivity and selectivity of the sensor for exposure to odor from seafood as well as trimethylamine (TMA) and dimethylamine (DMA) gases. TMA and DMA gases are known to be created during the deterioration of fish. Thus, Al doped ZnO sensors were suggested to monitor the freshness of seafood in an inexpensive and a rapid non-destructive manner. They also showed [75] that the resistance change of Al doped ZnO films after exposure to ammonia gas (200 ppm) is about three times as large as that of un-doped ZnO. Mukhopadhyay et al [76] reported Al doped ZnO to have

good sensitivity to H_2. The other dopants, lanthanum (La) [16], tin (Sn) [77], molybdenum (Mo) [78], antimony (Sb) [79], and calcium (Ca) [80] have also been studied for improving the gas sensing performance of ZnO.

Stambolova et al [16] fabricated SnO_2 and ZnO thin films doped with 0-7 at. % La by spray pyrolysis and investigated the sensor response to 1.5 vol.% ethanol vapor in air. ZnO doped with 3% La showed much higher sensitivity than 3% La doped SnO_2 films and both films exhibited very short response time and recovery time (less than 60 sec) at 300 °C. It was suggested that La doping decreased the size of crystallite on the surface of films, resulting in the enhancement of ethanol sensitivity.

The SnO_2 content dependence of the sensitivity of sputtered Sn doped ZnO thin film was studied by Nanto et al [77]. The SnO_2 doped ZnO film (78 wt. %) exhibited a high sensitivity and good selectivity for C_2H_5OH gas.

Dayan et al [78] investigated the sensor response of Mo doped ZnO thick films to H_2, CO and CH_4. The MoO_3 doped ZnO (7 wt. %) thick film sensors exhibited higher sensitivity to H_2 than CO and CH_4. They also studied the effect of Sb doping on sensor response of ZnO thick films. The Sb doped ZnO films showed the higher sensitivity to H_2, CO and CH_4 gases than undoped ZnO sensors [79]. Table 2.3 summarizes previous research on ZnO gas sensors.

In spite of extensive research on ZnO gas sensors using various sensor types, target gases and dopants, the fundamental understanding of the sensing properties of semiconducting oxides including SnO_2 is still poor since the focus has been on the empirical optimization of sensor performance. Even though semiconducting oxide thin films have been actively investigated for practical applications, systematic studies related to the sensing mechanisms of thin film sensors is still required. Therefore, in this study, the influence of thin film processing conditions on the properties and sensor performance was investigated systematically. Especially, AC impedance spectroscopy with and without apply bias was utilized to assist in identifying the individual contributions to the sensor response. Most sensor investigations including SnO_2 have been performed using simple DC resistance measurements alone which are inadequate in identifying the key sensor processes. This is why the basic understanding of gas sensing is still immature in contrast to the widespread commercial applications. In particular, by utilizing AC

impedance spectroscopy in concert with DC bias, the resistance drift, on an extended time scale, was discovered and characterized.

Table 2.3 Previous research on ZnO gas sensors

Sensor type	Variable	Target gas	Ref
Single crystal		CO, CH_4, H_2	10
Thick film		CO, CH_4, H_2	80
Thick film	Undoped, Pd, Fe, Ru doped	NH_3	13
Thick film	Sb	CO, CH_4, H_2	79
Pellet	Undoped, Al	H_2	76
Thin film (CVD)		H_2, LPG	15
Thin film (Sputter)	Thickness, Al doped	CO	72
Thin film (Sputter)	Al	TMA, DMA	74
Thin film (Sputter)	Al	NH_3	75
Thin film (Sputter)	SnO_2 doped	C_2H_5OH	77
Thin film (Spray)	Undoped, La doped	C_2H_5OH, humidity	73
Nanometer	Fe, Ag	LPG, CO, C_2H_2, H_2	70
Nanometer	Grain size	SF_6, C_2H_5OH, C_4H_{10}, H_2	71

3. Experimental procedure

3.1 Processing

3.1.1 Semiconducting oxide film preparation

Undoped ZnO thin films were prepared by reactive DC magnetron sputtering (Supersystem II, Kurt J. Lesker Co.) from a Zn metal target. A Zn metal rather than a ZnO target, provides several advantages, including ready fabrication of high purity targets, high deposition rates and ability to achieve controlled stoichiometry (by variation of Ar/O_2 ratio), difficult to realize with oxide targets. To investigate the effect of the Ar to O_2 gas ratio on the microstructure of the undoped ZnO thin films, the oxygen concentration in the Ar/O_2 mixture was varied from 10 to 90%. The chamber was evacuated with rotary and cryo pumps. After reaching a pressure below 7×10^{-7} Torr in the sputtering chamber, Ar and O_2 gases were introduced into the chamber through two separate control valves. The working sputtering pressure was held constant at 5 mTorr and the DC power was maintained at 70W. After deposition, the ZnO films were annealed at 500 °C or 700 °C in air for 12 hrs. The deposition conditions are summarized in Table 3.1.

Table 3.1 Deposition conditions for undoped ZnO thin films

Target	Zn (99.99%), diameter: 2 inch
Power	DC 70W
Base pressure	$< 7 \times 10^{-7}$ Torr
Working pressure	5 mTorr
Target-substrate distance	10 cm
Substrate temperature	Unheated
Sputtering gas	Ar and O_2
Sputtering gas ratio (Ar: O_2)	1:9 to 9:1
Thickness	150 and 300 nm

Al doped ZnO films were fabricated by reactive RF magnetron sputtering using ZnO with 2 wt.% Al_2O_3 target at the same sputtering system. The RF power was 100W and

sputtering pressure was 10 mTorr with 20% of oxygen concentration in the Ar/O_2 mixture with 25 Å/min of deposition rate.

Film thickness was measured by a stylus profilometer (P10 Tencor Surface Profiler). Figure 3.1 shows the deposition rates of undoped ZnO and Al doped ZnO thin films produced with various Ar:O_2 ratios. Above an oxygen concentration of 40%, the deposition rate decreased abruptly and the undoped ZnO films looked transparent. The ZnO film at an oxygen concentration of 10% showed metallic properties and color. Based on these data, we selected three different deposition conditions for undoped ZnO films for investigating the performance of gas sensors (sample 3, 5 and 7).

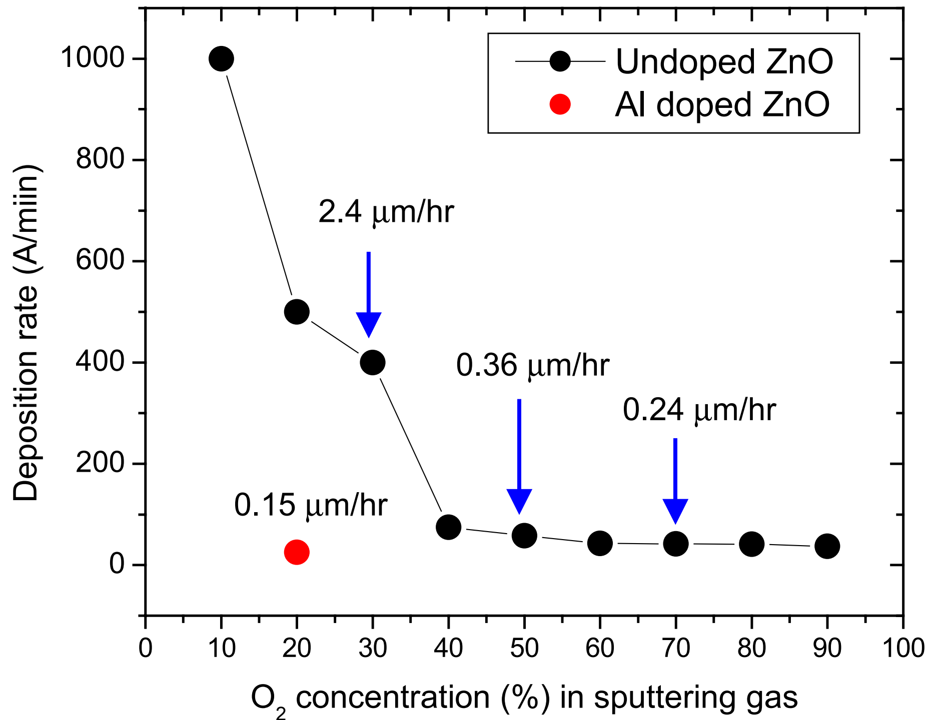

Figure 3.1 Deposition rates of sputtered ZnO thin films

The following other semiconducting oxide films, e.g. SnO_2, WO_3, CTO and V_2O_5 were investigated and compared with ZnO films. These oxides films were fabricated onto a micro array on Si-based wafer and onto a micromachined platform at the Fraunhofer-Institute Physical Measurement Techniques (IPM) in Germany.

CTO films were prepared by reactive e-beam evaporation, alternating between Cr and Ti layers. The individual thickness was adjusted to achieve the desired Cr/Ti ratio. CTO films were stabilized by annealing at 850 °C for one hour in synthetic air. The deposition and stabilization of the thin film CTO layer are described in detail elsewhere [32].

SnO_2 films, of 60 nm thickness, were deposited via RF magnetron reactive sputtering using a SnO_2 target. The SnO_2 may also be covered with Pt clusters of a few 10's of nm diameter. The Pt clusters act as catalyst in the surface reaction of various target gases. The stabilization conditions utilized for the thin film SnO_2 layers were 12 hours at 700 °C in air. The impact of Pt on the sensor properties of SnO_2 is described elsewhere [38].

The WO_3 deposition was performed by sputtering of a tungsten target under oxygen pressure using an Ar/O_2 gas ratio of 1. In order to achieve a well-defined crystal structure, a post annealing process was performed at 500 °C for one hour in a synthetic air atmosphere [38].

Deposition of the V_2O_5 layer was performed by electron beam evaporation of vanadium under controlled oxygen pressure. An oxidation treatment at 500 °C in synthetic air for one hour was performed to completely oxidize the films to the desired V_2O_5 stoichiometry. [82].

3.1.2 Micro array gas sensors

A schematic of the gas sensor chip with 2 x 2 micro arrays is illustrated in Figure 3.2. A silicon wafer was used as substrate with a 1 µm thick SiO_2 film to insulate the gas sensing elements from the substrate. A 200 nm thick Pt film with a 25 nm adhesion layer (Ta) was deposited and patterned to act as buried bottom electrodes, heater and temperature sensor. For operating temperatures of 300-500 °C, around 2 Watt of power was needed. A sufficient uniformity of temperature is ensured by the high thermal conductivity of the silicon substrate (150 Wm/K) [32].

The layout shown in Figure 3.2 enables the deposition of four different sensing elements by discrete processes. Thus, this offers the possibility of multi gas analysis by pattern recognition methods.

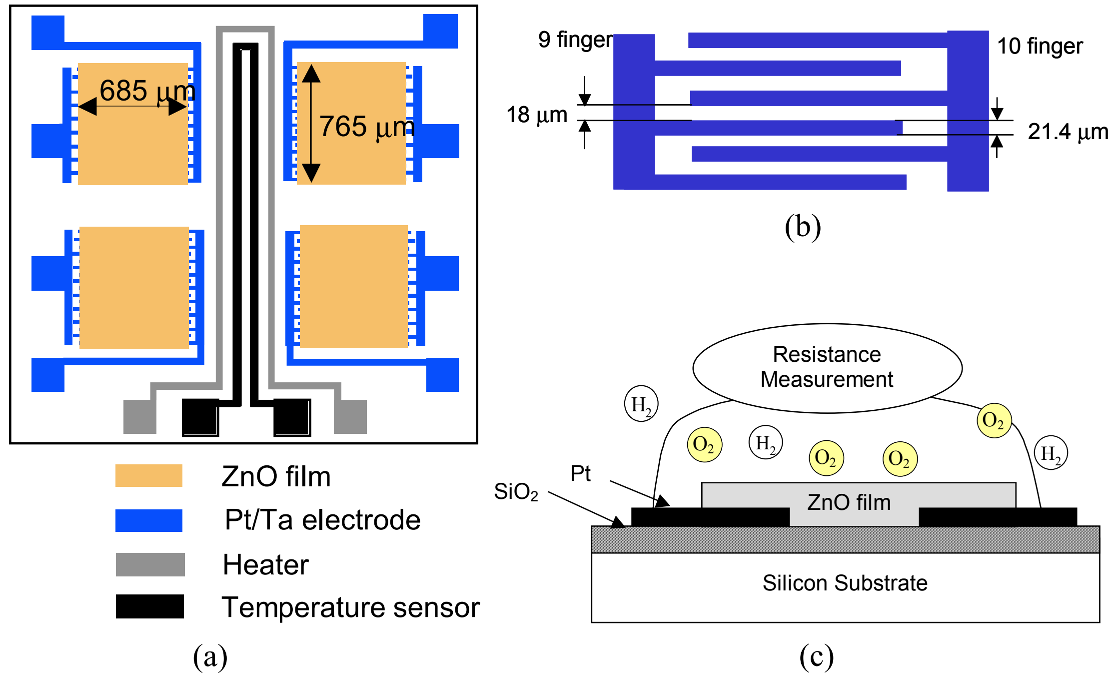

Figure 3.2 (a) Top view of zinc oxide thin film array with four sensing elements (765 x 685 µm). The chip size is 9 mm^2. The layout shows the interdigital electrodes, heater and temperature sensor which are composed of Pt/Ta films. (b) Pt/Ta interdigited bottom electrodes with 18 µm distance (c) Schematic of ZnO gas sensor structure

Figure 3.3 shows the Fraunhofer-IPM standard fabrication process of micro arrays. Silicon wafers (4 inch) were used as substrates and a 1µm silicon oxide film was grown by thermal oxidation to insulate the substrate material from the gas sensing materials. Electrodes, heater and temperature sensor were fabricated in two-step processes.

A sacrificial Al layer was used to improve the lift off process of the Pt/Ta multilayers by formation of over-hang structures. Also the smooth edges of the Pt/Ta layers resulting from the lift-off process, were suitable for semiconducting oxide growth. The 280 nm thickness of the Al layer was deposited on the substrate by e-beam evaporation. Onto the Al layer, a photoresist was spin coated and patterned by a photolithography process. Through the patterned photoresist, the Al layer was over-etched by chemical wet etching to make the over-hang structures which were suitable for

lift-off. Thermally evaporated Pt (200 nm) and Ta (25 nm) materials were deposited on the surface of the Al and photoresist layers. To achieve a good adhesion of the Pt film, a Ta adhesion layer was deposited prior to the Pt evaporation. After the deposition of the Pt/Ta layers, the photoresist and the Al sacrificial layer were removed by chemical etching. For the patterning of gas sensing oxide layers onto the electrodes, the lift-off method was also used. However, this time, only the photolithography step was used without using an Al sacrificial layer since the oxide films were easily patterned using the lift-off method.

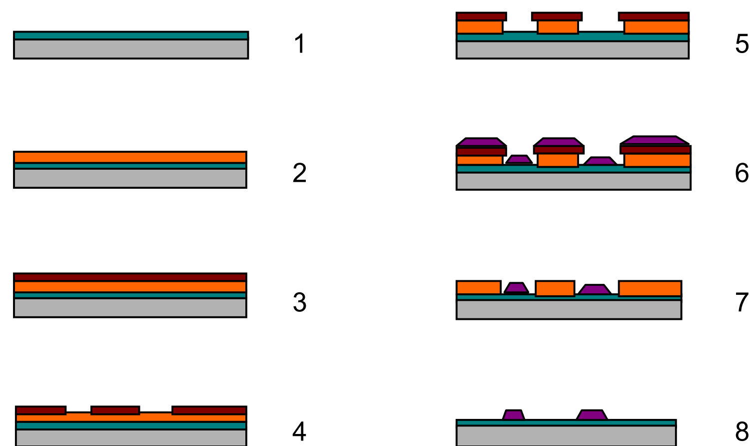

Figure 3.3 Process steps for Pt/Ta metallization (1) Si/SiO_2 wafer, (2) aluminium layer by e-beam evaporation, (3) spin coated photoresist, (4) photoresist patterned by photolithographic process, (5) wet etched aluminium layer, (6) deposition of Pt/Ta multi layers, (7) lift off process, and (8) removal of the sacrificial aluminium layer [32]

For each oxide deposition process, only one window of the photoresist was opened; thus only one sensing element was deposited during each lift-off process. After deposition, the photoresist was removed and then, the oxide was stabilized by a suitable annealing process. The sensitive oxide layer requiring the highest stabilizing temperature was patterned and annealed first. Thus, CTO was first patterned and annealed due to its highest annealing temperature process. Figure 3.4 shows the photo of the mounted gas sensor micro arrays without the metal cap. It shows the distinct different colors of each of the four semiconducting oxide gas sensing elements (SnO_2, WO_3, CTO and V_2O_5).

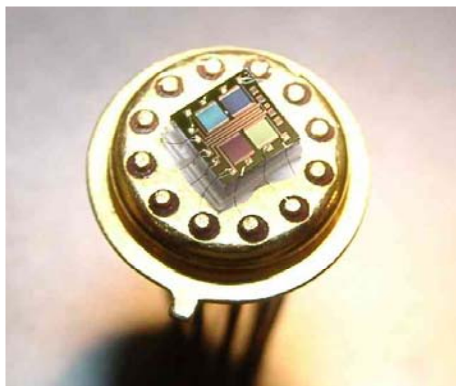

Figure 3.4 A photo of mounted multi oxide micro array sensor with four gas sensing elements; SnO_2, WO_3, CTO and V_2O_5.

For the study of ZnO gas sensor performance, ZnO films were deposited onto micro array platforms unheated during sputtering to prevent thermal damage of the patterned photoresist. ZnO films with three different oxygen concentrations in the Ar-O_2 mixture (30, 50 and 70%) during sputtering and Al doped ZnO films were chosen to investigate the effect of deposition conditions on the microstructure and gas response. All four sensing elements were deposited under the same deposition conditions. After the ZnO films were patterned using the lift-off process by removal of the photoresist, they were annealed at 500 °C or 700 °C in synthetic air for 12 hours. Table 3.2 lists the key components of the ZnO gas sensor chips.

Table 3.2. Key components of the micro array ZnO gas sensor

Element	Role
ZnO (300 nm)	Gas sensing layer • Sputtering gas ratios (Ar:O_2 = 7:3, 5:5, and 3:7) • Al doping • Post annealed at 500 °C and 700 °C for 12 hrs
Pt (200 nm)	Bottom electrode, heater and temperature sensor
Ta (25 nm)	Adhesion layer
SiO_2 (1 μm)	Insulating layer
Si wafer	Substrate

The diced chips were glued into a 12-polar TO5-housing using a ceramic cement with high temperature stability. A glass spacer was used to achieve thermal isolation of the chip against the metal housing. The pins of the package were connected to the chip using 35 μm thick gold wires by ultrasonic bonding. The package was closed by a metal cap with a built-in wire mesh to enable gas exchange with the environment. Figure 3.5 shows a schematic cross sectional view and a photo of the mounted sensor chips.

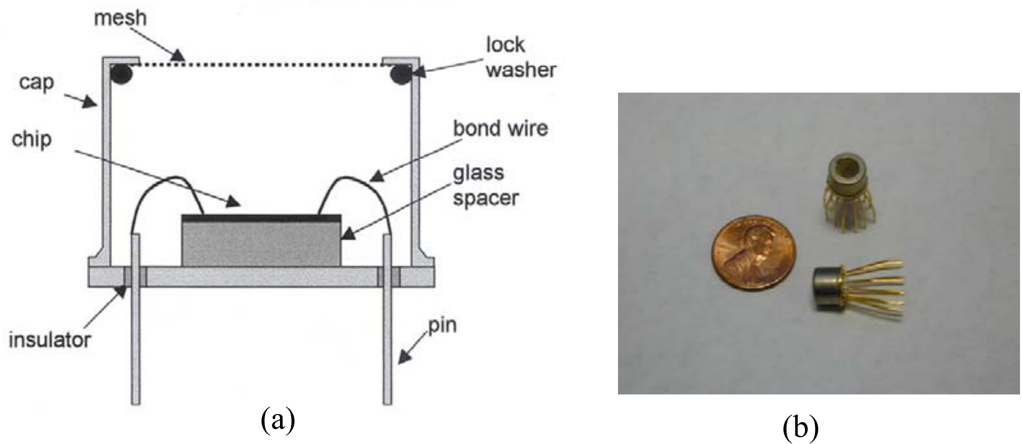

Figure 3.5 (a) A schematic cross sectional view of the mounted sensor chip and (b) a photo of the mounted sensor chips

For comparison, Fraunhofer-IPM's SnO_2 micro array gas sensor with micromachined membrane platforms was examined for its gas sensor performance. Figure 3.6 (a) shows the design of the 2 x 2 micro arrays. The micromachined membrane platform mainly consisted of a bulk micromachined boron doped silicon wafer and low stress silicon nitride layer (180 nm). A 200 nm thick Pt film with a 20 nm adhesion layer was deposited and patterned to act as buried bottom electrodes, heater and temperature sensor. SnO_2 films were deposited by sputtering. For operating temperature of 300 - 500 °C, less than 5 mW of power was needed. The detailed fabrication procedure is found elsewhere [38]. Figure 3.7 shows a schematic of micro hotplate gas sensor and two photographs of the devices after chip dicing.

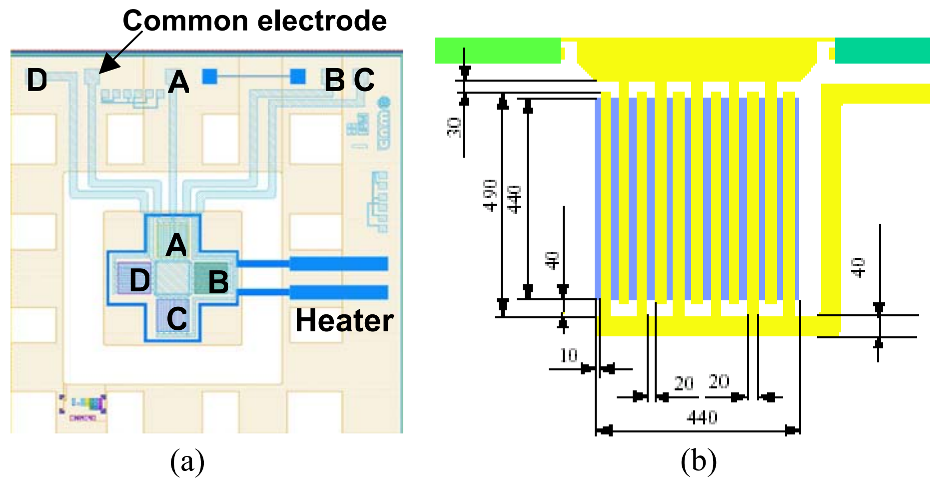

Figure 3.6 (a) Top view of micromachined micro array with four sensing elements and (b) Pt interdigited electrode with distance 20 μm [38]

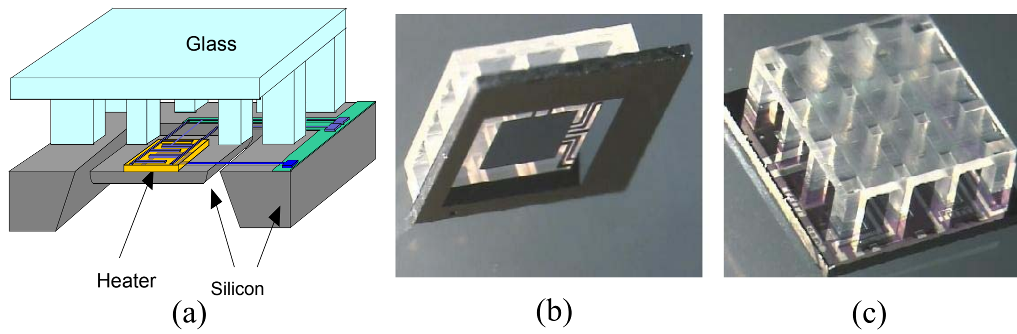

Figure 3.7 Micro array gas sensors with micromachined membrane platform and glass bridge (a) A schematic of micro hotplate gas sensor, (b) bottom view (c) top view

3.2 Physical and chemical analysis

The properties of the ZnO films were observed by optical microscopy, atomic force microscopy (Digital Instruments Nanoscope IIIa AFM), scanning electron microscopy (SEM, JEOL), and focused ion beam-scanning electron microscopy (FIB-SEM, FEI Dual Beam Focused Ion Beam System DB235) as well as by X-ray diffraction (XRD, Rigaku) with Cu Kα radiation, and wavelength dispersive X-ray spectrometry (WDS, JEOL JXA-733 Superprobe). XRD measurements were performed on ZnO films prepared in a similar manner on SiO_2 coated Si wafers. The XRD patterns of as-deposited and post annealed ZnO films were compared and characterized to find the influence of the deposition process on the microstructure, and eventually on the gas sensitivity of the ZnO films. FIB-SEM observation was performed on 700°C post annealed Al doped ZnO films on SiO_2 coated Si wafers. The cross section of ZnO films etched by Ga ion beams readily revealed the microstructure. AFM, SEM and WDS measurements were performed on ZnO films on gas sensor micro arrays after each annealing. Surface contact potential imaging by AFM was utilized for investigating the polarization effect induced by applying DC bias.

3.3 Electrical measurements for gas sensor performance

Figure 3.8 shows a schematic cross sectional view of the test chamber and photos of the mounted sensor chip and test chamber. As shown in figure 3.8 (a), the test chamber (1.5 x 4 x 1.375 in^3) made of transparent acrylic material, is a linear configuration with tapered shapes of the gas inlet and outlet regions. This arrangement and small volume reduces the dead volume of the reaction chamber, shortens gas exchange times and allows for more accurate measurement of the sensor response time. Four mounted sensor chips can be accommodated simultaneously and electrically connected outside using sensor sockets.

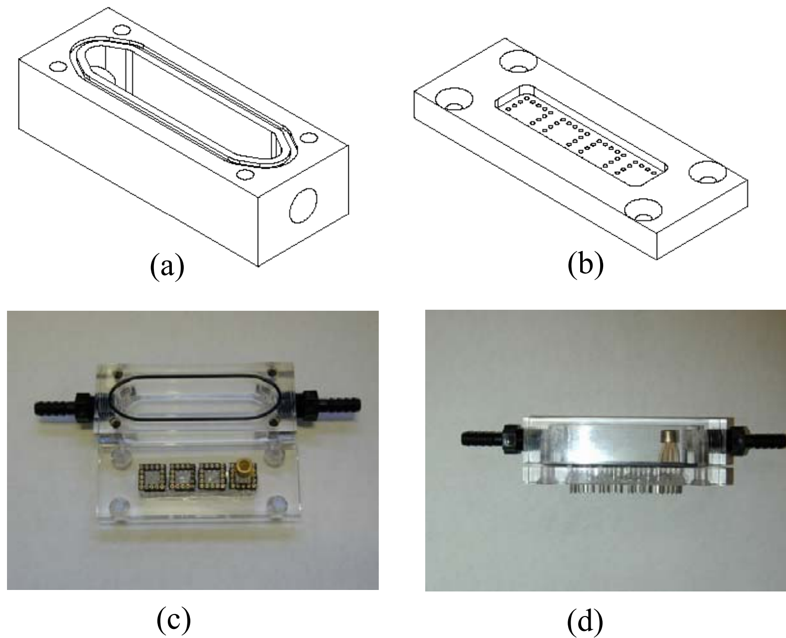

Figure 3.8 Schematic cross sectional view of test chamber (a) and cover (b), and photos of the mounted sensor chip and test chamber (c) and (d)

Figure 3.9 illustrates the gas sensor measurement set-up. The gas-mixing set-up utilized a mass flow controller (MKS 647A) with four channels and test gases. Table 3.3 shows the test gases used for gas response and polarization effect measurements. The gas flow rate was constant at 100 sccm for all measurements to avoid any problem with gas consumption by the sensor and to minimize problems with adsorption and desorption at the walls of pipelines and test chamber. Gas mixing was regulated by varying the gas

flow through mass flow controllers (MFC). For controlling the test gas concentrations, the gas flow was varied according to equation (3.1) [83],

$$C\ (\text{Component A}) = C\ (\text{Test gas A})\ \frac{V(A)}{V(Total)} \qquad (3.1)$$

For 100 ppm H_2 gas, for example, 10 sccm of H_2 (1000 ppm in air) and 90 sccm of dry air flowed through the MFC.

Table 3.3 Test gases for gas response and polarization effect measurements

Gas	Concentration	Role
Dry air		Carrier/reference
H_2	1000 ppm in air	Reducing
CO	1000 ppm in air	Reducing
NO_2	100 ppm in air	Oxidizing
Ar	99.999%	
O_2	0.01%, 0.1%, 1%, 10% in argon	

In nearly all applications there is always a certain amount of water vapor in the gas mixture. This may influence the sensor response, since almost all gas sensing oxides show some cross sensitivity to humidity. Considering this disturbing influence on the sensor response, it is important to enable the test gas mixture to be humidified [83]. The humidification of the test gases was done by adding humidified air using two separated gas flow controllers.

The response of semiconducting metal oxides to various gases has most commonly been investigated by DC current-voltage measurements. While DC measurements are sufficient for monitoring the overall response of gas sensors to various gases, they are inadequate in pinpointing the individual contributions from the grains, grain boundaries, and oxide/electrode interfaces. For purposes of understanding the source of gas sensitivity of a given specimen, it is important that each of these contributions be investigated separately. In this study, current-voltage (I-V) behavior (DC source monitor: HP 4142B) and AC impedance spectra (Impedance/Gain-Phase analyzer: Solartron SI 1260) were utilized and investigated. In particular, frequency dependent complex impedance measurements (frequency: 1 – 10^7 Hz, amplitude: 50 mV), both with and

without DC bias were performed to characterize and model the response of thin film ZnO on micro arrays to H_2, NO_2 and CO. Furthermore, time and DC bias dependent polarization/degradation effects of ZnO micro array sensors were investigated in dry air, H_2, Ar and various concentrations of O_2 in argon using AC impedance spectra measurements for long term analysis.

Current-Voltage analyses of ZnO films on micro arrays were also performed at room temperature in an open laboratory environment using a probe station (Karl Suss). During the measurements, abnormal I-V behavior (hysteresis, sweep rate dependence, etc) was found. For investigating these behaviors, ZnO films micro arrays were treated with alcohol, cleaned with D.I. water together with 500 °C annealing and overnight vacuum treatments.

For the performance comparison of micro array gas sensors, the DC resistance response of ZnO and the other oxides on micro arrays were examined to CO, H_2, CH_4 and NO_2 in synthetic air (80 % N_2 and 20% O_2, 50% R.H., at 25 °C) using a digital voltmeter (Keithley 2700) in the same test chamber at Fraunhofer-IPM.

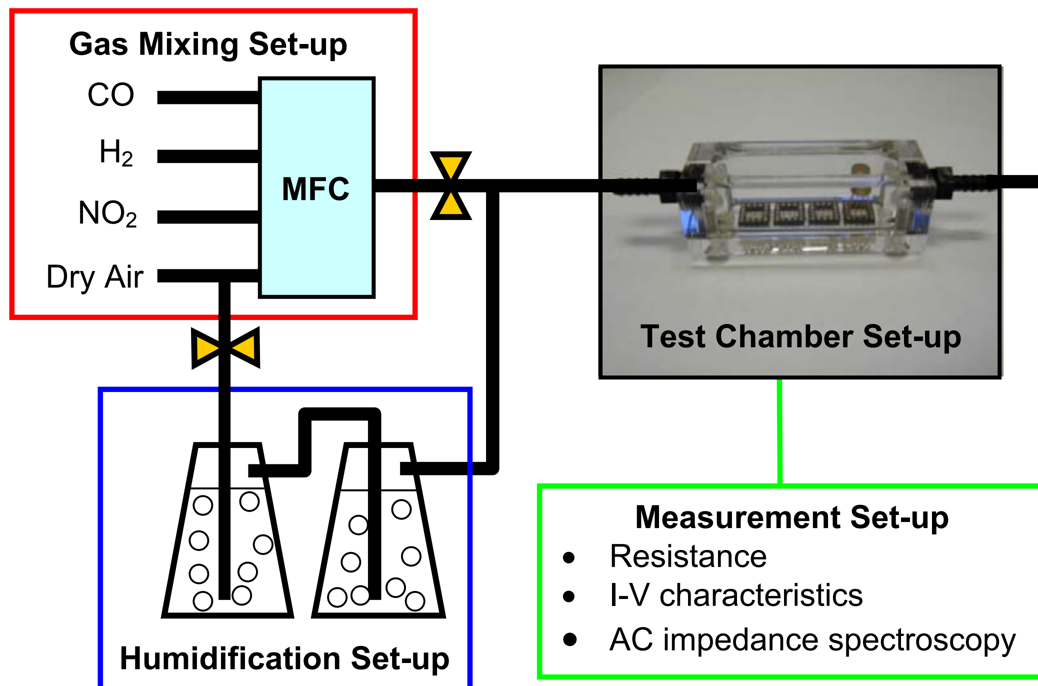

Figure 3.9 Gas sensor measurement setup

4. Result

4.1 Physical and chemical analysis

The patterned ZnO thin films and Pt interdigited electrodes are shown in Figure 4.1, demonstrating that the lift-off method is suitable to define these structures. Figure 4.2 shows the ZnO films on Pt electrodes before and after annealing at 700 °C for 12 hours in synthetic air. The sputtered ZnO film onto Pt bottom electrodes shows good step coverage.

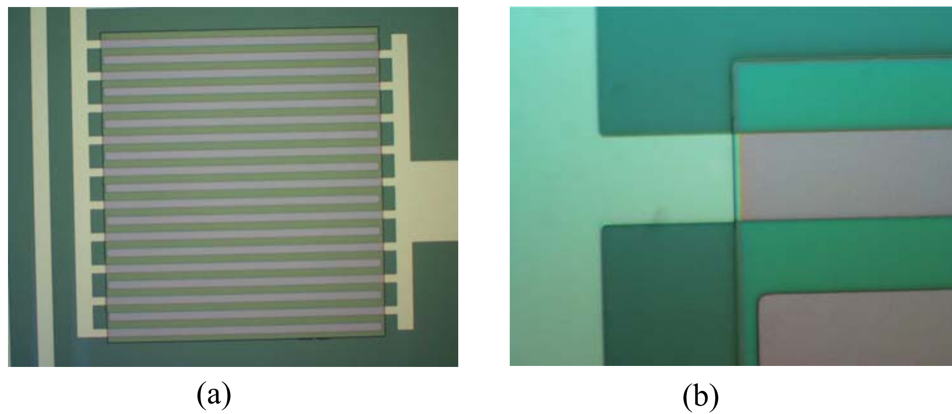

(a) (b)

Figure 4.1 Optical microscopy images of micro array sensor with patterned ZnO films

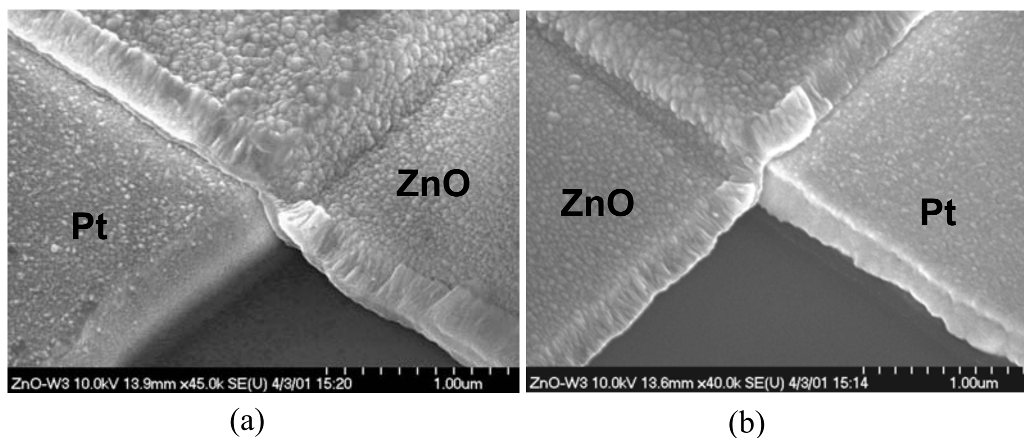

(a) (b)

Figure 4.2 SEM photographs of the ZnO film on Pt electrode (a) Before annealing and (b) After 700 °C annealing in synthetic air for 12 hours

The X-Ray Diffraction patterns (CuKα1, λ=1.5406 A) were obtained on various ZnO films on SiO_2 coated Si wafers prepared in a similar manner as the films on the micro arrays. Figure 4.3 shows the XRD patterns of undoped ZnO films with different Ar/O_2 ratios and the reference pattern of ZnO powder. All undoped ZnO films show c-axis orientation with the (002) plane parallel to the substrate since only one peak corresponding to the (002) plane is observed in the x-ray spectra. As the oxygen concentration during sputtering increases, the peak intensity and the sharpness of the peak increases. Thus, ZnO films deposited with higher O_2/Ar ratio have more highly oriented and well crystallized structures. For example, ZnO films with $Ar:O_2 = 3:7$ show an almost 10 times higher peak intensity of the (002) plane than the film with $Ar:O_2 = 7:3$; also slight higher intensity than that of ZnO film with $Ar:O_2 = 5:5$.

The post deposition annealing also affects the crystalline properties of sputtered ZnO films. With an increase of annealing temperature, ZnO films show better crystalline quality based on the increase of the peak intensity of (002) and the sharpness of the peak. Beside the profile of the peak, as deposited ZnO films show a shift in diffraction peak position of (002) from their normal powder derived value. As the annealing temperature increases, the peak's position shifts towards the powder value but slightly deviates from the powder value in the opposite direction. This indicates that post annealing changes the spacing between (002) planes, which are parallel to the c-axis. Table 4.1 lists the XRD parameters of pure ZnO films.

Figure 4.4 shows the spacing value (d) between (002) planes and the value of full width at half maximum (FWHM) for the (002) diffraction peaks. As one increases the annealing temperature, spacing of the planes and FWHM decrease. ZnO films annealed at higher temperature thus exhibit better crystalline quality. Also increasing O_2/Ar ratio, generally result in better crystalline quality.

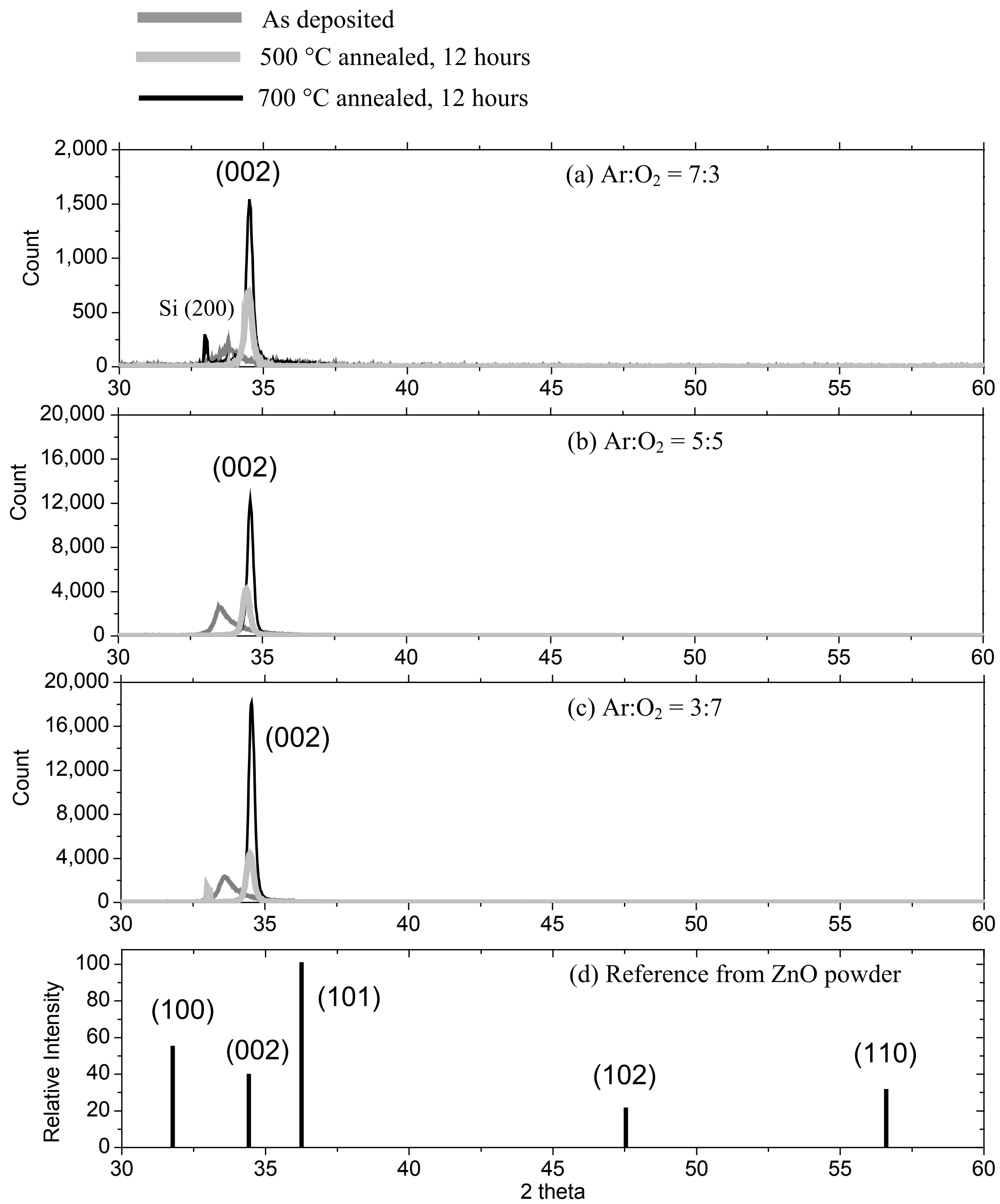

Figure 4.3 X-ray diffraction patterns of pure ZnO films (a) $Ar:O_2$ = 7:3, (b) $Ar:O_2$ = 5:5, (c) $Ar:O_2$ = 3:7, and (d) reference from ZnO powder

Table 4.1 XRD parameters of ZnO films deposited with various Ar/O_2 ratios

		2θ for (002) plane (°)	Intensity (Count)	Spacing d (A)	FWHM (°)
ZnO powder	Reference	34.419	-	2.604	-
ZnO (Ar:O_2 = 7:3)	As deposited	33.952	200	2.638	0.613
	500 °C annealed	34.482	688	2.599	0.323
	700 °C annealed	34.524	1,554	2.596	0.266
ZnO (Ar:O_2 = 5:5)	As deposited	34.104	2,480	2.627	0.712
	500 °C annealed	34.444	4,260	2.602	0.290
	700 °C annealed	34.555	12,388	2.594	0.248
ZnO (Ar:O_2 = 3:7)	As deposited	33.884	2,413	2.643	0.755
	500 °C annealed	34.496	4,463	2.598	0.288
	700 °C annealed	34.589	18,321	2.592	0.240

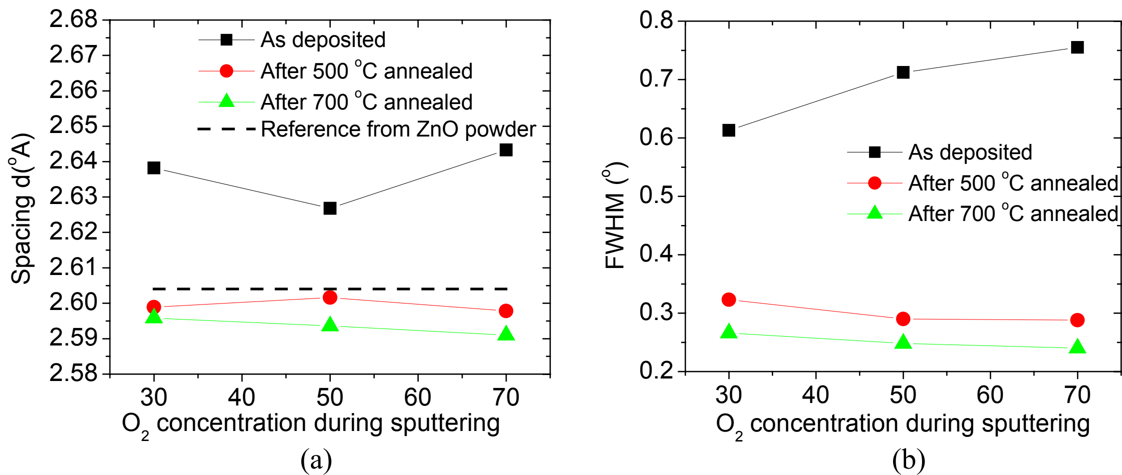

Figure 4.4 Characteristic parameters given by XRD from ZnO (002) planes. (a) Spacing and (b) Full width at half maximum (FWHM).

The shift of the position of the diffraction peak is mainly associated with the strain induced in the films [84]. This peak shift can be expressed using Bragg's law ($\lambda = 2d\sin\theta$). Figure 4.4 (a) shows the deviation of the spacing between (002) planes from that of unstressed ZnO powder. The d value for as deposited ZnO films is greater than that of ZnO powder. With the increase of annealing temperature, the d value is decreased to less than that of the powder value. It indicates that as deposited films are elongated along the c-axis, and compressive forces act in the plane of the ZnO films. The compressive stress becomes weaker as the annealing temperature increases, resulting in a decrease of d value between (002) planes. With increasing annealing temperature, the stress state of sputtered ZnO films shifts from compressive to tensile. Using the value (d) corresponding to the (002) planes of sputtered ZnO films and unstressed ZnO powder respectively, the strain induced along the c-axis and the stress in the plane of the film are approximately estimated by equation (4.1) and (4.2) [54], respectively, and are listed in Table 4.2.

$$\text{Strain } (e_{zz}) = (d_{\text{ZnO film}} - d_{\text{ZnO powder}}) / d_{\text{ZnO powder}} \quad (4.1)$$

$$\sigma = [2 \cdot C_{13} - (C_{11} - C_{12}) \cdot C_{33} / C_{13}] \cdot e_{zz} \quad (4.2)$$

The C_{ij} are the elastic stiffness constants and e_{ii} is the linear strain in the *i*th direction. The values of the stiffness constants for ZnO are $C_{11} = C_{33} = 2.1 \times 10^{11}$ N/m^2, $C_{12} = 1.2 \times 10^{11}$ N/m^2, and $C_{13} = 1.05 \times 10^{11}$ N/m^2 [54].

Table 4.2 Calculated stresses in the plane and strains along the c-axis of ZnO films

Stress (N/m^2) / *Strain*	As deposited	Annealed at 500 °C	Annealed at 700 °C
ZnO (7:3)	-6×10^9 / *0.01333*	7.97×10^8 / *-0.00177*	1.33×10^9 / *-0.00296*
ZnO (5:5)	-4.03×10^9 / *0.00895*	3.29×10^8 / *-0.00073*	1.71×10^9 / *-0.00380*
ZnO (3:7)	-6.88×10^9 / *0.01529*	9.86×10^8 / *-0.00219*	2.16×10^9 / *-0.00480*

Al doped ZnO films have very distinct XRD patterns compared to those of pure ZnO films as shown in Figure 4.5. Al doped ZnO films have weak (100) and (101) peaks and do not have the peak corresponding to the (002) plane easily found in undoped ZnO films. This suggests that Al doped ZnO films have crystalline structure with mixed

orientation. This crystalline structure of Al doped ZnO films remained after post deposition annealing since the (100) and (101) peaks have nearly the same intensity even after being annealed at 700 °C for 12 hours. The XRD parameters and calculated strains of Al doped ZnO films are summarized in Table 4.3.

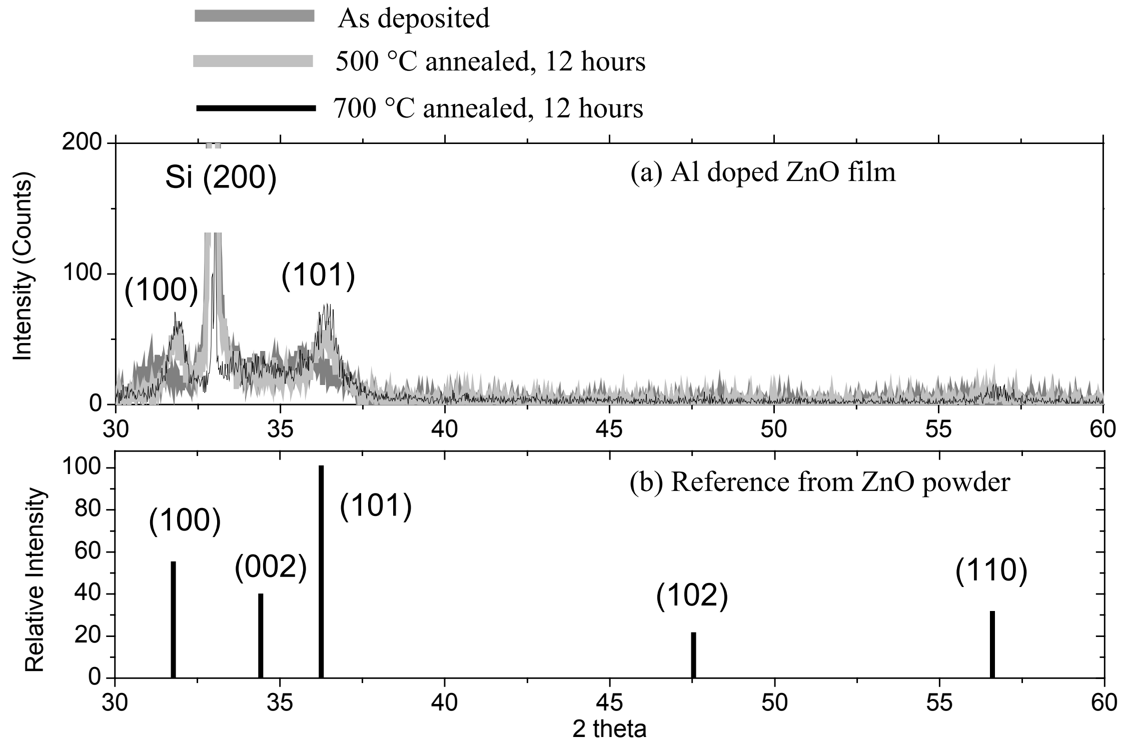

Figure 4.5 X-ray diffraction patterns of (a) Al doped ZnO films and (b) reference from ZnO powder

Table 4.3 XRD parameters and calculated strains of Al doped ZnO films

Plane	X-ray parameter	Reference from ZnO powder	Al doped ZnO films		
			As deposited	After 500 °C annealed	After 700 °C annealed
(100)	2θ (°)	31.771	31.299	31.767	31.853
	Intensity (Count)		38	58	71
	Spacing d (°A)	2.815	2.856	2.815	2.807
	FWHM (°)		0.785	0.471	0.49
	Strain (%)		1.468	0.011	-0.252

Al doped ZnO films also show the shift of peak position from that of ZnO powder. Calculated strains from the peak position are listed in Table 4.3. As deposited Al doped ZnO films are under compressive stress which changes to tensile after post deposition annealing. The decrease of the spacing value with annealing temperatures is shown in Figure 4.6 (a). The value of FWHM of Al doped ZnO films is decreased after 500 °C annealing, but increases somewhat after 700 °C annealing.

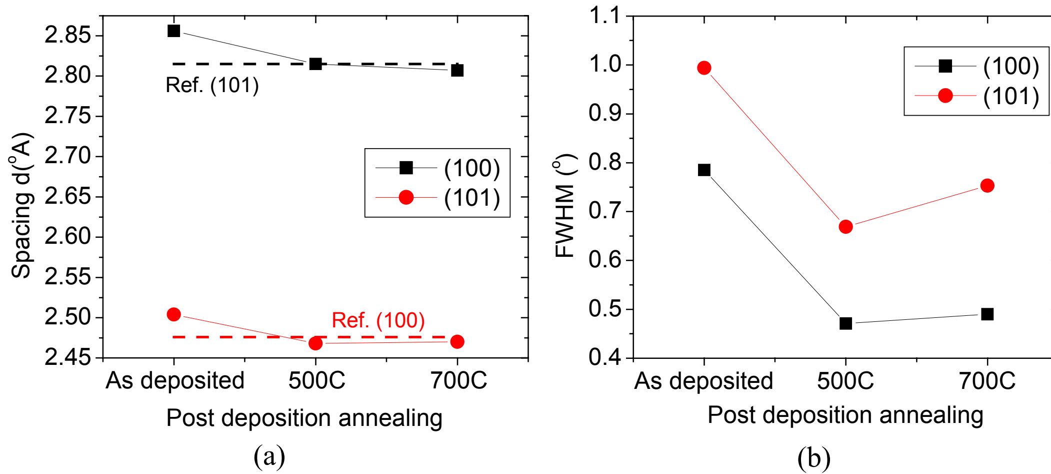

Figure 4.6 Characteristic parameters given by XRD from Al doped ZnO films. (a) Spacing and (b) Full width at half maximum (FWHM).

The ZnO films deposited onto micro array sensor platforms were observed using atomic force microscopy (AFM). Each ZnO film was post annealed at 500 °C and 700 °C in synthetic air for 12 hours except for the ZnO film with Ar:O_2 = 7:3, which was annealed only at 700 °C. The AFM images of Figure 4.7 shows the effect of deposition conditions, post deposition annealing and Al doping on the microstructure of the ZnO films. The grain size of undoped ZnO films increases with an increase in the concentration of oxygen in the Ar-O_2 mixture. Little change in microstructure was observed even after annealing at 700 °C in air for 12 hours. ZnO films prepared with Ar:O_2 = 7:3 have a surface roughness of Ra = 5.1 nm and grain size of 30 - 40 nm, while those prepared at Ar:O_2 = 3:7 have a smoother surface (Ra = 3.8 nm) and larger grain size of about 100 nm. ZnO films with Ar:O_2 = 5:5 have grain size intermediate between the

other two compositions. These behaviors correspond well to the XRD patterns of undoped ZnO films.

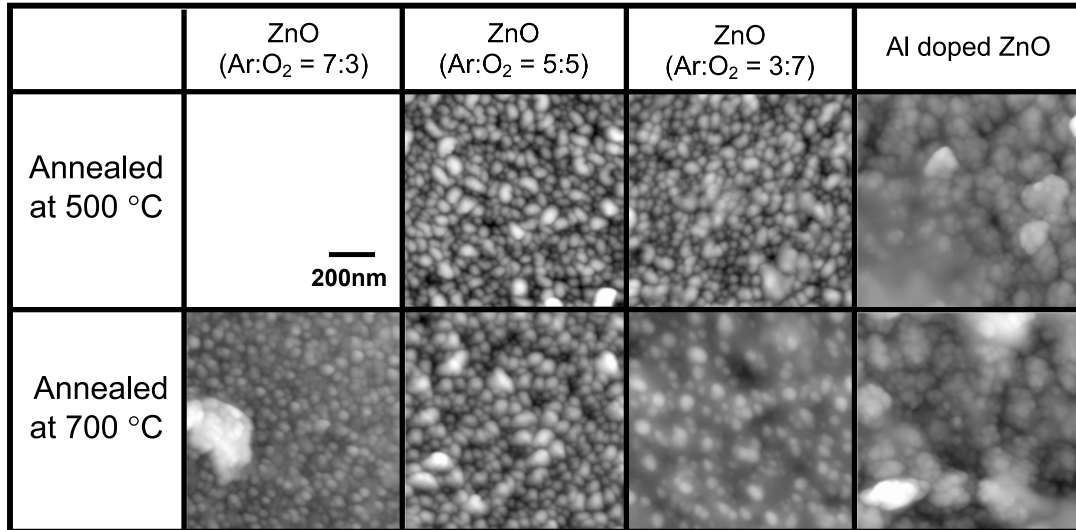

(a) 2 dimensional view (1 μm x 1 μm) of ZnO films

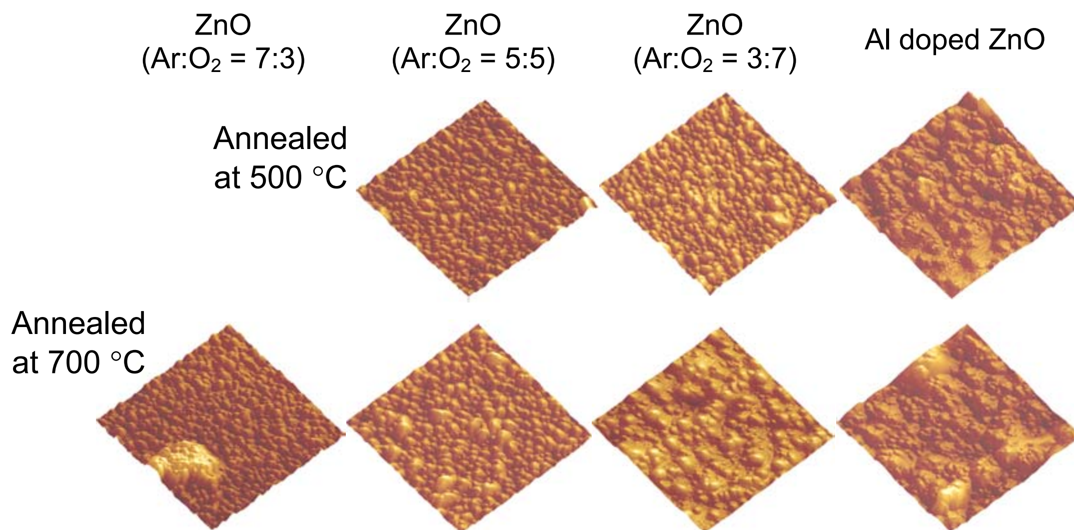

(b) 3 dimensional view (1 μm x 1 μm) of ZnO films

Figure 4.7 AFM images of ZnO films on Si based micro array after annealing at 500 and 700 °C for 12 hours (a) 2 dimensional view (1 μm x 1 μm) and (b) 3 dimensional view (1 μm x 1 μm)

The increase of grain size with increasing oxygen content in the sputtering chamber could be related to the lower deposition rate of these ZnO films. The lower deposition rate provides more time for sputtered Zn and O atoms to diffuse on the surface, resulting in enhanced grain growth. The roughness (Ra) of the ZnO films is summarized in Table 4.4.

Table 4.4 Average roughness (Ra, nm) of ZnO films on micro arrays by AFM

	ZnO ($Ar:O_2$=7:3)	ZnO ($Ar:O_2$=5:5)	ZnO ($Ar:O_2$=3:7)	Al doped ZnO
Annealed at 500 °C	-	4.61	4.34	6.83
Annealed at 700 °C	5.08	4.11	3.75	8.35

As for the XRD patterns, Al doped ZnO films show very distinct AFM images compared to those of the undoped films. Al doped ZnO films have very rough surfaces with agglomerate shaped grains. Even the roughness of surface increases after annealing at 700 °C while the roughness of undoped films decreases. The microstructure remains stable after 700 °C annealing without exhibiting any noticeable grain growth.

The surface of Al doped ZnO films was observed using SEM to investigate the detailed microstructure of the surface. Figure 4.8 show the planar and tilted (52°) view of the surface of the Al doped ZnO film annealed at 700 °C. The SEM image confirms that the film has very rough and porous surface as indicated from AFM images.

For investigating the three dimensional microstructure of Al doped ZnO films, focused ion beam (FIB)-SEM observation was performed. Al doped ZnO films on SiO_2 coated Si wafer annealed at 700 °C were etched by a gallium ion beam to reveal the cross section. Figure 4.9 shows SEM images of the cross sections of Al doped ZnO films. The grain of the film is hardly observed since the cross section, etched by Ga ions, is very smooth. However, the cross sectional view shows that the film has a porous microstructure with fine pores located mainly in the interface region between the film and substrate.

Al doped ZnO films have a rough surface and porous crystalline structure with mixed orientation compared to undoped ZnO films. This appears to be related to the presence of Al dopants in the ZnO films. This will be discussed later.

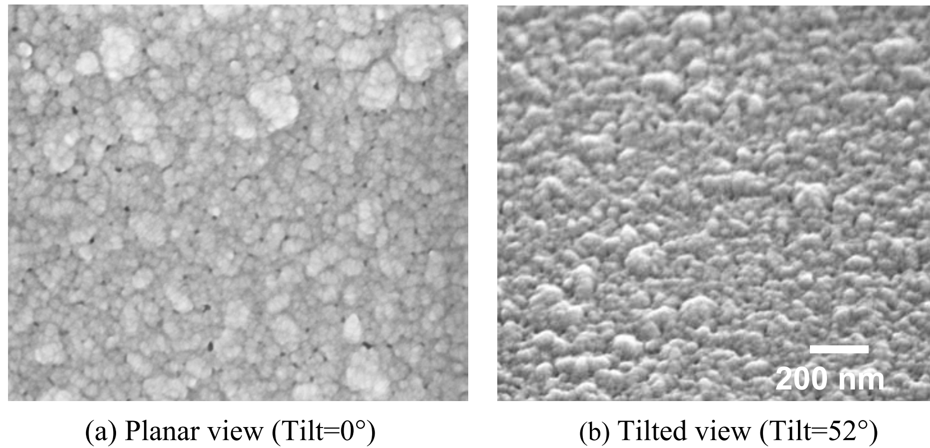

(a) Planar view (Tilt=0°) (b) Tilted view (Tilt=52°)

Figure 4.8 SEM images of Al doped ZnO films after annealed at 700 °C for 12 hours (a) Planar view (Tilt=0°) and (b) Tilted view (Tilt=52°)

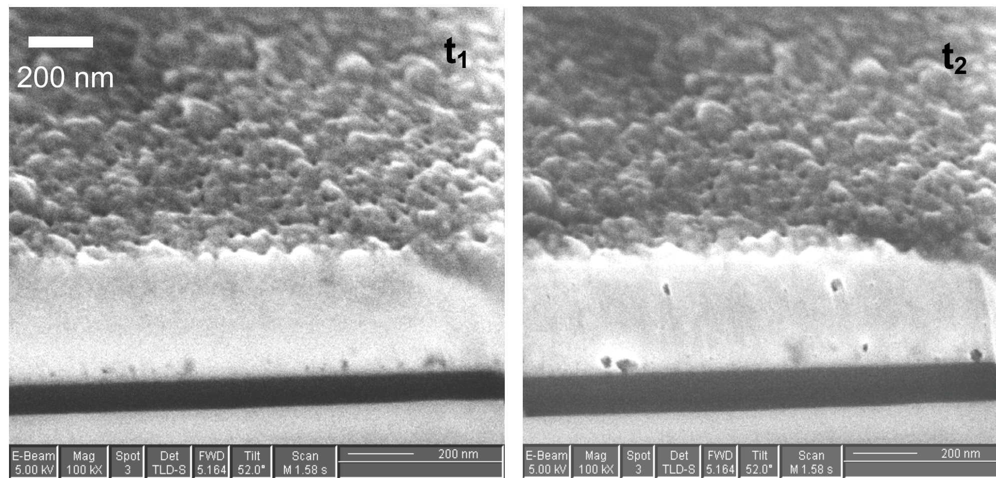

Figure 4.9 SEM images of Al doped ZnO films on SiO_2 coated Si wafer after 700 °C annealed for 12 hrs. Each images shows the cross sectional view after etched continuously by Ga ion beam (t_1 and t_2).

Next, the chemical analysis of sputtered ZnO films was performed. The atomic ratio of Zn, O and Al in ZnO films was examined by wavelength dispersive X-ray spectrometry (WDS, resolution ~ 2%) as shown in Table 4.5 and Figure 4.10. As

expected, undoped ZnO films have higher oxygen contents as one increases the oxygen concentration in the gas phase during sputtering. Which the target material was prepared with 2 wt.% Al, the Al doped ZnO films were found by WDS to contain only about 0.9 wt.% and lower Zn contents compared to the pure ZnO film. This will be explained in the discussion section with the assistance of defect chemistry. All ZnO films show the tendency to approach the stoichiometric ratio (Zn:O=1:1) after annealing of 700 °C.

Table 4.5 Atomic ratios of Zn, O and Al in ZnO films by WDS observation

	ZnO ($Ar:O_2$=7:3)	ZnO ($Ar:O_2$=5:5)	ZnO ($Ar:O_2$=3:7)	Al doped ZnO
Annealed at 500 °C	-	49.0 : 51.0	47.6 : 52.4	45.5 : 53.3 : 1.2(Al)
Annealed at 700 °C	57.8 : 42.2	49.8 : 50.2	48.3 : 51.7	46.0 : 52.7 : 1.3(Al)

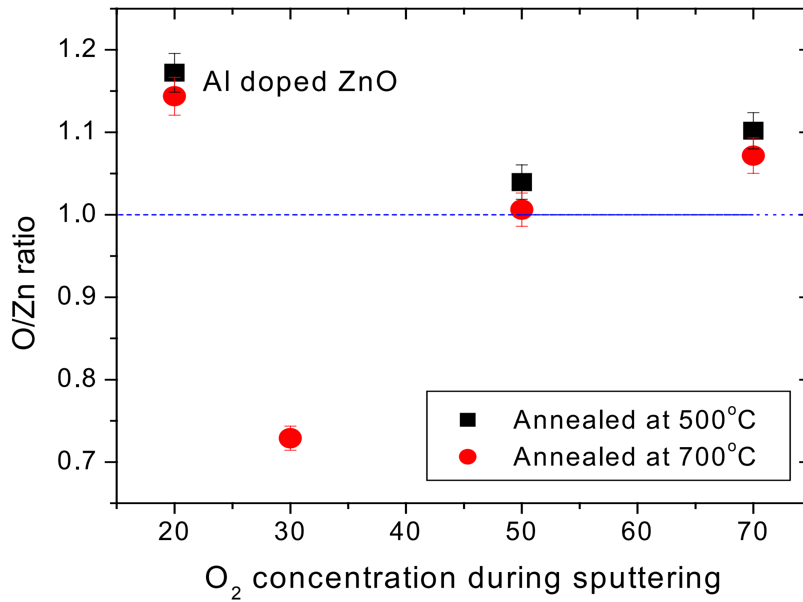

Figure 4.10 O/Zn ratios of ZnO films onto micro arrays measured by WDS.

Summary of key observations

1. The O_2/Ar ratio during sputtering mainly controls the film deposition rate.
2. Higher O_2/Ar ratios give preferential c-axis orientation, larger grain size, better crystalline quality, and near stoichiometric composition.
3. Post deposition annealing results in better crystalline quality and reduces the stress in films
4. Al doping induces porous microstructure with mixed orientation.

4.2. Gas sensor performance

4.2.1. Sensor response

The gas sensor performance of sputtered ZnO films on micro arrays was examined in controlled atmosphere at different temperatures using DC resistance measurements. For example, Figure 4.11 shows the resistance change of ZnO thin film micro array sensors when exposed to H_2 (100 ppm), CO (50 ppm), NO_2 (2 ppm) and NH_3 (50 ppm) in synthetic air (50% R.H., 25 °C) at 420 °C. Both the undoped ZnO and Al doped ZnO films show measurable response to the various gas environments and typical n-type semiconducting behavior; the resistance decreases when exposed to reducing gases (H_2, CO and NH_3), and increases when exposed to oxidizing gas (NO_2).

The post deposition annealing effect on gas sensor performance can be easily observed in Figure 4.11. In all cases, the sensor response is improved following the 700 °C anneal. However, the gas sensor performance of the undoped ZnO films is more sensitive to post annealing treatment than the Al doped ZnO films. Undoped ZnO films annealed at 700°C in air for 12 hours show reasonable gas response with low and stable baseline resistance while undoped ZnO films annealed at 500 °C show poor gas response with unstable baseline resistance. Al doped ZnO films annealed at 500 °C and 700 °C show measurable gas response even though Al doped ZnO films annealed at 500 °C have considerably lower resistance values.

For investigating the influence of the Ar/O_2 ratio during sputtering on sensor performance, the two the undoped ZnO films (Ar:O_2 = 7:3 and 3:7) with the most extreme Ar:O_2 ratios were examined. The gas response of the two ZnO films to H_2 (10, 20, 50 and 100 ppm), NO_2 (1, 2 and 5 ppm) and CO (10, 20, 50 and 100 ppm) was examined at temperatures of 300, 340, 380, 420 and 460 °C and are illustrated in Figure 4.12. The sensitivity to H_2 (100 ppm), NO_2 (5 ppm) and CO (100 ppm) as a function of operation temperature is shown in Figure 4.13. The response to NO_2 of both ZnO films is much greater than to H_2 and CO gases. Both ZnO films show strong response to low concentrations of NO_2 (1 ppm), with increased sensitivity at lower temperature. In general, ZnO films (Ar:O_2 = 3:7) show the better sensitivity and weaker temperature sensitivity as compared to ZnO (Ar:O_2 = 7:3). Note that the sensitivity of ZnO (Ar:O_2 = 7:3) to the various gases nearly disappears at the temperatures of 380 and 420 °C.

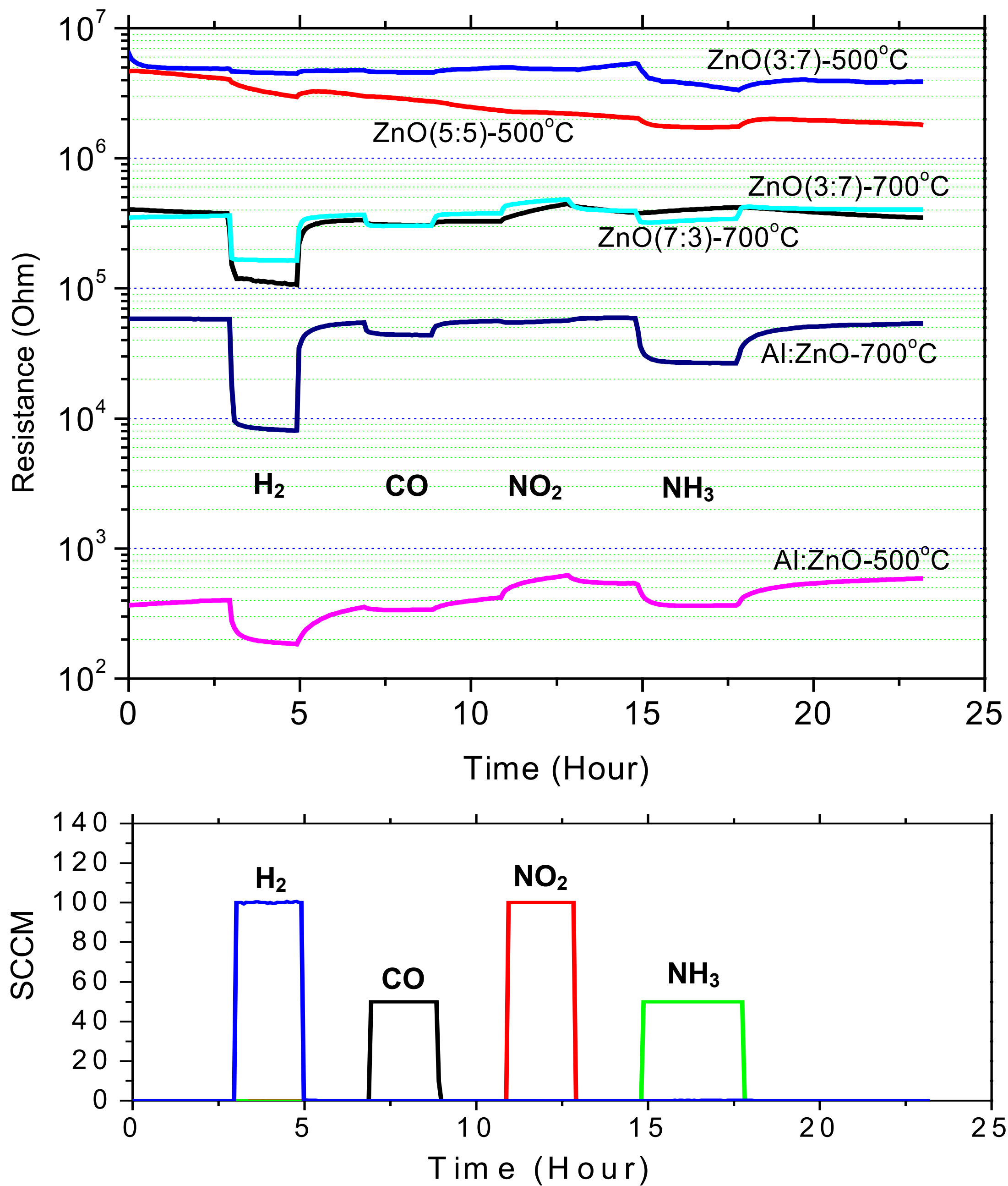

Figure 4.11 Gas responses of sputtered ZnO micro array sensors to H_2 (100 ppm), CO (50 ppm), NO_2 (2 ppm) and NH_3 (50 ppm) in air (50% R.H., 25 °C) at 420 °C

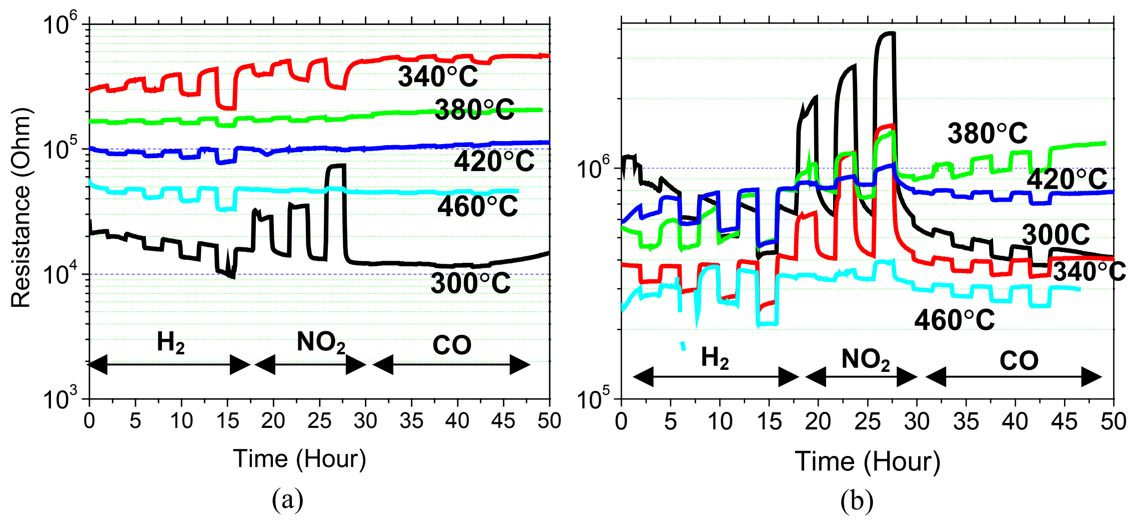

Figure 4.12 Gas responses of sputtered ZnO micro array sensors to H_2 (10, 20, 50 and 100 ppm), NO_2 (1, 2 and 5 ppm) and CO (10, 20, 50 and 100 ppm) (a) Ar:O_2 = 7:3 and (b) Ar:O_2 = 3:7

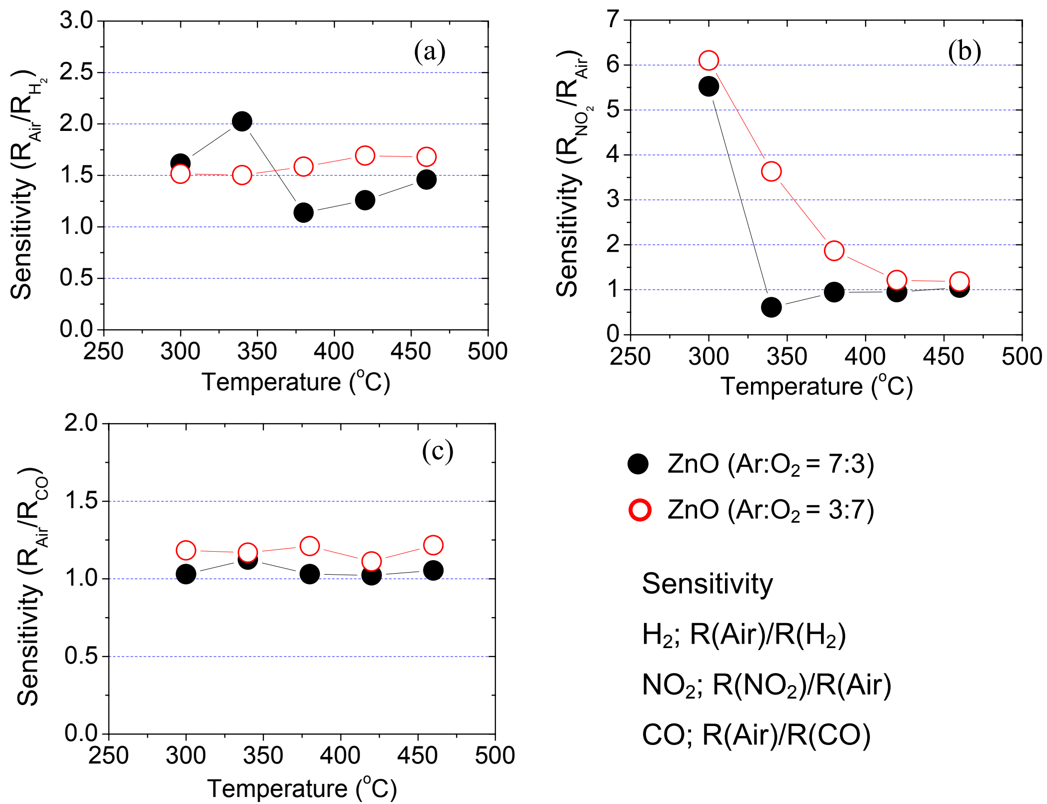

Figure 4.13 Temperature dependent sensitivity of ZnO micro arrays to (a) 100 ppm H_2, (b) 5 ppm NO_2, and (c) 100ppm CO

In order to understand the temperature dependence of the sensitivity to the different gases, it is useful to examine the temperature dependence of the resistance of the ZnO films in the reference air atmosphere. These results, as shown in Figure 4.14, exhibit a number of regimes previously noted in the literature [1]. These include a semiconductor-like behavior from 100 - 200 °C, followed by a temperature insensitive regime (about 200 - 300 °C), then a regime exhibiting a positive temperature coefficient of resistance (PTCR) about 350 - 400 °C, and finally the beginnings of a typical negative temperature coefficient of resistance (NTCR) regime. This unusual behavior, in the temperature insensitive regime, is normally ascribed to transport controlled by an adsorbed layer (OH^-) on the ZnO surface. The PTCR regime, on the other hand, is characterized by thermal desorption of the (OH^-) layer [1, 29]. The adsorbed layer is assumed to be fully removed from the surface of the films at approximately 400 °C.

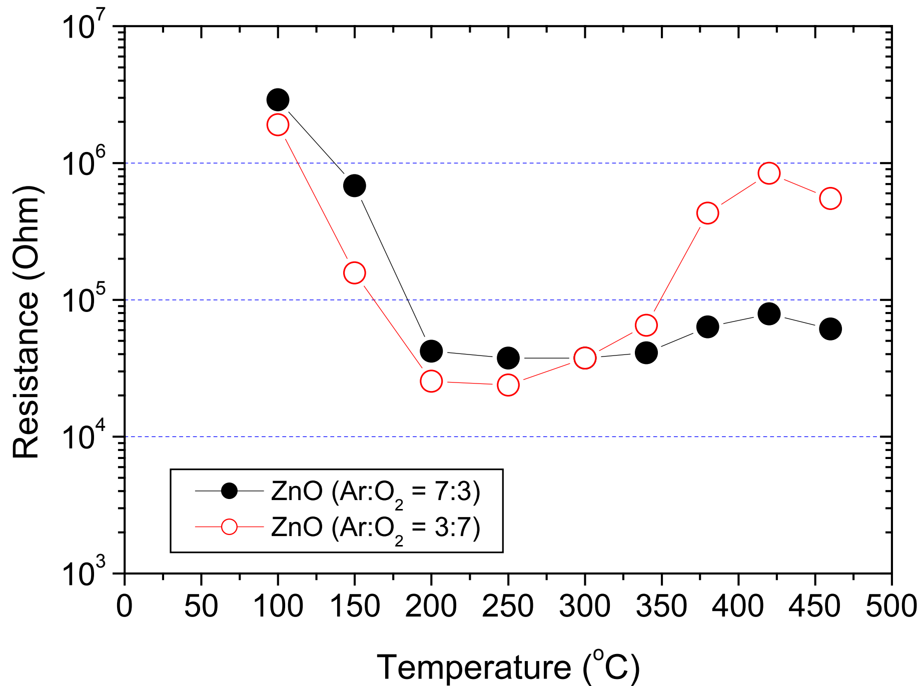

Figure 4.14 Resistance of undoped ZnO films during heating in air

The sensor response of ZnO films with Ar:O_2 = 5:5 was compared to the ZnO film with Ar:O_2 = 3:7 as shown in Figure 4.15. The two ZnO films annealed at 700 °C show similar resistance values and gas sensor response to CH_4 (130 and 1000 ppm), NO_2 (2 and 5 ppm), CO (10, 50, and 100 ppm) and NH_3 (20, 100, and 200 ppm) in synthetic air at 460 °C. These two ZnO films, which have similar physical and chemical properties, also show similar gas sensor performance.

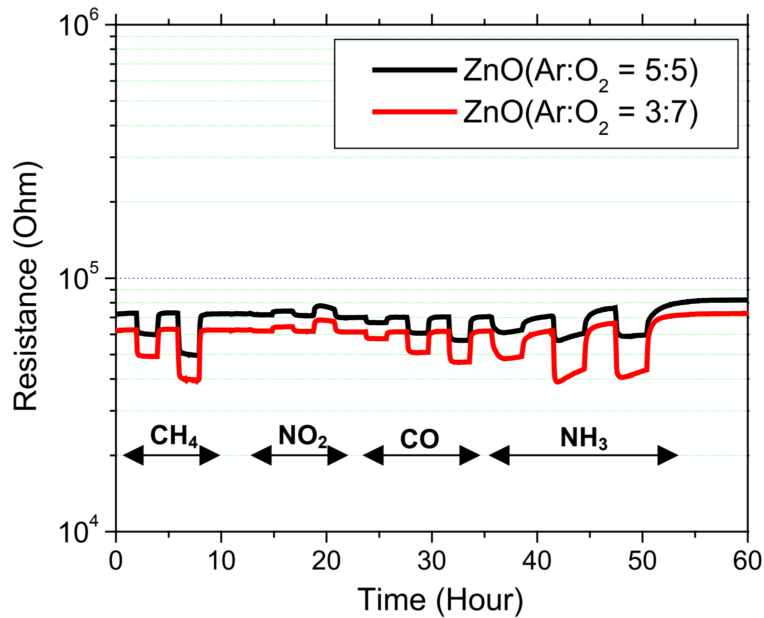

Figure 4.15 Gas responses of ZnO films with Ar:O_2 = 5:5 and 3:7 to CH_4 (130, 1000 ppm), NO_2 (2, 5ppm), CO (10, 50, 100 ppm) and NH_3 (20, 100, 200 ppm) in synthetic (50% R.H., 25 °C) at 460 °C. ZnO films were annealed at 700 °C for 12 hours.

The sensor performance of Al doped ZnO films was examined and compared to that of undoped ZnO films. Figure 4.16 shows the gas response of micro array sensors to H_2 (100 ppm), CO (50 ppm), NO_2 (2 ppm) and NH_3 (50 ppm) in synthetic air at 420 °C. While Al doped ZnO films have lower resistance values, they exhibit superior sensor response to the undoped films.

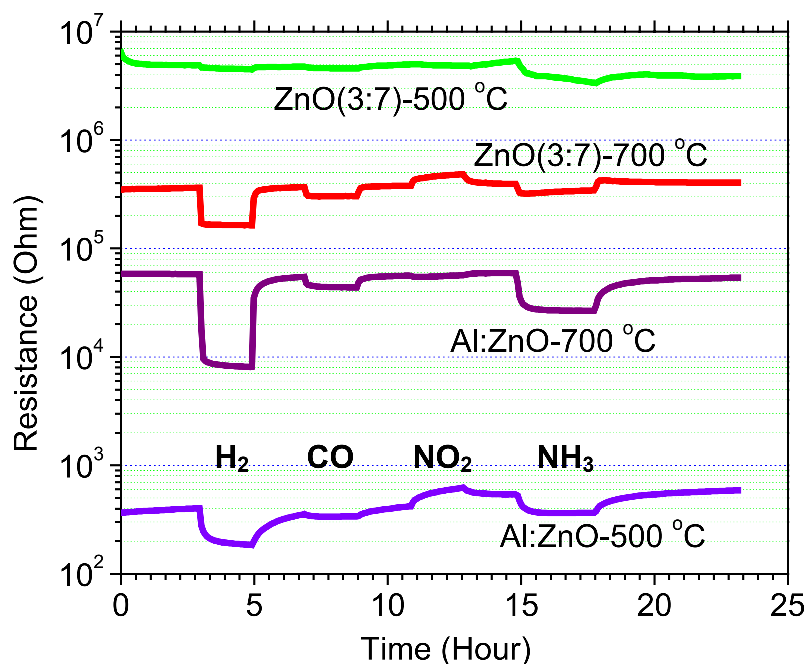

Figure 4.16 Gas response of undoped ZnO and Al doped ZnO micro array sensors to H_2 (100 ppm), CO (50 ppm), NO_2 (2 ppm) and NH_3 (50 ppm) in synthetic air at 420 °C.

The gas sensor performance of the undoped ZnO (Ar:O_2 = 3:7) film was compared to the Fraunhoher-IPM's multi oxide micro array sensor, which contained CTO ($Cr_{2-X}Ti_XO_{3+X}$, Cr doped Ti oxide), Pt catalyst modified SnO_2, WO_3, and V_2O_5 films. The response of the ZnO and the multioxide micro array was measured simultaneously during exposure to H_2 (100 ppm), CO (50 ppm), NO_2 (1 ppm) and NH_3 (50 ppm) in synthetic air at 420 °C. The response of the ZnO film is comparable to the other gas sensitive films as shown in Figure 4.17. Of particular note, only ZnO exhibits a measurable response to NO_2 while only V_2O_5 exhibits sensitivity to NH_3 alone. The other emphasis is that the micro array sensors including SnO_2 show the slow resistance drift, e.g., a SnO_2 micro array shows the slow response following immediate fast response with the exposure to 100 ppm H_2. This slow response have been widely investigated and characterized in later.

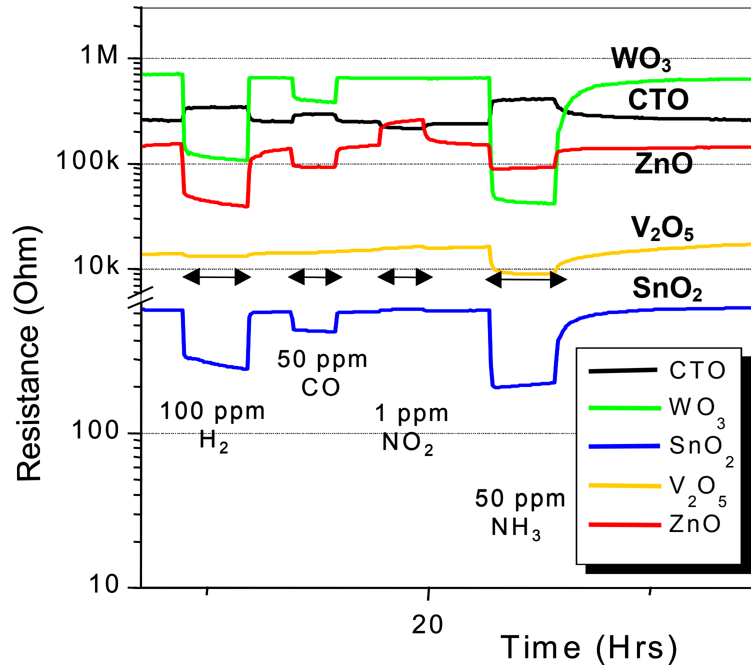

Figure 4.17 Sensor responses of different gas sensitive films onto micro arrays during exposure to H_2 (100 ppm), CO (50 ppm), NO_2 (1 ppm) and NH_3 (50 ppm) in synthetic air with 50% relative humidity, respectively. The operating temperature was 420 °C

Summary of key observations

1. ZnO shows n-type semiconducting behavior.
2. ZnO with higher O_2/Ar ratios has higher sensitivity.
3. ZnO with higher annealing temperature shows higher sensitivity and stable baseline resistance.
4. Al doped ZnO has higher sensitivity in spite of low baseline resistance.
5. ZnO shows a unique response to NO_2 compared to SnO_2, V_2O_5, WO_3 and CTO.

4.2.2. Current – voltage characteristics

The I-V characteristics of ZnO micro array sensors were examined at typical sensor operating temperatures in various gas atmospheres. Hysteretic I-V curves obtained for ZnO films were observed at all operating temperatures (from 300 °C to 460 °C) and in both reducing and oxidizing gas environments. As an example, Figure 4.18 and Figure 4.19 show the I-V curves of ZnO films ($Ar:O_2 = 7:3$) in different gas atmospheres at 300 °C and 460 °C.

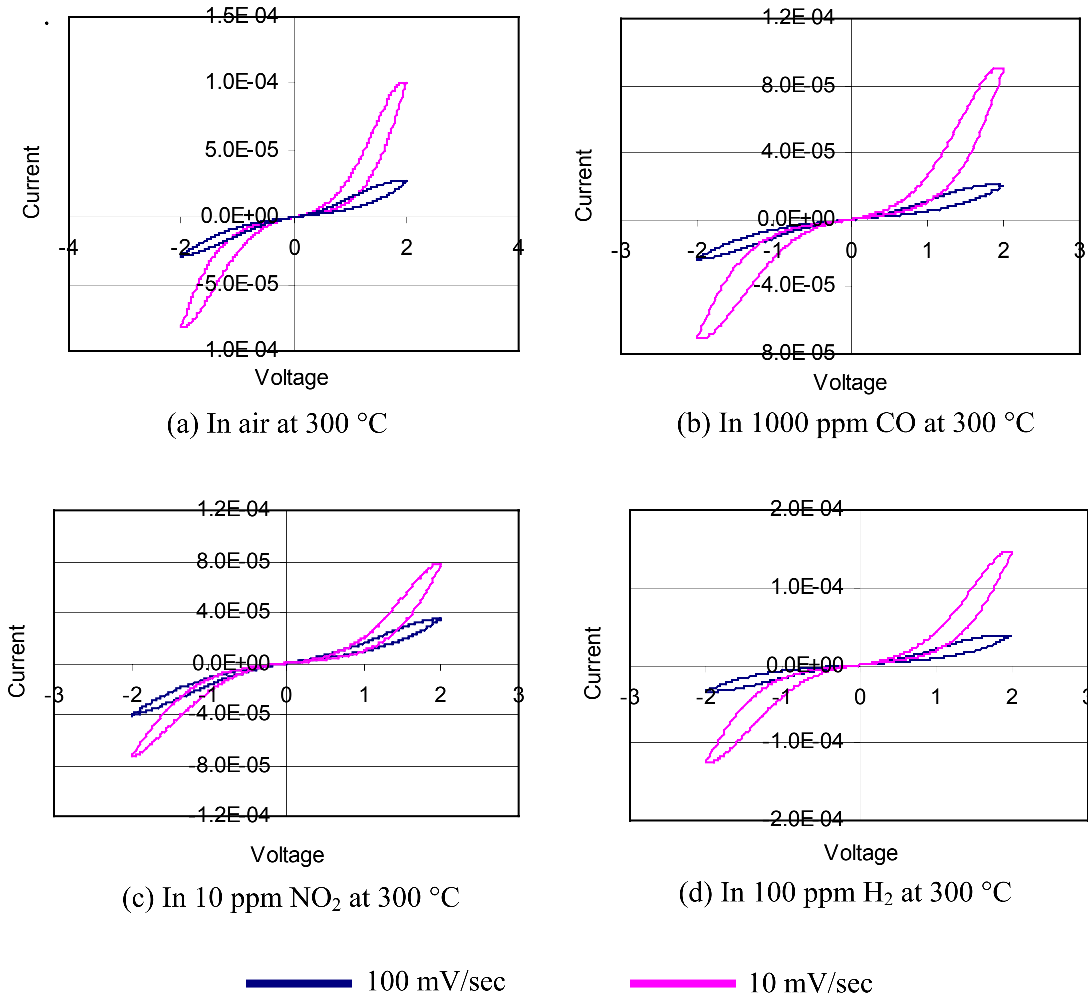

(a) In air at 300 °C

(b) In 1000 ppm CO at 300 °C

(c) In 10 ppm NO_2 at 300 °C

(d) In 100 ppm H_2 at 300 °C

Figure 4.18 Current-voltage (I-V) curves of ZnO ($Ar:O_2$ = 7:3) micro array sensor measured at 300°C. I-V characteristics were observed from 0V to –2V, 0V, 2V to 0V with different sweep rates of 100 mV/sec and 10 mV/sec.

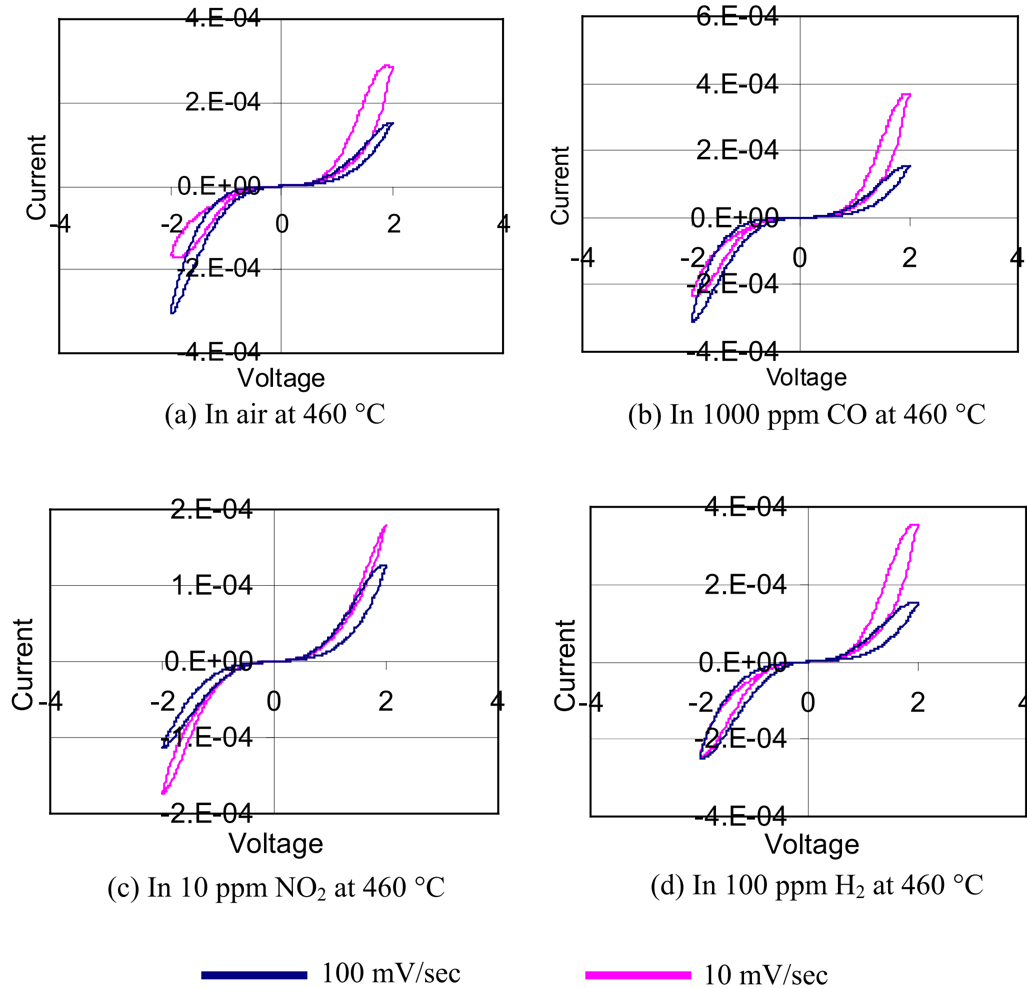

Figure 4.19 Current-voltage (I-V) curves of ZnO (Ar:O_2 = 7:3) micro array sensors measured at 460°C. I-V characteristics were observed from 0V to –2V, 0V to 2V with different sweep rates of 100 mV/sec and 10 mV/sec.

The effect of sweep rate (100 mV/sec and 10 mV/sec) is strongest at 300°C with the effective resistance smaller at the lower sweep rate in both reducing and oxidizing atmosphere. As temperature increased, the discrepancy in the two I-V curves decreased. As shown in Figure 4.19, the difference of I-V curves at 460°C is smaller compared to the I-V curves at 300 °C. However, some hysteresis remains at all operating temperatures (300, 340, 380, 420 and 460 °C) in both reducing and oxidizing atmospheres.

Figure 4.20 shows the I-V curves of Al doped ZnO films (previously annealed at 700 °C) at 420 °C in air. Al doped ZnO films exhibit significantly lower hysteresis and sweep rate dependency and nearly ohmic-like I-V characteristics.

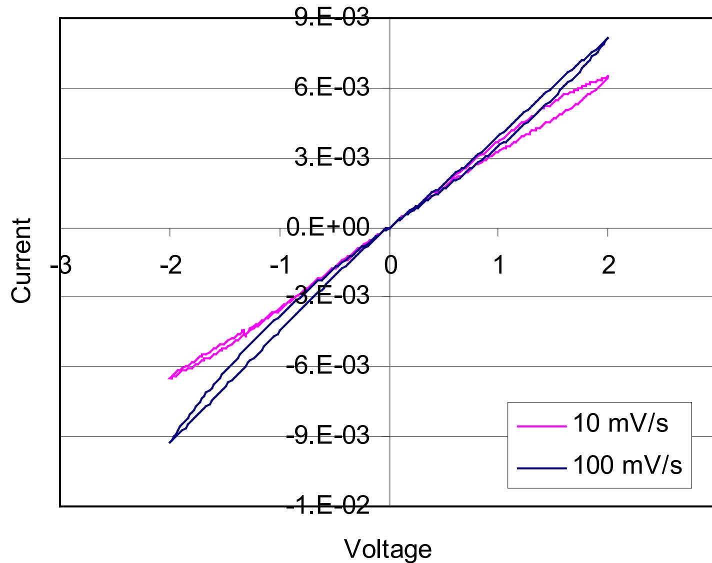

Figure 4.20 Current-voltage (I-V) curves of Al doped ZnO micro arrays measured at 420°C. I-V characteristics were observed from 0V to –2V, 0V to 2V with different sweep rates of 100 mV/sec and 10 mV/sec.

The I-V characteristics of the multi oxide micro arrays (SnO_2, WO_3, CTO and V_2O_5) were also examined. Hysteretic behavior was also found for the n-type semiconducting oxides, i.e., SnO_2, WO_3, and V_2O_5. The I-V characteristics of 70 nm thick SnO_2 films were observed at 400°C in air and are shown in Figure 4.21 (a). The I-V characteristics again show larger hysteretic effects at the lower sweep rate. The I-V characteristics of the p-type semiconductor material, CTO (Cr doped TiO_2), on the other hand, are quite different. Figure 4.21 (b) shows the I-V curves measured for CTO films at 420 °C in air at several sweep rates (100 mV/sec and 10 mV/sec). These exhibit nearly ohmic behavior without evident hysteretic behavior.

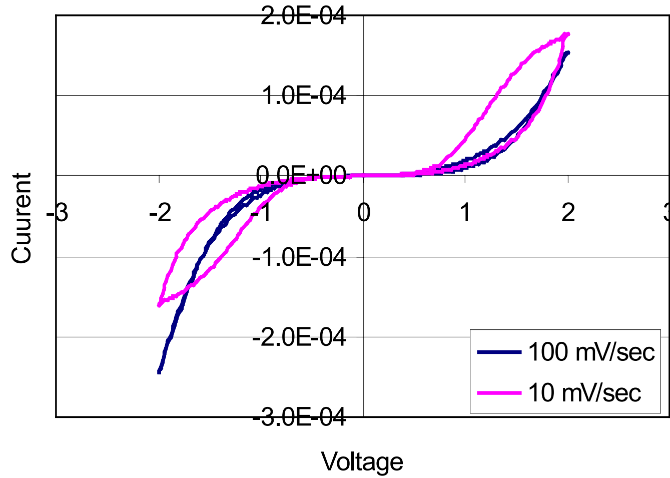

(a) A SnO_2 (70 nm) film onto micromachined platform at 400 °C in air.

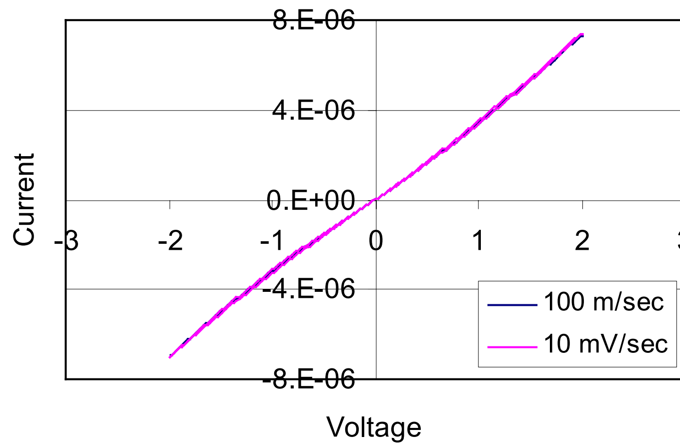

(b) CTO (300 nm) micro array sensor at 420 °C in air

Figure 4.21 Current-voltage (I-V) curves of multi oxide micro arrays. The voltage sweep rates were 100mV/sec and 10 mV/sec, and sweep direction was 0V to –2V, 2V, to 0V.

The influence of different oxygen and argon mixtures on the I-V characteristics was investigated. Figure 4.22 shows the I-V curves of ZnO films ($Ar:O_2$ = 5:5) measured at 420°C in several oxygen/argon mixtures. As shown, the sweep rate dependence and hysteresis of the I-V curves decrease as the oxygen content in argon decreases.

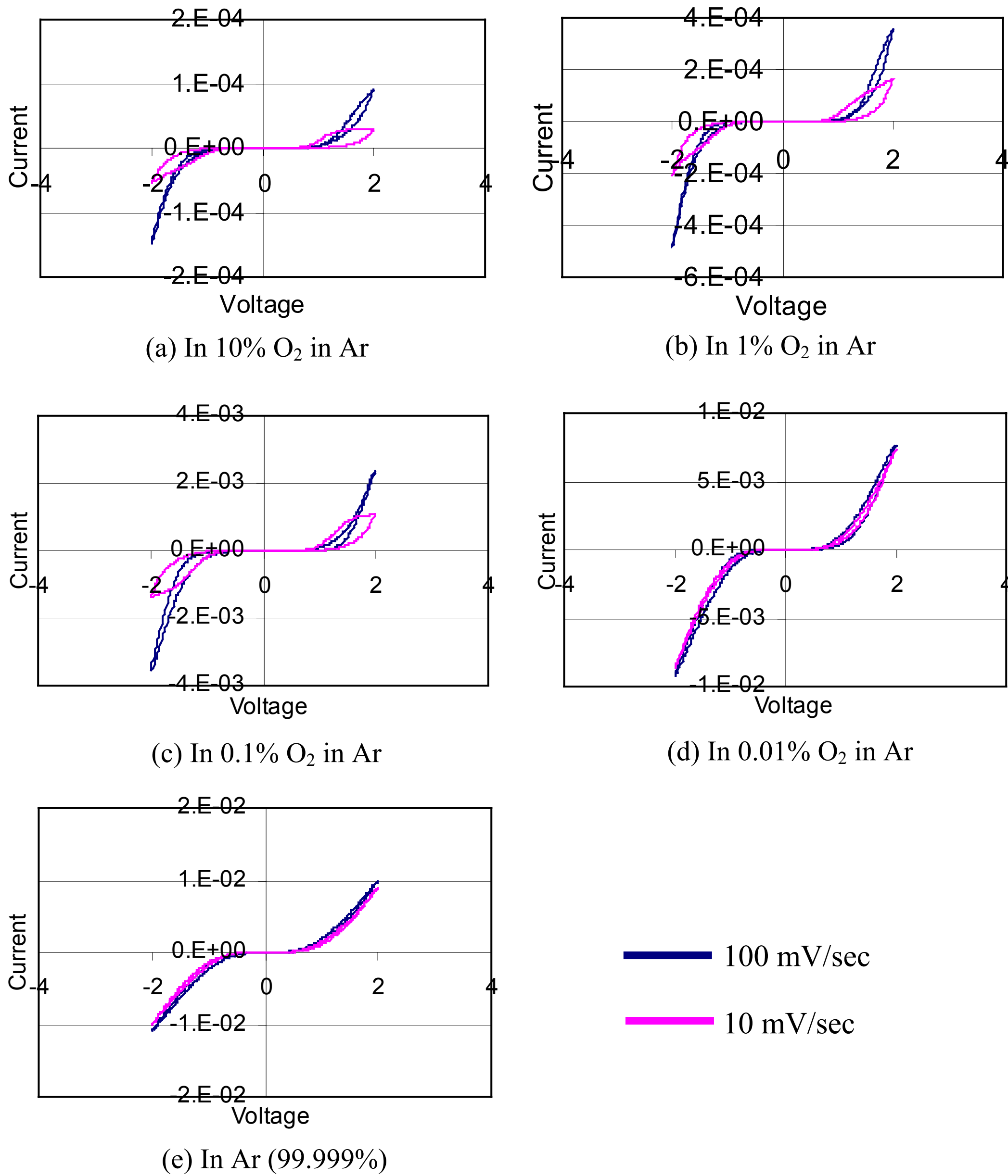

(a) In 10% O_2 in Ar

(b) In 1% O_2 in Ar

(c) In 0.1% O_2 in Ar

(d) In 0.01% O_2 in Ar

(e) In Ar (99.999%)

Figure 4.22 Current-voltage (I-V) curves of ZnO ($Ar:O_2$ = 5:5) micro arrays measured at 460°C in several oxygen contents in argon. I-V characteristics were observed from 0V to –2V, 0V to 2V with different sweep rates of 100 mV/sec and 10 mV/sec.

The gas response of ZnO micro arrays was also examined using I-V measurements. These I-V curves also exhibit hysteresis, sweep rate dependency and measurement history dependency. Thus, the gas sensitivity acquired from the I-V characteristics was not reproducible and varied at each measurement voltage. Figure 4.23 shows an example of sensor response and sensitivity. ZnO ($Ar:O_2$ = 7:3) was exposed to H_2 and CO in air at 460 °C and the sensitivity was calculated using the ratio of resistances (R_{Air}/R_{Gas}). The sensitivity also exhibits hysteresis and varies with voltage.

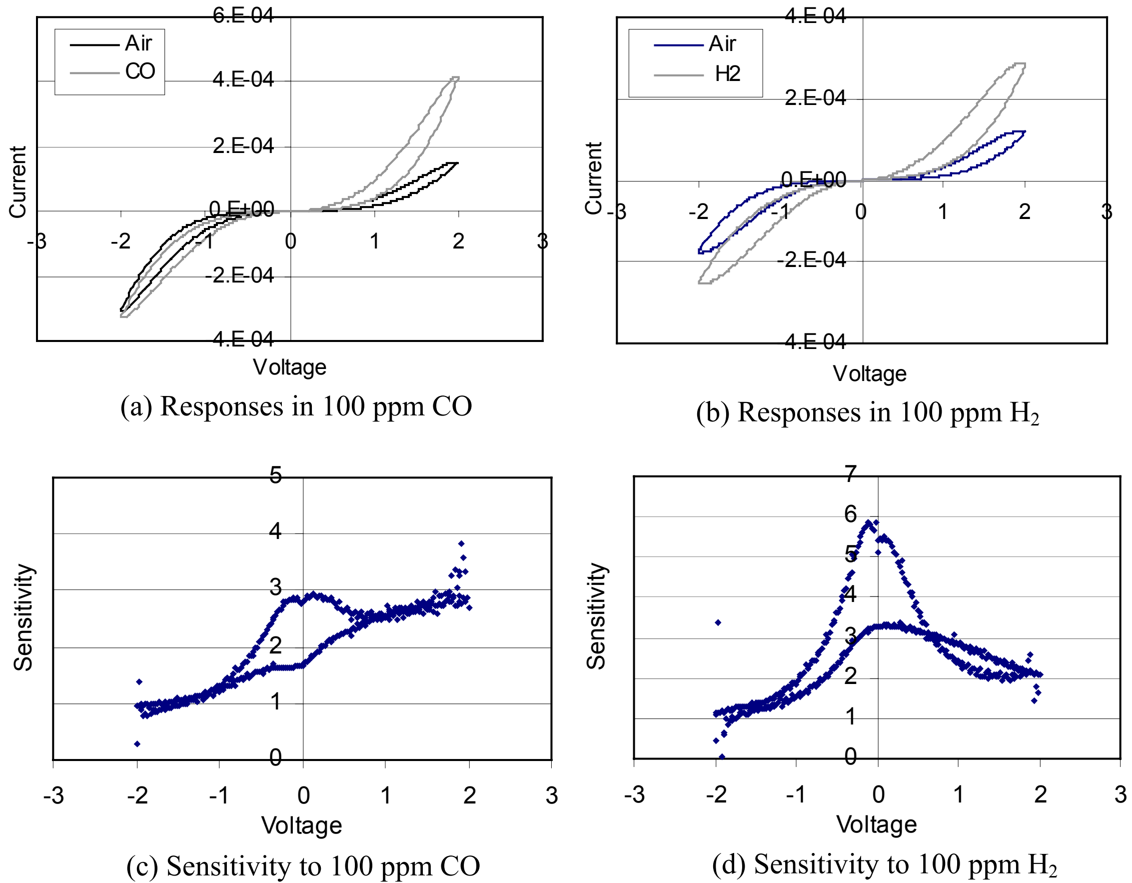

(a) Responses in 100 ppm CO

(b) Responses in 100 ppm H_2

(c) Sensitivity to 100 ppm CO

(d) Sensitivity to 100 ppm H_2

Figure 4.23 Gas responses and sensitivity of ZnO ($Ar:O_2$ = 7:3) micro arrays to 100 ppm CO and H_2 at 460°C using I-V measurements. I-V characteristics were observed from 0V to –2V, 0V to 2V with sweep rates of 100 mV/sec.

Figure 4.24 shows measured I-V curves of a ZnO film ($Ar:O_2$ = 5:5) obtained at room temperature with different sweep rates and voltage polarities. The I-V

characteristics were measured with sweep rates of 100 mV/sec and 10 mV/sec, and sweep directions starting with 0V to –3V, 0V, 3V to 0V or 0V to -3V, 0V, 3V to 0V).

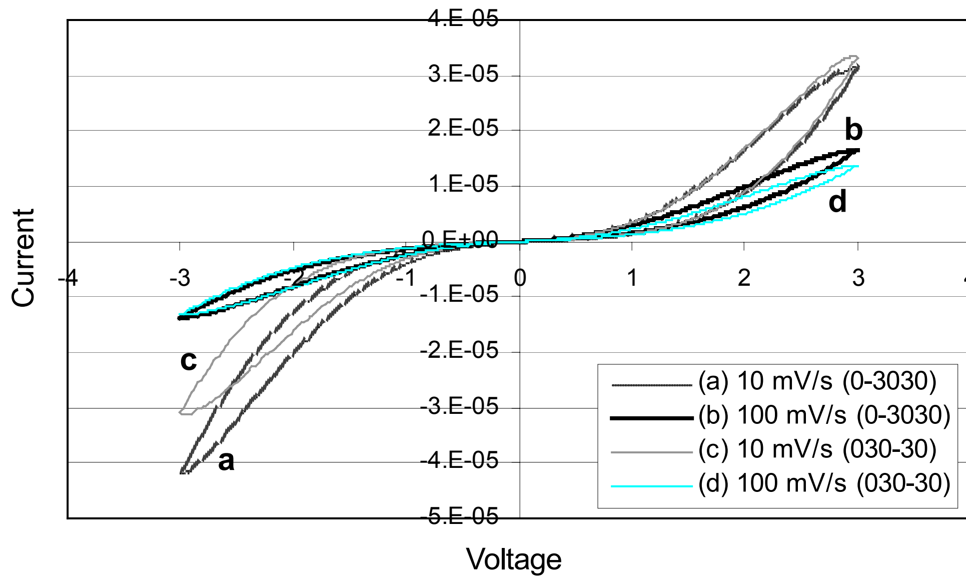

Figure 4.24 Current-voltage (I-V) curves of the ZnO film (Ar:O_2 = 5:5) onto micro array chip measured at room temperature in open atmosphere. I-V characteristics were observed from 0V to –3V, 0V, 3V to 0V, or 0V to 3V, 0V, -3V to 0V with different sweep rates (100 mV/sec and 10 mV/sec)

Several surface treatments were examined as a means of investigating this phenomenon. First, ethyl alcohol was dripped onto the surface of the ZnO films. After the alcohol was dried, I-V measurements were performed with different sweep rates and delay as shown in Figure 4.25. After the alcohol treatment, the resistance of the films increased, and the abnormal I-V characteristics including hysteresis disappeared. The abnormal I-V characteristics were not recovered even after the film had been placed into a vacuum chamber (5 x 10^{-7} Torr) overnight followed by ultrasonic cleaning in D.I. water for 10 min. Finally, the ZnO films were annealed at 500 °C in air for 5 hours. After annealing, the resistance increased slightly and the abnormal I-V characteristics re-appeared. This points to the importance of surface coverage on the electrical properties of these thin films.

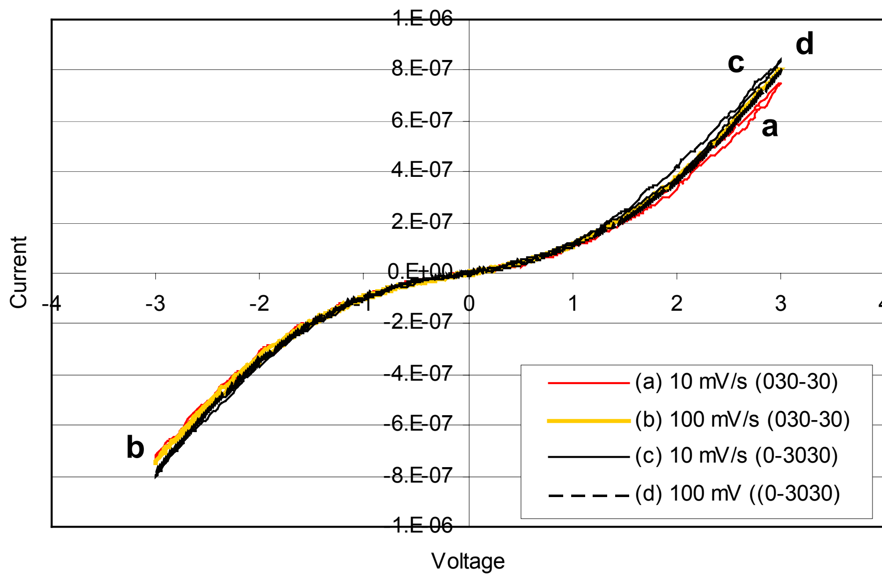

Figure 4.25 Current-voltage (I-V) curves of ZnO film (Ar:O_2 = 5:5) onto micro array chip measured at room temperature in open atmosphere after ethyl alcohol treatment. I-V characteristics were observed from 0V to –3V, 0V, 3V to 0V, or 0V to 3V, 0V, -3V to 0V with different sweep rates (100 mV/sec and 10 mV/sec)

Summary of key observations

1. I-V characteristics of undoped ZnO micro arrays exhibit back-to-back diode characteristics.
2. I-V curves of undoped ZnO show hysteresis and sweep rate dependences in air, 100 ppm H_2, 10 ppm NO_2 and 100 ppm CO.
3. The sweep rate dependence and hysteresis of the I-V of undoped ZnO curves decrease as the oxygen content in argon decreases
4. Al doped ZnO films exhibit significantly lower hysteresis and sweep rate dependences and nearly ohmic-like I-V characteristics
5. SnO_2 shows hysteretic behavior and sweep rate dependences while CTO exhibits nearly ohmic behavior without evident hysteretic behavior.
6. Surface treatments modify the I-V characteristics of ZnO films
7. Gas responses by I-V curves indicate that sensitivity depends on measurement method.

4.2.3 AC impedance response

In an attempt to deconvolute the effects of the gases on the overall resistance of the ZnO films, AC impedance spectroscopy (frequency: 1 - 10^7 Hz and AC amplitude: 50 mV) was observed to examine contributions from bulk and interfacial components of the electrode-film structure. Measurements were focused on undoped ZnO micro arrays since Al doped ZnO films were too conductive for AC impedance investigation. Figure 4.26 shows the AC impedance spectra of a ZnO (Ar:O_2 = 3:7) micro array exposed to dry air at a temperature of 460 °C with DC biases of 0, 1, and 2V. The high frequency semi-circle is independent of bias. A second semi-circular loop with an inductive component appears at lower frequency only under applied DC bias and increases in diameter with increasing DC bias. This behavior was characteristic all of the undoped ZnO films investigated.

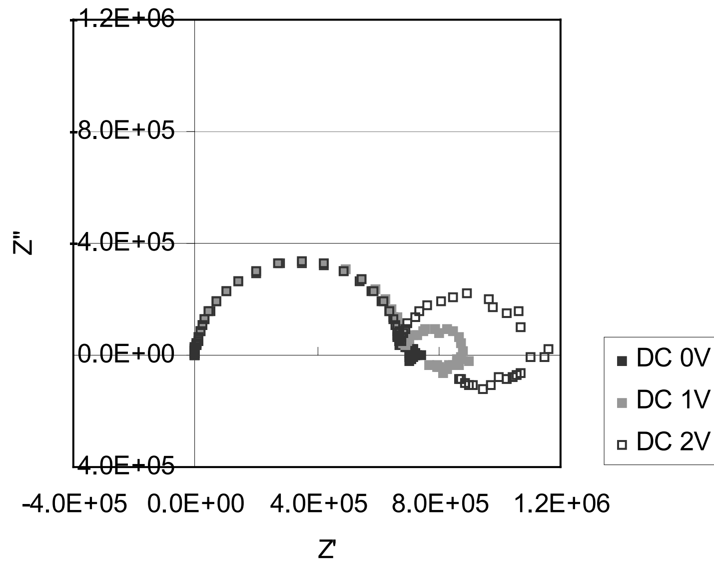

Figure 4.26 The AC impedance spectra of ZnO (Ar:O_2 =3:7) micro arrays in air at 460 °C with applied DC bias 0, 1 and 2V.

The AC impedance spectra indicate that there are two main contributions to the overall impedance. The response at high frequency (above 10^3 Hz) has the capacitive component of several pF. The lower frequency response (below 10^3 Hz) has a larger

capacitive component of about 10^{-8} – 10^{-9} F. As the DC bias increases, the capacitance value of this second semi-circle decreases, while the resistance increases.

During AC impedance measurements, the spectra were, at times, observed to be dependent on measurement history. Consequently, the impedance spectra, following a DC bias pretreatment, were re-examined in air at 460 °C. Figure 4.27 shows the AC impedance spectra of a ZnO film ($Ar:O_2$ = 3:7) with 40 min of DC bias pretreatment. For example, after 1V DC bias for 40 min as the pretreatment, the AC impedance spectra were measured while maintaining the 1V DC bias. With the DC bias pretreatment, both high and low frequency semi-circles increase in diameter as the DC bias increases.

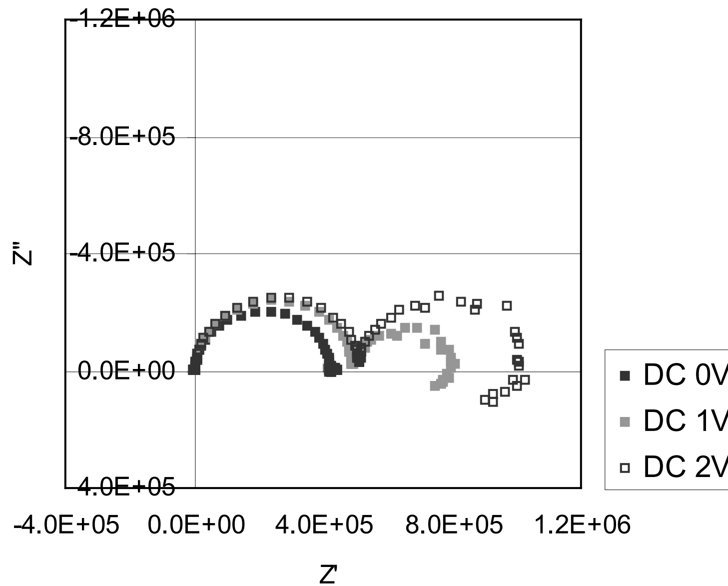

Figure 4.27 The AC impedance spectra of ZnO ($Ar:O_2$ = 3:7) micro arrays in air at 460 °C measured at DC biases, following 40 min of DC biases pretreatment.

To deconvolute the effects of DC bias during pretreatment and measurement, the DC biases were applied only between measurements while the AC impedance spectra were examined without applied DC bias. Figure 4.28 shows the AC impedance spectra of the ZnO micro array sensors after the DC bias pretreatment for 40 min. The spectra is dominated by a large semicircle at high frequency which increases in diameter with

increasing DC bias during pretreatment together with what appears to be a very small semicircle at the low frequency end.

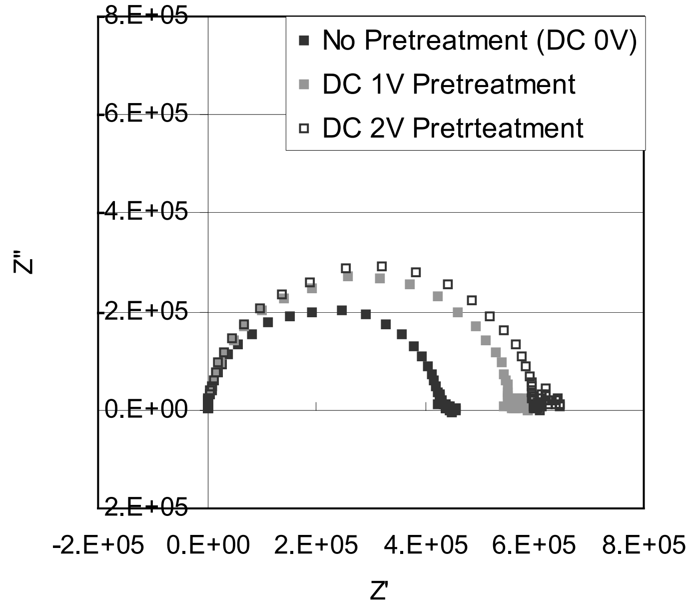

Figure 4.28 AC impedance spectra of ZnO (Ar:O_2 =3:7) micro arrays in air at 460 °C without biases after DC bias pretreatments for 40 min

AC impedance spectra of multi oxide arrays (SnO_2, WO_3, V_2O_5 and CTO) were also examined for comparison purposes. WO_3 and V_2O_5 films were not suitable for AC impedance spectra due to their low resistance values. The DC bias dependent behavior of ZnO was also found for SnO_2 films. The AC spectra of the SnO_2 micro array showed the second semi-circle component at low frequency with DC applied bias. In contrast, the CTO film showed no second semi-circular component at low frequency when DC bias was applied in pretreatments and during measurements. Figure 4.29 shows an example of the AC impedance spectra of SnO_2 and CTO micro arrays exposed to air at 420 °C. The spectra were measured at DC 1V bias following DC 1V bias pretreatment for 40 min.

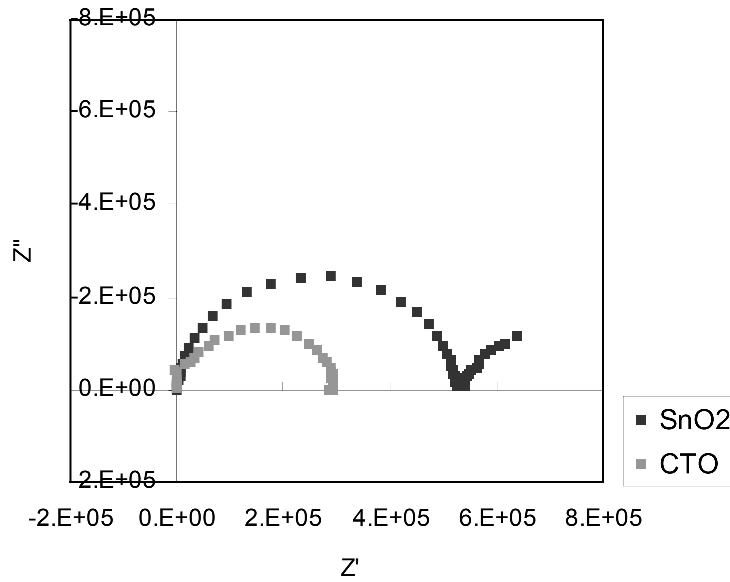

Figure 4.29 AC impedance spectra of SnO_2 and CTO micro arrays in air at 420 °C. The spectra were measured at DC 1V bias following the DC 1V pretreatment for 40 min.

AC impedance spectroscopy of ZnO films was performed in different oxygen and argon mixtures. When ZnO micro arrays were exposed to 10 and 1 % oxygen in argon, the AC spectra measured with DC bias have both semi-circle components at high and low frequencies. In environments with less than 0.1% oxygen in argon, it was difficult to investigate the DC bias effect since the resistance with DC biases was too small for observing the AC impedance spectra.

When the time dependent stability measurements were performed, sometimes, the second semi-circle component at low frequency was observed even without applied bias following repeated measurement. As the number of measurements increased, the low frequency semi-circular component increased slightly. Figure 4.30 shows the AC spectra of a ZnO (Ar:O_2 = 3:7) micro array exposed to different oxygen partial pressures at 420 °C. These spectra were obtained following repeated measurements every 5 min for 17 hours. The overall resistance is seen to reduce with decreasing oxygen with the low frequency component becoming unmeasureable at .01% oxygen and below.

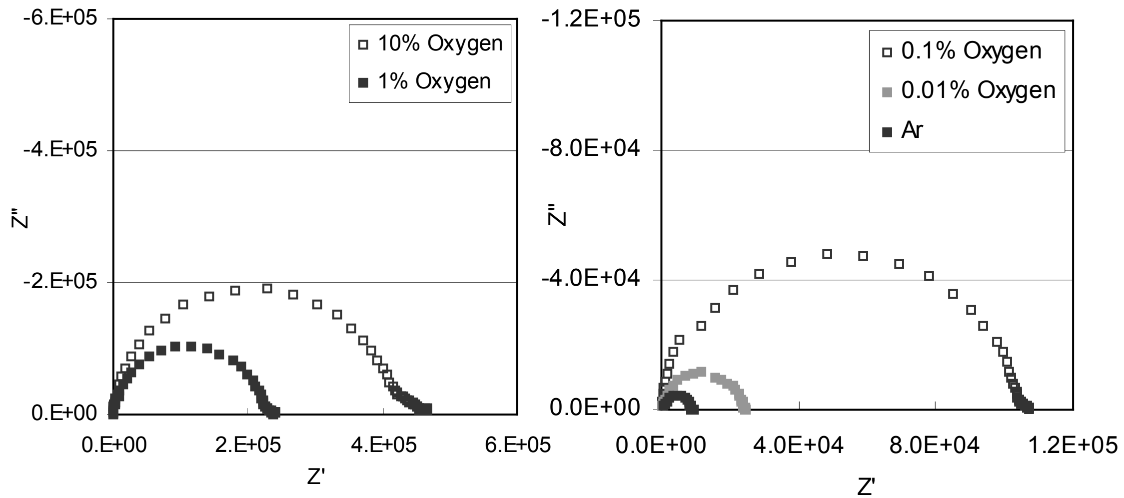

Figure 4.30 AC impedance spectra of ZnO ($Ar:O_2$ = 3:7) micro arrays exposed to the different oxygen contents in argon at 420 °C. The spectra were obtained without DC bias following repeated measurements every 5 min for 17 hours.

AC impedance spectroscopy was also performed when the ZnO micro arrays were exposed to other gas environments. Figure 4.31 shows the AC impedance spectra of a ZnO ($Ar:O_2$ = 7:3) micro array exposed respectively to 100 ppm CO, 10 ppm NO_2 and 100 ppm H_2 in air at a temperature of 420 °C without applied biases (DC 0V) during measurements. Only the high frequency semi-circle appears in these gas environments as well. The diameter of the semi-circle increases when exposed to NO_2 while it decreases in CO and H_2. These changes correspond well to the n-type semiconducting behavior of ZnO films.

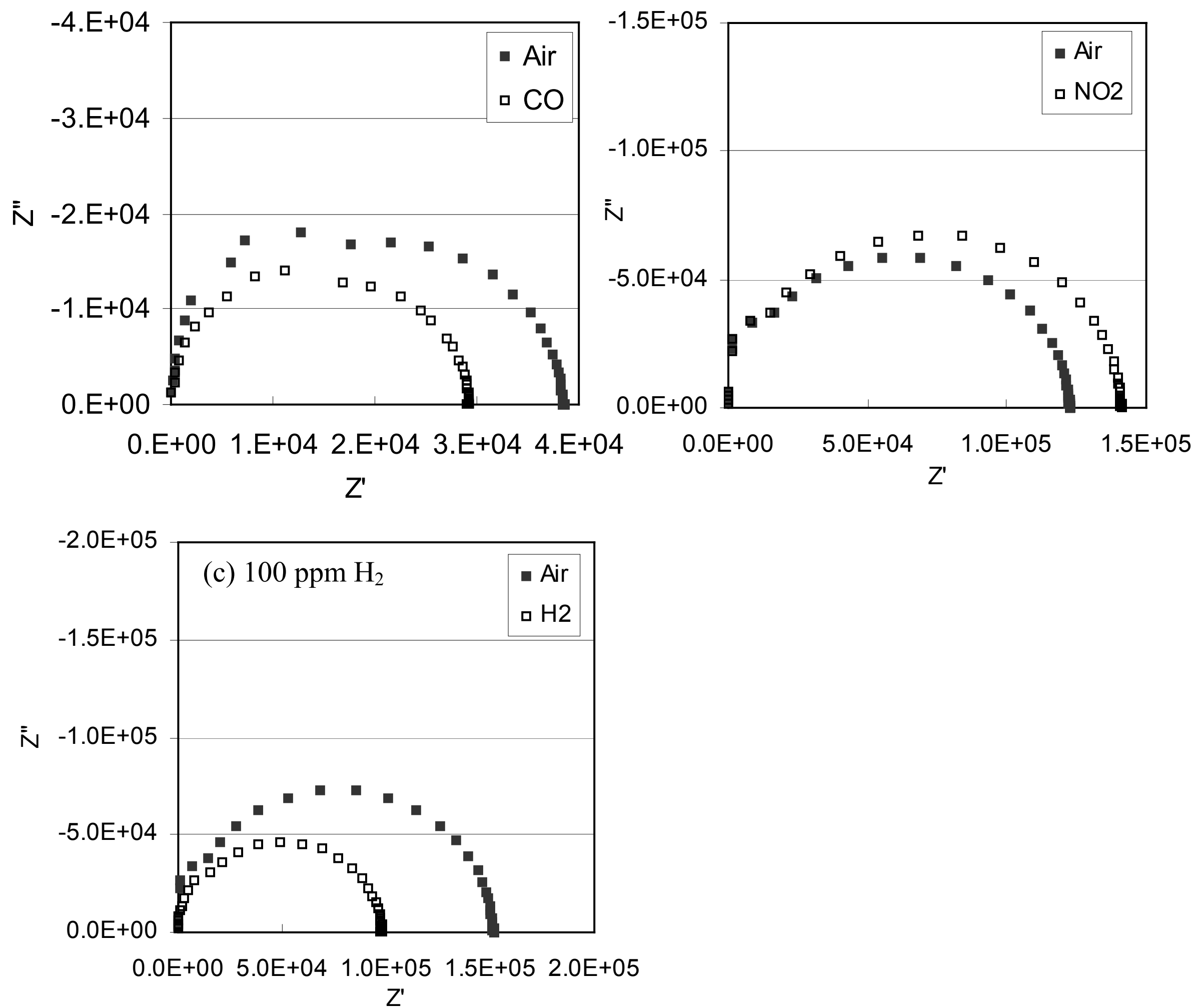

Figure 4.31 AC impedance spectra of ZnO ($Ar:O_2$ = 7:3) micro arrays exposed in air to CO (100 ppm), NO_2 (10 ppm) and H_2 (100 ppm) at 420°C without applied DC biases during measurements

The DC bias effect on sensor response was also investigated in various gas environments. Figure 4.32 shows the AC impedance spectra of a ZnO ($Ar:O_2$ = 3:7) micro array exposed to 100 ppm H_2 in dry air at a temperature of 460 °C with DC biases of 0, 1 and 2V. Even in 100 ppm H_2, a second semi-circle forms at low frequency with applied DC bias. Both semi-circles shrunk when the ZnO film was exposed to H_2. This

DC bias effect on sensor response was also found in the other gas environments (CO and NO_2).

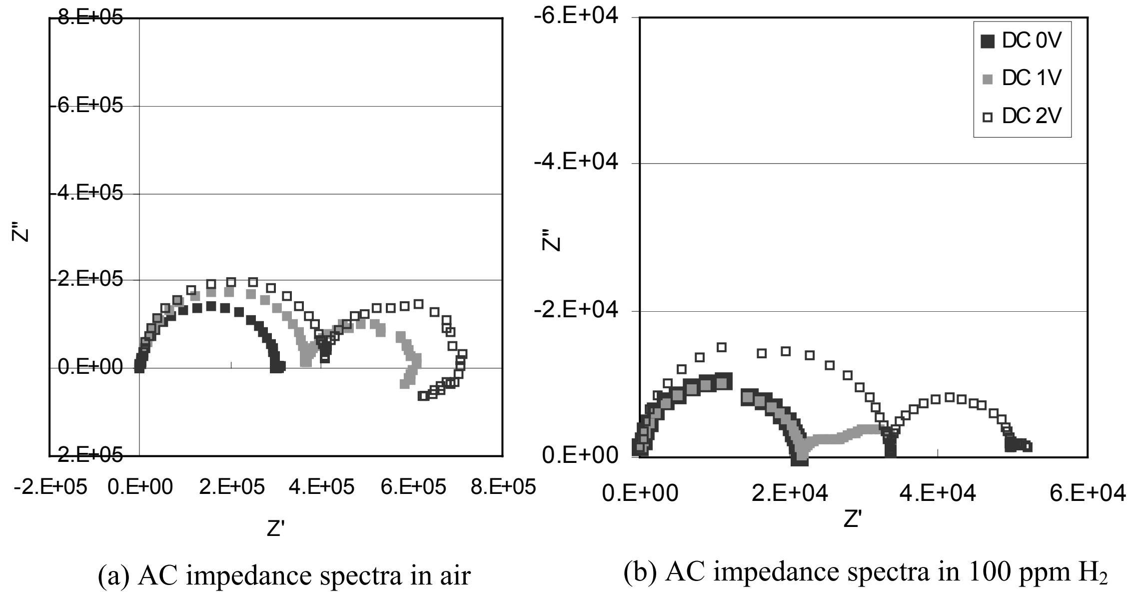

(a) AC impedance spectra in air

(b) AC impedance spectra in 100 ppm H_2

Figure 4.32 Responses of ZnO (Ar:O_2 = 3:7) micro arrays exposed 100 ppm H_2 in air at 460°C with applied DC biases of 0, 1 and 2V

Summary of key observations

1. The AC spectra of ZnO micro arrays have high and low frequency semi-circular components
2. Applied DC bias modifies both semi-circles
3. The AC spectra of SnO_2 micro arrays show two semi-circle components with DC applied bias. In contrast, the CTO film shows no second semi-circular component
4. The low frequency component becomes unmeasureable at 0.01% O_2/Ar mixtures and below.
5. Both semi-circles respond to gas atmosphere.

4.3 Time dependent sensor performance

In utilizing the sensor performance of ZnO micro arrays, the resistance drift was found in the temperature range of sensor operation (300 – 460 ºC). When micro arrays were exposed to different gas environments, a slow resistance drift over several hours followed an almost immediate resistance response. Sometimes, the resistance value in reference air environment steadily changed even after overnight preheating of the ZnO sensors. As described in the previous chapter, the resistance of micro arrays was dependent on DC biases applied during pretreatment and measurements. For investigating these response drifts, the resistance of the micro array sensors was observed on a long time scale (around 20 hours) with or without bias effects.

4.3.1 Time dependent response

For investigating the drift of gas sensor response, the resistance of a ZnO ($Ar:O_2$ = 5:5) micro array was measured in various oxygen partial pressures following exposure to dry air at 420 °C. The resistance was measured every 5 minutes for 17 hours from the AC spectra without DC bias applied either during pretreatment or measurements as shown in Figure 4.33. When ZnO was exposed to oxygen/argon mixtures following dry air, the response is expressed as the ratio of resistance in dry air to that in the oxygen/argon mixture, R (oxygen/argon mixture)/R (dry air), in Figure 4.33 (a), (b) and (c). Figure 4.33 (d) shows the response of ZnO exposed to dry air following exposure to argon. In this case, the response is defined as the ratio of resistance in dry air to that in argon ($R_{Dry\ air}/R_{Argon}$).

The response of ZnO to oxygen/argon mixtures shows n-type semiconductor behavior i.e., resistance decreases with decrease of oxygen content. The sensitivity to reductions in oxygen partial pressure is surprisingly high. For example, the sensitivity of ZnO to argon is more than 100 ($R_{Dry\ air}/R_{Argon}$). However, the response time is unreasonably slow to be attributed to adsorption/desorption of oxygen on the surface alone. The response of ZnO micro arrays can be mainly divided into two regimes, fast and slow responses. For example, first, the resistance of ZnO was responded almost immediately with the exposure to argon following dry air. After the immediate response,

the resistance was steadily decreased and drifted for about 17 hours. The long response time indicates that the other reactions are also involved in the sensor response of ZnO.

The response of ZnO exposed to dry air following argon annealing also shows several regimes and more than a factor of a 100 increase in resistance. However, the response seems to be faster during oxidation than during reduction, i.e. When the ZnO is exposed to air following argon, the resistance is almost stabilized in 4-5 hours versus >17 hours respectively indicating differences in the rates of reactions for reduction and oxidation.

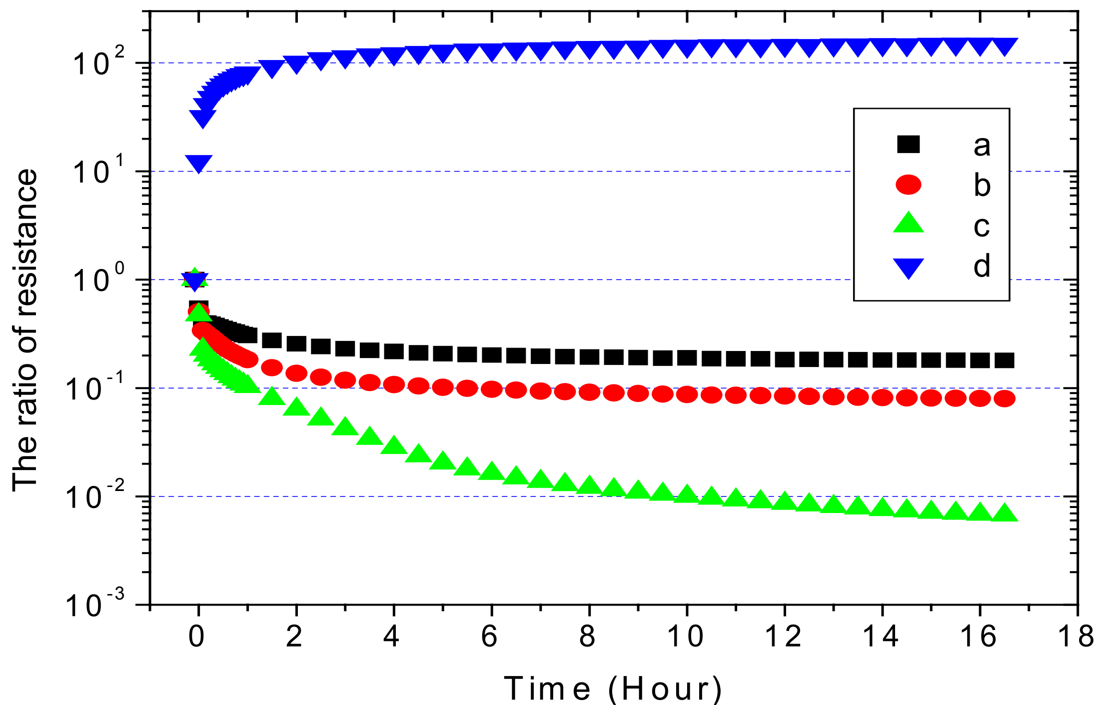

Figure 4.33 Resistance changes of ZnO micro arrays in oxygen/argon mixtures and dry air at the temperature of 420º C. The AC impedance spectra were utilized without biases. The ZnO was exposed to (a) 1% O_2 in Ar, (b) 0.1% O_2 in Ar, and (c) Ar following dry air or (d) dry air following Ar. The response is expressed as the ratio of resistance between oxygen/argon mixtures and dry air.

The resistance dependence of this ZnO (Ar:O_2 = 5:5) micro array to oxygen content is plotted in Figure 4.34. The resistance values utilized were those obtained after 17 hours exposure of the sensor to the new gas. The slope of about 1/2 on the log-log plot is not characteristic of a bulk controlled defect reaction.

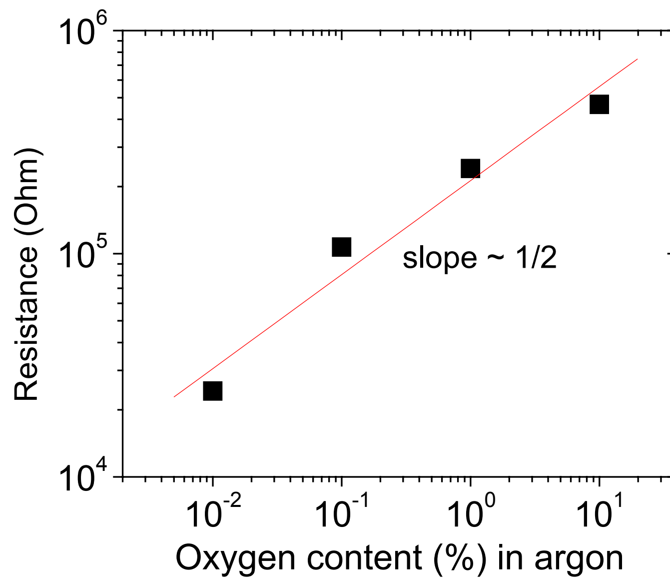

Figure 4.34 Relation of resistance of ZnO ($Ar:O_2$ = 5:5) micro array and oxygen contents in argon. The resistance was measured by AC impedance spectra without biases at 420º C for 17 hours.

The influence of temperature on the response time of ZnO to oxygen/argon mixtures was also investigated. First, the ZnO micro array was exposed to 10% oxygen in argon for more than 20 hours. After the resistance was stabilized, the ZnO was exposed to oxygen contents of 1, 0.1 and 0.01% continuously for 5 hours at temperatures of 380, 420 and 460 °C. The AC impedance spectra were measured every 5 minutes. Figure 4.35 shows the resistance change of for another ZnO ($Ar:O_2$ = 3:7) specimen at each temperature following a series of changes in the oxygen/argon mixtures.

The resistance of ZnO decreased with increasing temperature and decreasing oxygen content. Upon exposure to different oxygen/argon mixtures, an initial rapid change was followed by a slower transient particularly evident at the lower isotherm. As the temperature is increased, the relaxation times of these two regimes become shorter. By 460 °C, the resistance reaches a near steady state value nearly immediately except for the lowest oxygen partial pressure.

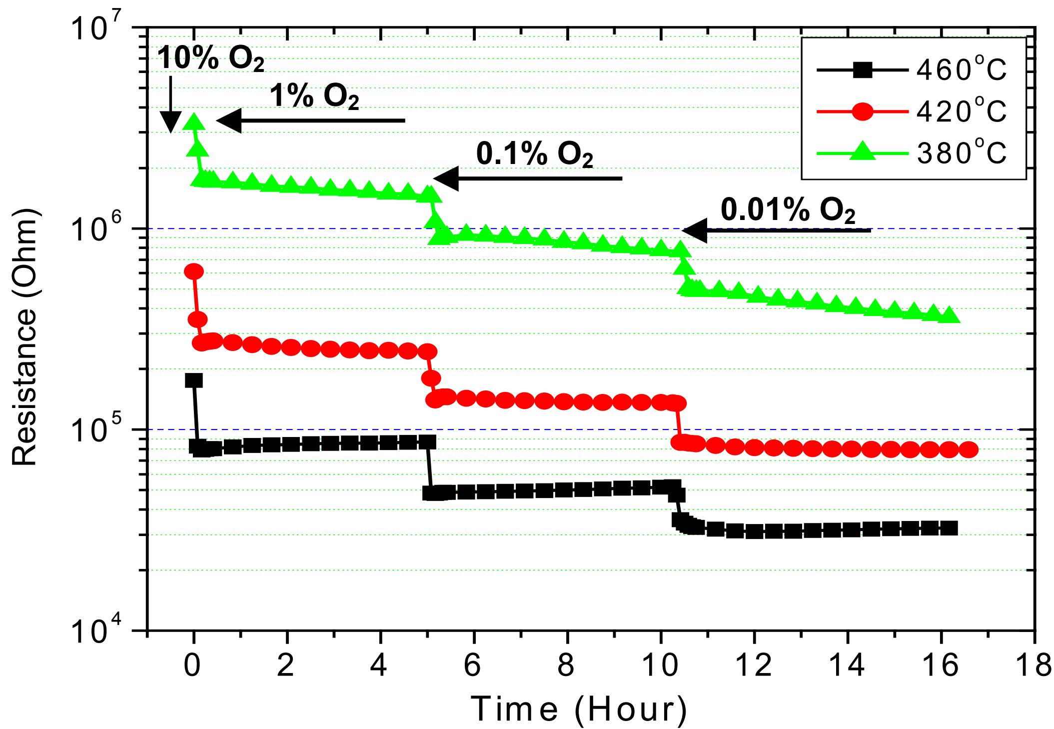

Figure 4.35 Resistances of ZnO ($Ar:O_2$ = 3:7) measured in oxygen/argon mixtures at the temperatures of 380, 420 and 460º C. The ZnO was exposed from 10% oxygen to the oxygen/argon mixtures of 1, 0.1 and 0.01% for 5 hours.

The resistance of ZnO ($Ar:O_2$ = 3:7) is plotted in Figure 4.36 as a function of oxygen partial pressure after exposure of 5 hours. ZnO, at higher operating temperature, has a somewhat stronger dependence than at lower temperature perhaps due to the slower kinetics at reduced temperatures.

Figure 4.37 shows the temperature dependence of the resistance of the ZnO ($Ar:O_2$ = 3:7) micro array for several different oxygen atmospheres. The resistance was measured from the AC spectra following exposure of 20 hours in 10 and 0.01% oxygen in argon environments. The activation energies are 1.0 and 0.99 eV in 10% and 0.01% oxygen in argon respectively.

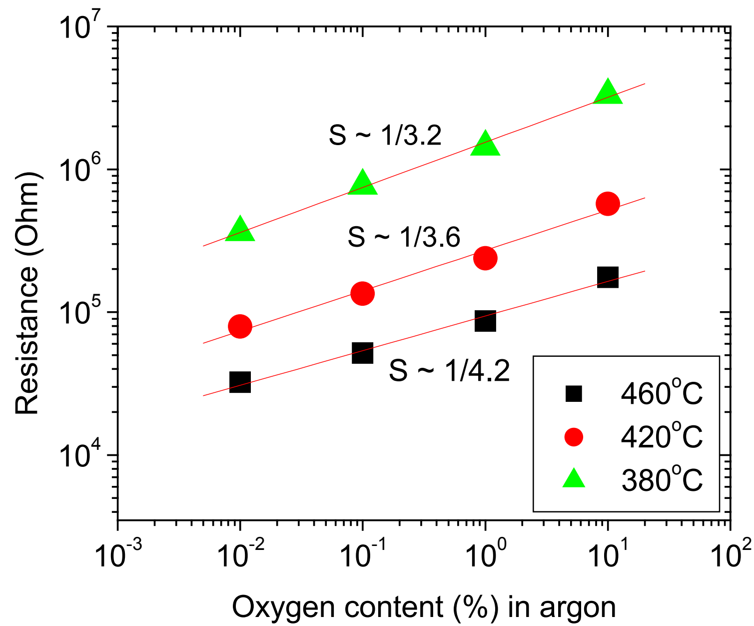

Figure 4.36 Resistance of ZnO (Ar:O_2 = 3:7) in oxygen/argon mixtures. The resistance was measured by AC impedance spectra without biases after the exposure of 5 hours.

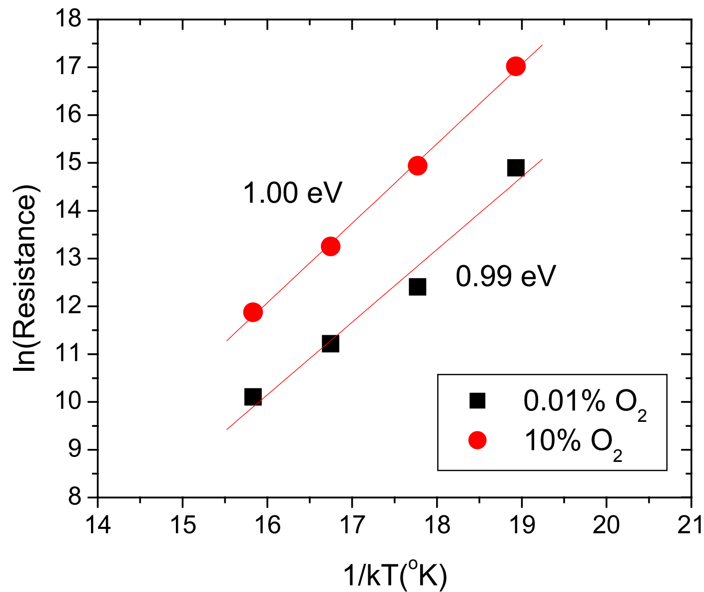

Figure 4.37 Resistance of ZnO (Ar:O_2 = 3:7) with operating temperatures. The resistance was measured from AC impedance spectra without biases after the 20 hours of the exposure to 10% and 0.01% oxygen in argon.

4.3.2 Time dependent DC bias effects

In investigating the sensor performance, the resistance of the ZnO micro arrays was found to be DC bias and time dependent. For purposes of investigating the DC bias effect, resistance values were extracted from the AC spectra under various DC biases. All measurements were performed in dehumidified air. First, ZnO was heated to 460 ºC for 24 hours for stabilization before starting measurements. AC measurements, with 1V DC bias applied all the times, were performed every 5 minutes for 2 hours at the same temperature. After the first set of measurements of 2 hours, the DC bias was removed while the temperature was maintaining at 460 ºC. A second set of measurements was then repeated after 24 hours. Figure 4.38 shows the time dependence of the total resistance of ZnO (Ar:O_2 = 7:3). In the first set of measurements, the resistance markedly increased within the first approximately 30 min, nearly saturating after 2 hours. The AC impedance spectra measured at each time have both high and low frequency semi-circles, and both increased with time. In the second measurements following after 24 hours from the first set, the resistance increased with time in a similar manner to the first measurements. Surprisingly, the resistance did not fully recover even after 24 hours with the DC bias removed.

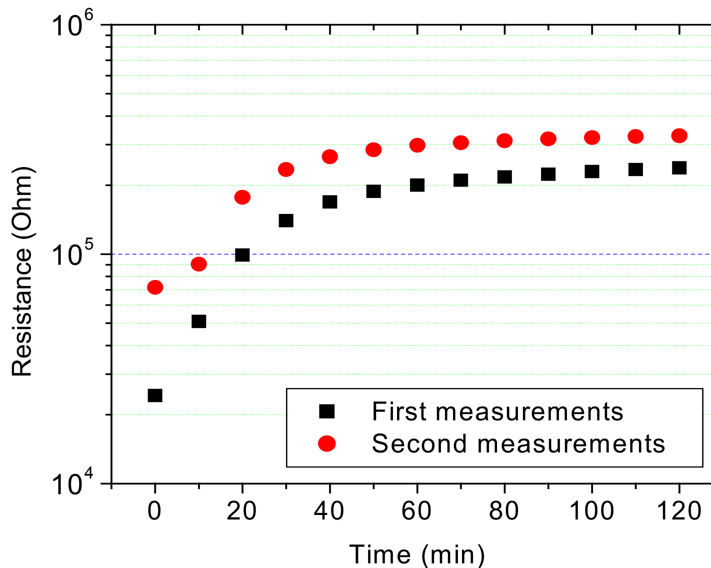

Figure 4.38 Resistance drifts of ZnO (Ar:O_2 = 7:3) micro array in dry air at 460º C. AC impedance spectra was performed in every 5 min for 2 hours each set of measurements. DC 1V bias was applied during the measurements of 2 hours. Between first and second measurements, ZnO was left at 460 °C without applied biases for 24 hours.

Since such time dependent DC bias effects have not been reported extensively before, I investigated these phenomena more extensively in different gas environments. Because DC bias applied during the AC measurement is often useful in deconvoluting different contributions to the overall spectra, bias was also used during the measurements. The specific measurement conditions which were utilized (every 5 minutes) are listed in Table 4.6. For period A, the baseline of resistance without any bias effects was established. After period A, a 1V DC bias was applied between each measurement in period B. When measurements were made, however, during this period they were performed alternately with and without DC bias. In period C, the measurement condition was the same as that in period A, and the relaxation process was anticipated at these times. Measurement conditions in period D were identical to those of period B. Finally, in period E, the measurement conditions were similar to those of period B except for a reversal in the polarity of the applied voltage, i.e. –1V instead of DC 1V bias for investigating reverse bias effects. Figure 4.39 shows the time dependent resistance of a ZnO ($Ar:O_2$ = 5:5) micro array, in dry air at 420 °C, under programmed DC bias as defined in Table 4.6.

Table 4.6 Conditions of AC impedance spectra measurements

	Time (hour)	DC bias in pretreatment	DC bias in measurement
A	3	DC 0V	DC 0V
B	6	DC 1V	DC 0V or DC 1V
C	5	DC 0V	DC 0V
D	6	DC 1V	DC 0V or DC 1V
E	6	DC –1V	DC 0V or DC –1V

During period A, the resistance of ZnO without bias exhibits a constant stabilized value. However, upon applying the DC bias, the resistance changes abruptly. In period B, with 1V DC bias applied during measurements, the resistance drops sharply initially and then gradually increases with time until it saturates at a value higher than that in period A. The shape of the resistance drift with time is similar to that observed earlier for ZnO ($Ar:O_2$ = 7:3) in Figure 4.38. The resistance measured without bias in period B, however,

is immediately higher than the resistance in period A. In period C, the resistance gradually decreases with time, approaching the value initially obtained during period A. The shape of resistance drift in period D is similar to that obtained in period B, although the resistance is slightly higher. In period E, the shape of resistance drift is similar to that of period B and D. Initially, there is a small drop in the zero bias value but the resistance quickly recovers to nearly the same magnitude as for positive bias. There does, however, appear to be a decrease in the saturation value of the resistance measured under bias.

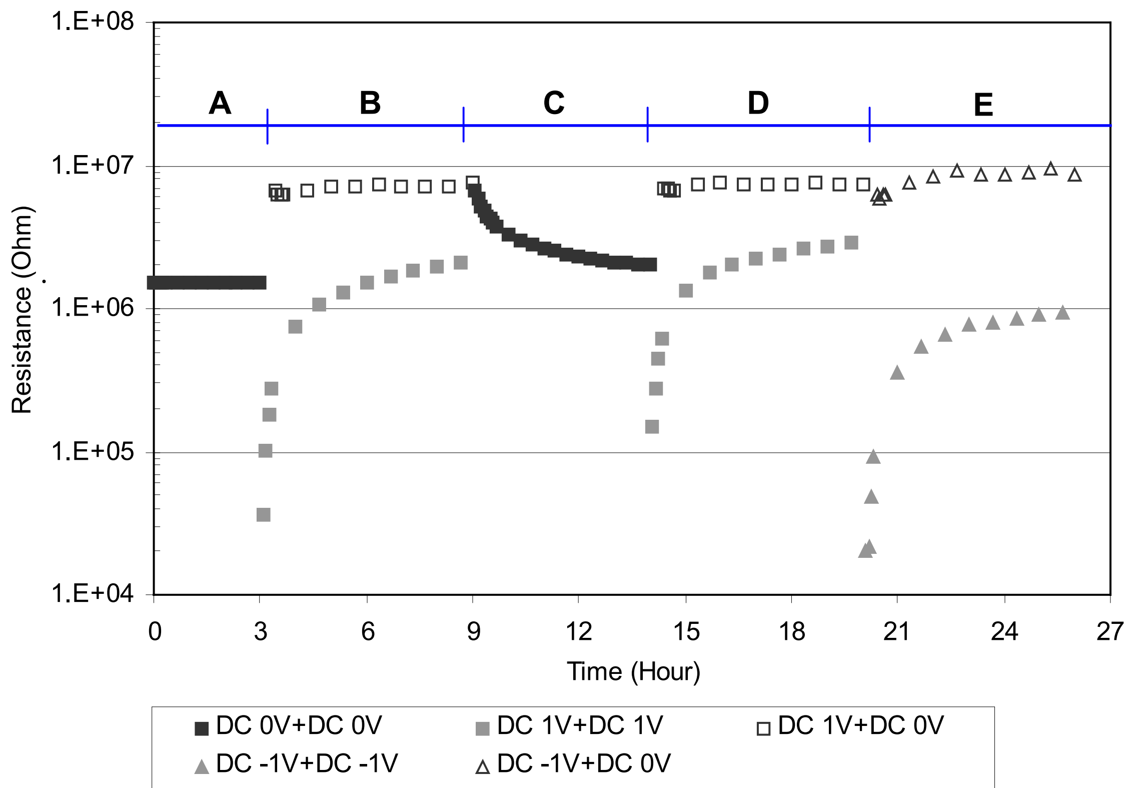

Figure 4.39 Resistance drift of ZnO ($Ar:O_2$ = 5:5) micro array in dry air at the temperature of 420º C. The AC impedance spectra were utilized with DC biases of 0, 1 or –1V during the pretreatment and measurement.

The AC spectra generally consisted of two semi-circle components. The resistance values in Figure 4.39 represents the sum of the two series resistance components. Figure 4.40 (a) shows the AC impedance spectra obtained in regions A and B at the end of each period.

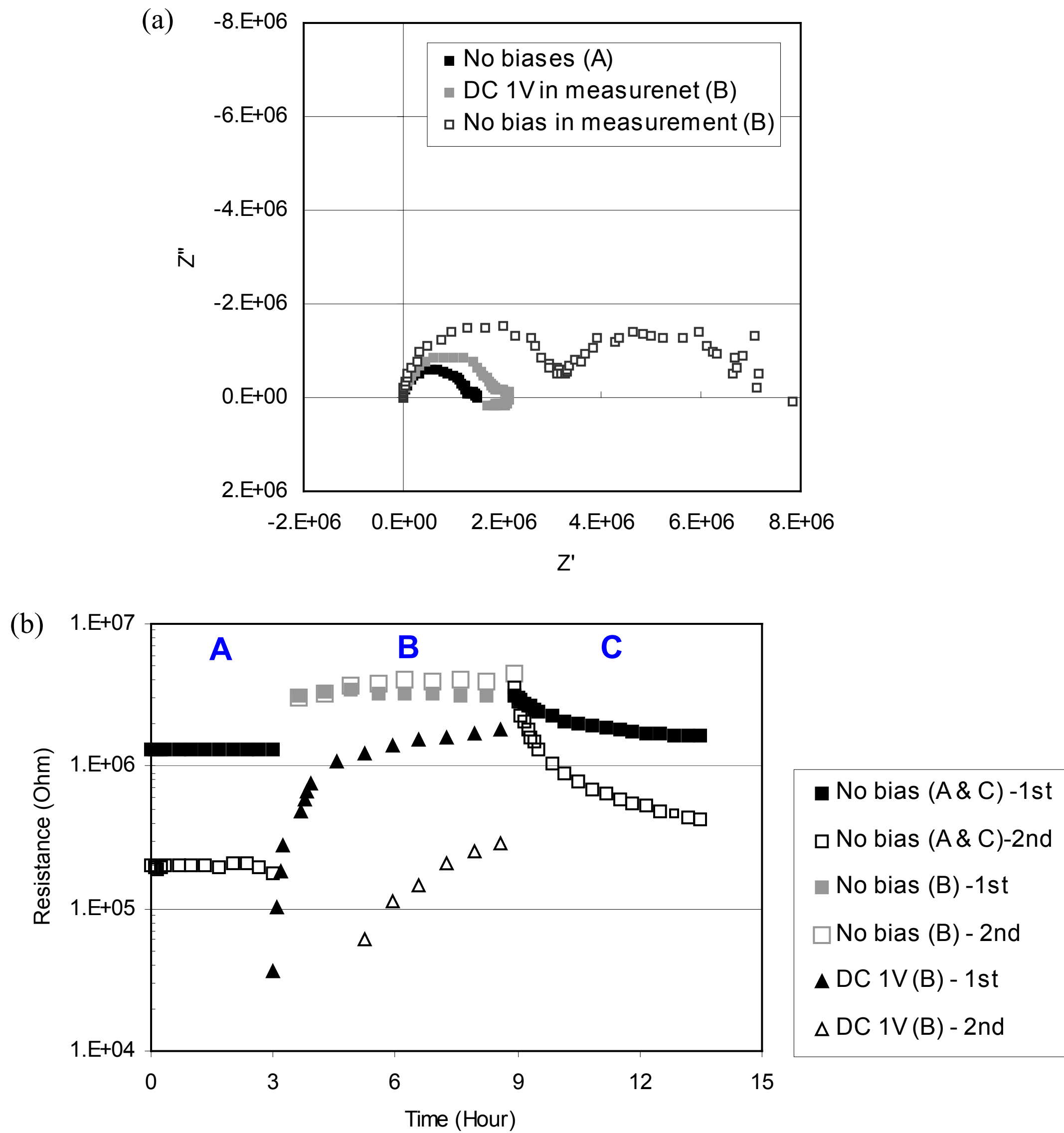

Figure 4.40 Time dependent DC bias effects of ZnO ($Ar:O_2$ = 5:5) micro array in dry air at the temperature of 420º C. (a) AC spectra at each experiment regime and (b) Resistance drifts with DC 1V bias

As shown in Figure 4.40, the DC bias significantly modifies the AC spectra. Without bias in period A, the resistance of the high frequency semi-circle is almost ten times

higher than that of second semi-circle component. However, by applying a 1V DC bias prior to each measurement, the AC spectra becomes strongly dependent on the DC bias during measurement. Both semi-circles shrink initially after application of the bias, and then begin to increase with time. In region B where the spectra are measured without bias, both semi-circles increase in size, with the second semi-circle becoming nearly the same size as the first one. During the relaxation period C, the low frequency semi-circle shrinks faster with time compared to the high frequency one.

To investigate the influence of the magnitude of the DC bias on the resistance, the measurements were repeated with a reduced bias of 0.2V and –0.2V. Figure 4.41 shows the corresponding time dependence of the resistance components. With a 5 fold reduction in bias magnitude, while the time dependent resistance variations were still observed, the magnitude of the resistance changes was correspondingly reduced with the same ratio.

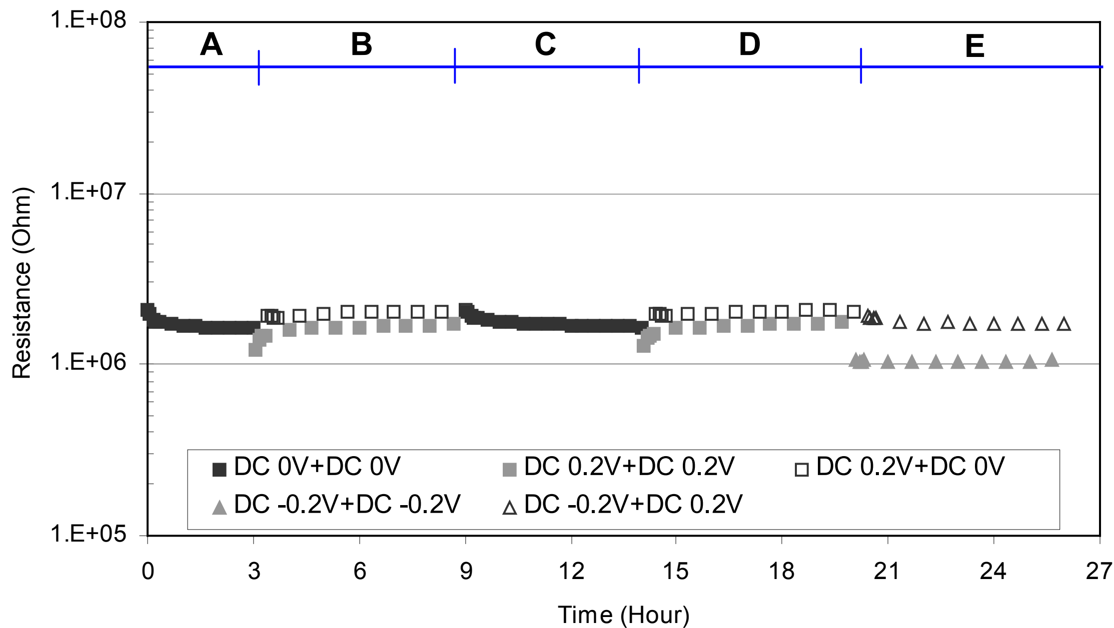

Figure 4.41 Resistance drifts of ZnO (Ar:O_2 = 5:5) in dry air at 420º C. The AC impedance spectra were utilized with DC 0.2V bias during pretreatment and measurement.

DC bias effects were also investigated for Al doped ZnO. The AC spectra were somewhat more distorted due to high conductivity. While DC bias effects could be

observed, changes of resistance due to bias were much smaller those of undoped ZnO films. Figure 4.42 shows the AC impedance spectra with DC 1V bias obtained in regions A, B and C at the end of each period in air at 420 °C.

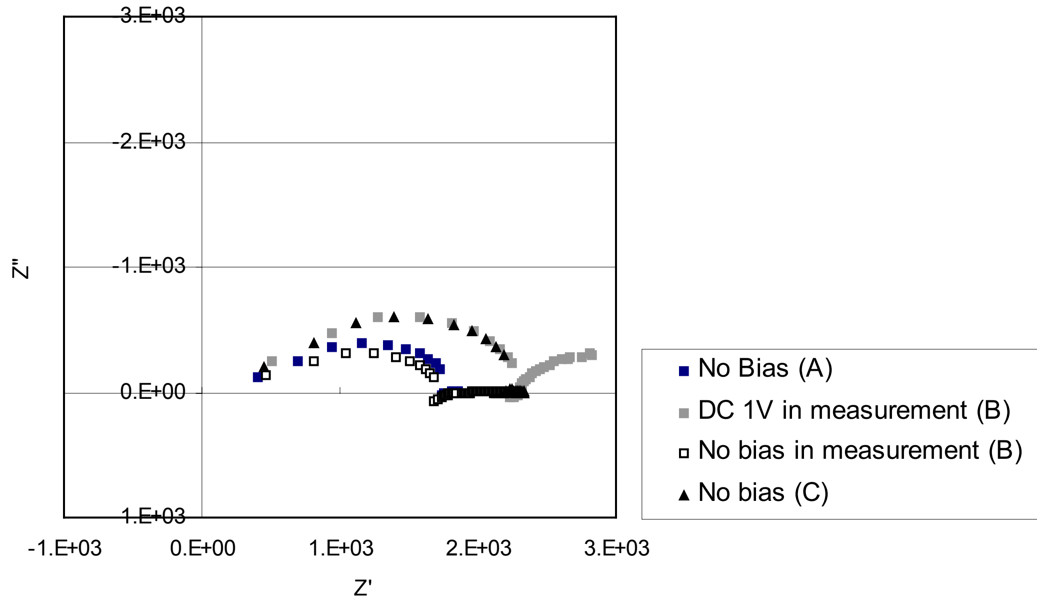

Figure 4.42. AC spectra of Al doped ZnO micro array at each experiment regime in dry air at the temperature of 420º C. The AC impedance spectra were utilized with DC 1V bias.

These bias effects were also investigated for other sensor materials. First, SnO_2, a popular commercial sensor material, was examined as a thin film micro array using the same program as in Figure 4.39. Figure 4.43 shows the resistance drift of SnO_2 in dry air at 400 °C. The results are similar to those obtained for the ZnO micro arrays.

CTO, the p-type semiconductor, was also investigated. Figure 4.44 shows the resistance drift of CTO micro array in dry air at 420 °C which were found to be much reduced compared to that in ZnO and SnO_2.

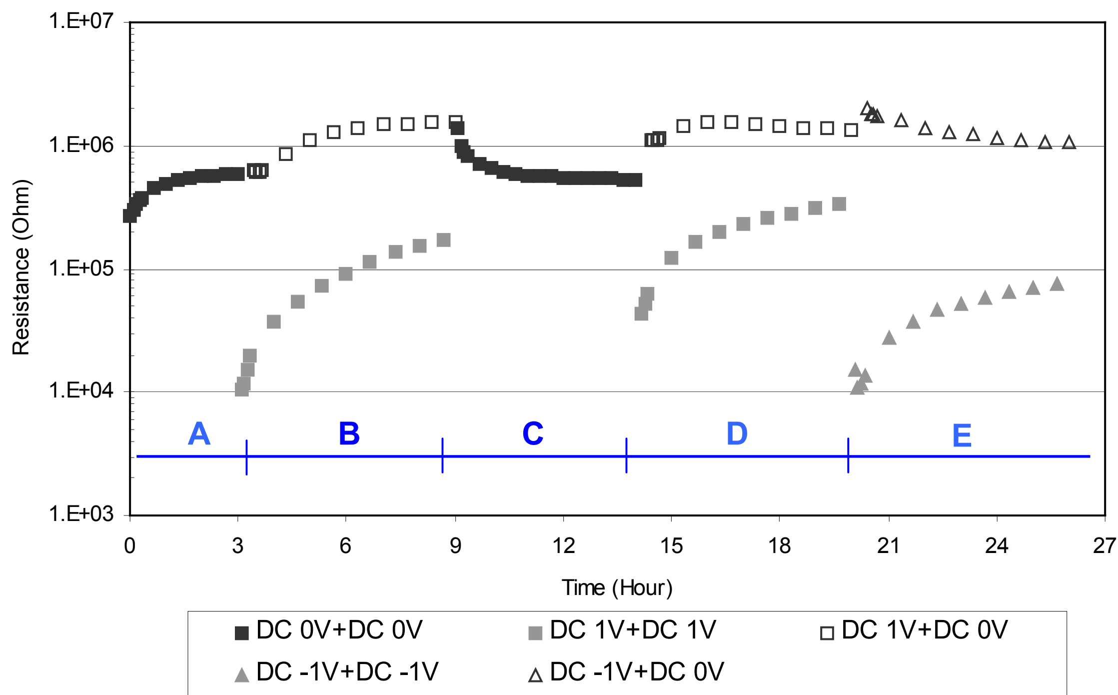

Figure 4.43 Resistance drifts of SnO_2 micro array onto micromachined platform in dry air at 400º C. The AC impedance spectra were utilized with DC 1V bias.

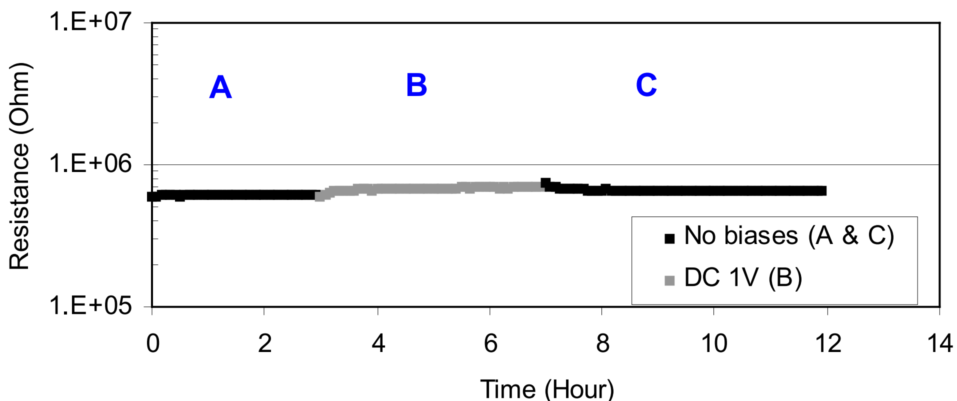

Figure 4.44 Resistance drifts of CTO micro array in dry air at 420º C. The AC impedance spectra were utilized with DC 1V bias.

Next, we examine the same phenomena in atmospheres representative of conditions expected during sensor operation. The resistance drift studies were performed on ZnO in 100 ppm H_2 in air at 420 °C as shown in Figure 4.45. The resistance of ZnO in 100 ppm H_2 is smaller than those in dry air, as expected. The time dependent DC bias effect was also observed even in 100 ppm H_2 environment.

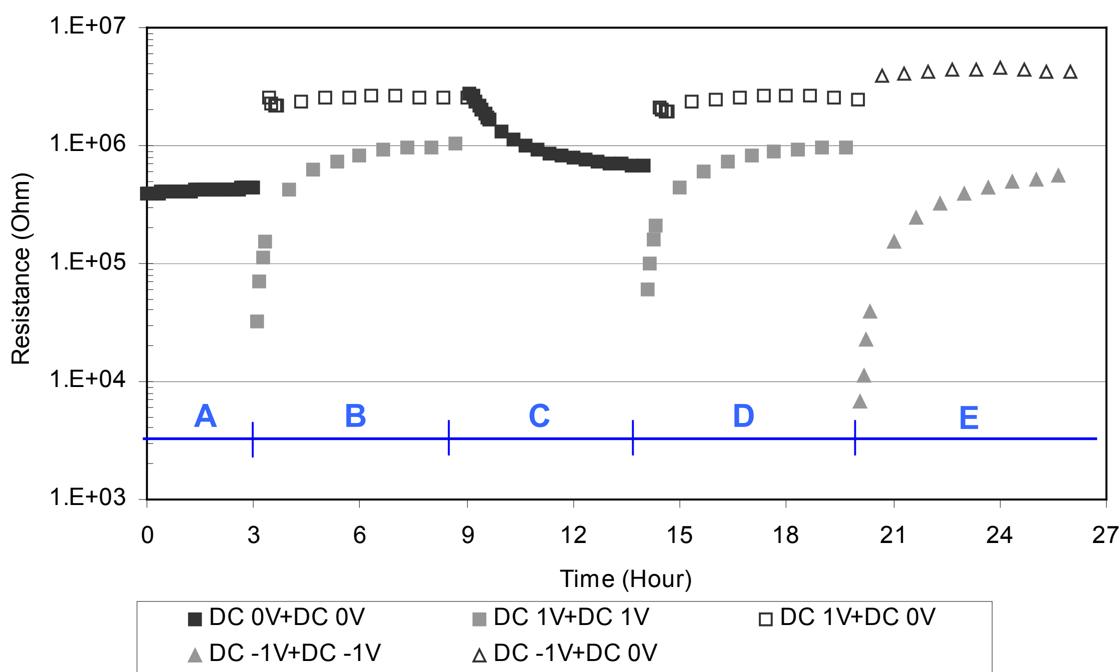

Figure 4.45 Resistance drift of ZnO ($Ar:O_2$ = 5:5) in 100 ppm H_2 of dry air at 420º C. The AC impedance spectra were utilized with DC 1V bias.

The resistance drift of ZnO by the bias was also investigated in different oxygen/argon mixtures. First, ZnO was exposed to an argon only environment and the spectra were examined every 5 minutes without applied bias for 3 hours. After the exposure to argon, ZnO was exposed to the oxygen/argon mixture. The measurement scheme in the oxygen/argon mixtures was same as listed in Table 4.6. The oxygen/argon mixtures were 10%, 1%, 0.1% and 0.01% oxygen content in argon.

The shape of resistance drift of ZnO in more than 1% oxygen was similar to that in dry air as shown in Figure 4.39. However, the resistance drift in less than 0.1% oxygen showed a somewhat different behavior. Figure 4.46 shows the resistance drift of ZnO ($Ar:O_2$ = 5:5) in 1 and 0.1% oxygen at 420 °C. The overall resistance value in 1% oxygen is higher than that in 0.1% oxygen as expected.

When ZnO was exposed to argon initially for 3 hours, the resistance decreased. Then, the resistance of ZnO increased after exposure to the oxygen/argon mixtures in period A. The resistance in 1% oxygen easily saturated and showed a similar time

dependent DC bias effect as in dry air. The resistance of ZnO in 0.1% oxygen differed in that the resistance with bias was lower than without bias.

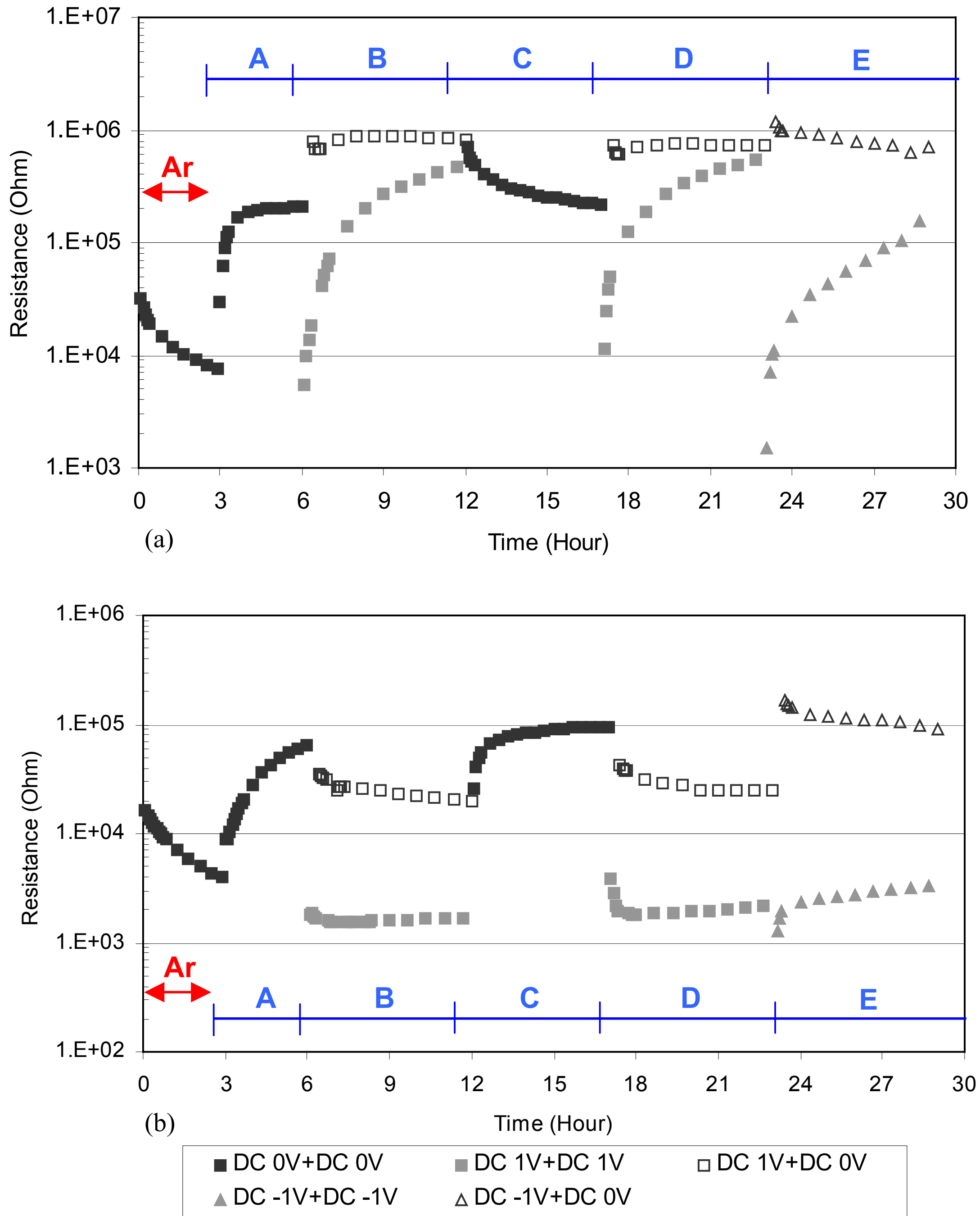

Figure 4.46 The resistance drift of ZnO micro array in oxygen/argon mixtures at 420º C. The AC impedance spectra were utilized with DC biases of 0, 1 or –1V during pretreatment and measurement. (a) In 1% O_2 in Ar and (b) In 0.1% O_2 in Ar

Given the close spacing between electrodes, high electric fields are generated even for small voltages of the order of volts. Given that high fields can induce ion migration, it was of interest to see if built-in fields could be induced via polarization effects. To test this hypothesis, surface potential image were observed using AFM techniques utilizing Si conductive probes.

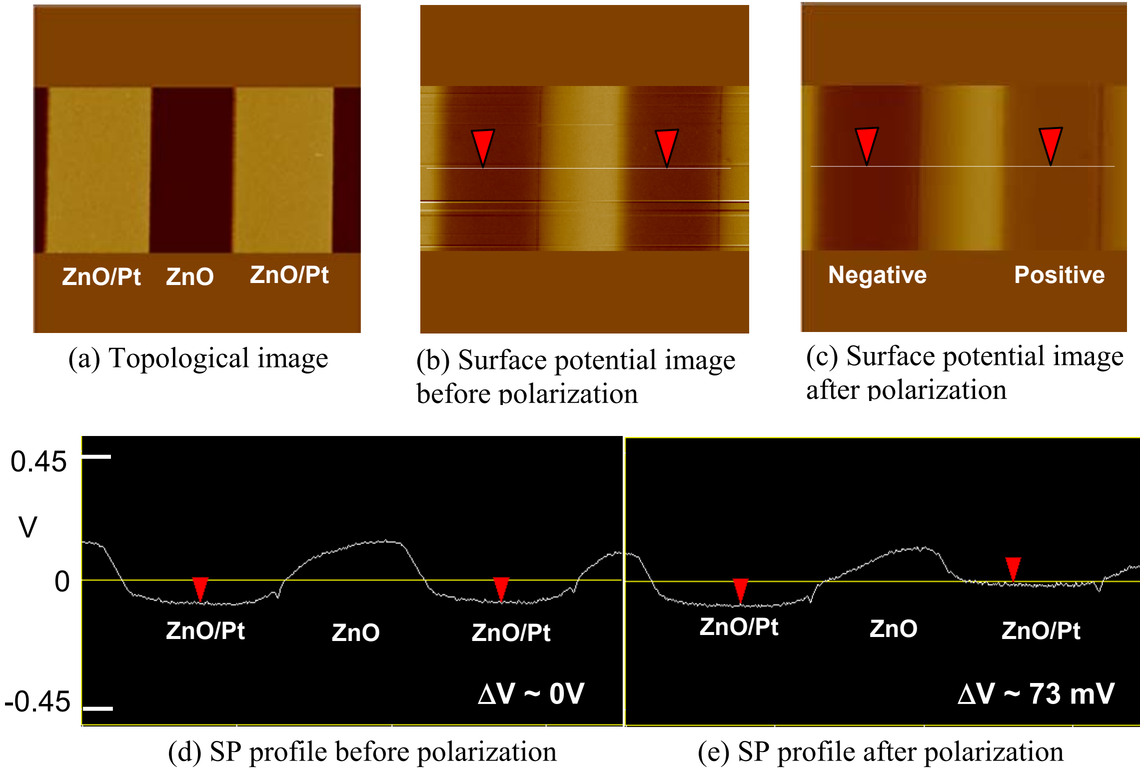

(a) Topological image (b) Surface potential image before polarization (c) Surface potential image after polarization

(d) SP profile before polarization (e) SP profile after polarization

Figure 4.47 Observed AFM images of ZnO micro array (Ar:O_2 = 3:7) during polarization DC 5V was applied to micro array in 2 hours at 500 °C for polarizing ZnO micro array.

Figure 4.47 shows the surface potential images after 48 hours of polarization of a ZnO micro array (Ar:O_2 = 3:7). The polarization was performed by applying 5V DC to a micro array at 500 °C for 2 hours. As shown in Figure (b) and (d), without DC bias, the surface contact potentials of two ZnO/Pt regions are nearly the same. However, ZnO/Pt regions show different surface contact potential values after polarization even though the observation was obtained 48 hours after polarization. The ZnO/Pt region, with positive applied voltage, shows higher contact potential than the region with negative voltage.

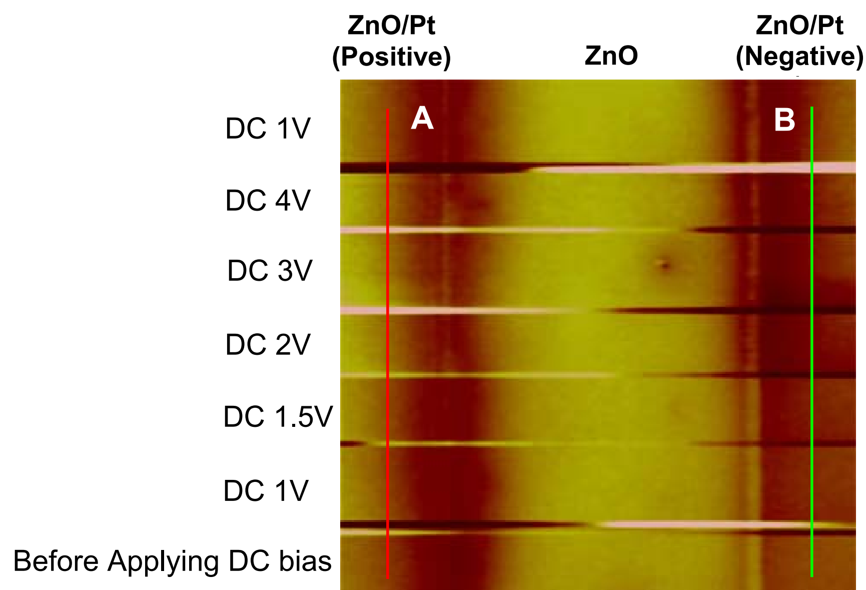

(a) Surface potential image during applied voltage

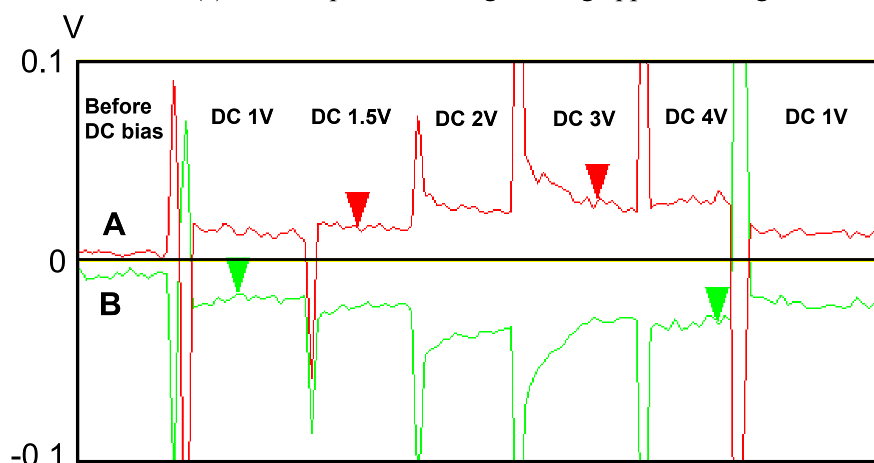

(b) Surface potential profile during applied voltage

Figure 4.48 AFM images of ZnO micro array (Ar:O_2 = 3:7) during applying DC voltage to interdigited electrodes.

For investigating the effect of applied voltage on surface contact potential, the DC voltage was applied to the interdigited electrodes during AFM observation at room temperature as shown in Figure 4.48. With an increase of DC bias, the potential of the ZnO/Pt region with positive applied voltage increased while the potential of the other ZnO/Pt region decreased. When the DC bias decreases, for example, from 4V to 1V, the

potential difference between two electrodes is reduced to almost the initial value. Such behavior was also found elsewhere [85].

Summary of key observation

1. ZnO micro arrays show a fast and slow response to changes in exposure of O_2/Ar mixtures.
2. As the temperature is increased, the relaxation times of these two regimes become shorter.
3. DC bias significantly modifies the AC spectra with time
4. Smaller DC biases reduce the magnitude of the resistance changes.
5. Al doped ZnO shows a smaller DC bias effect than undoped ZnO.
6. SnO_2 and CTO shows the time dependent DC bias effect while CTO has much reduced resistance drift
7. Time dependent DC bias effects are found in 100 ppm H_2 and O_2/Ar mixtures
8. The ZnO/Pt region, with positive applied voltage, shows higher contact potential than the region with negative voltage after polarization treatment.

5. Discussion

5.1 The influence of processing conditions on the properties of ZnO films

ZnO micro array sensors fabricated on Si based substrates, utilized varied processing conditions, e.g. O_2/Ar ratios during sputter deposition, post deposition annealing temperature and Al doping to investigate the roles of structure and composition on sensor response. Reactive sputtering, compatible with IC fabrication, was utilized for film deposition. Zn rather than ZnO targets, provided several advantages including high purity targets, high deposition rates and ability to achieve controlled stoichiometry by control of the O_2/Ar ratio within the sputtering chamber.

The O_2/Ar ratio during sputtering controlled the film deposition rate. The deposition rate decreased with increased oxygen concentration. Above an oxygen concentration of 40%, the deposition rate decreased abruptly as shown in Figure 3.1. With higher O_2/Ar ratio, the surface of the Zn metal target easily oxidized, leading to a reduction in the sputter rate. Furthermore, oxygen, as a sputter gas, has lower sputter yield than argon.

The influence of processing conditions on the physical properties of the ZnO films was observed using XRD, AFM, and FIB-SEM. All undoped ZnO films show largely c-axis orientation. This is reasonably given that the c-plane of ZnO corresponds to the densest packed plane. Under optimized conditions, the c-axis orientation is frequently observed in sputtered polycrystalline films even on glass substrates [51]. Figure 4.3 and Table 4.1 show the influence of O_2/Ar ratio and post deposition annealing on the crystalline quality of the undoped ZnO films. When the oxygen concentration is increased, XRD shows the intensity of the (002) peak to increase and the value of FWHM to decrease. Therefore, films deposited with higher O_2/Ar ratios lead to more highly oriented and crystalline structures. The improved crystalline quality with increasing oxygen content is likely related to the lower deposition rate at higher O_2/Ar ratio. The lower deposition rate provides more time for Zn and O atoms to diffuse on the surface to low energy sites of the crystal, resulting in enhanced crystalline perfection and grain growth. AFM observation shows that ZnO films with higher O_2/Ar ratio have larger grain size and smoother surfaces. The influence of O_2/Ar ratio on the microstructure of ZnO films is consistent with previous reports [52, 53].

Post deposition annealing also affects the crystalline quality of the undoped ZnO films. With an increase of annealing temperature, the intensity and sharpness of the XRD peaks increased. Beside the enhanced crystalline quality, the stress state of the ZnO films also changes. The diffraction peak position of as grown films is less than that of the reference ZnO powder, and with an increase of annealing temperature, the peak position approaches the powder value and ultimately deviates in the opposite direction. The deposited films appear to be elongated along the c-axis, with compressive forces acting in the plane of the ZnO films. This compressive stress becomes weaker as the annealing temperature increases, resulting in a decrease in spacing between (002) planes. Further increase of annealing temperature induces tensile stresses in the plane of the ZnO film. These observations regarding the effects of annealing on the quality of sputtered ZnO films are well known and correspond to the result by Gupta et al [60] who have investigated and reviewed annealing effects on ZnO films.

Al doped ZnO films have very distinctive XRD patterns compared to those of undoped ZnO films as shown in Figure 4.5 and Table 4.3. Al doped ZnO exhibits (100) and (101) peaks but with low intensity and does not show the (002) peak easily observed in undoped ZnO films. Post deposition annealing treatments also has little effect on the crystalline structure of Al doped ZnO. This indicates that as grown Al doped ZnO films have a mixed oriented structure which remains largely intact even after post annealing. Also, AFM observation shows that Al doped ZnO films have rough surfaces with agglomerate grain shape, with surface features remaining intact even after 700 °C annealing. Surface roughness and less compact structure may be attributed to migration of Al dopants towards the grain boundary, where they react with oxygen atoms and segregate as Al_2O_3 [65]. Cross sectional views reveal the porous microstructure of films annealed at 700 °C. Fine pores appear to be mainly located in the interface region between film and substrate.

XRD patterns of sputtered Al doped ZnO films being developed for transparent electrodes have often exhibited (100) and (101) rather than the (002) peak of the c-axis orientation [62-65]. As illustrated in Figure 5.1, this has been attributed to the existence of Al_2O_3 grains which disturb the nucleation of the columnar structure characteristic of the c-axis growth [64].

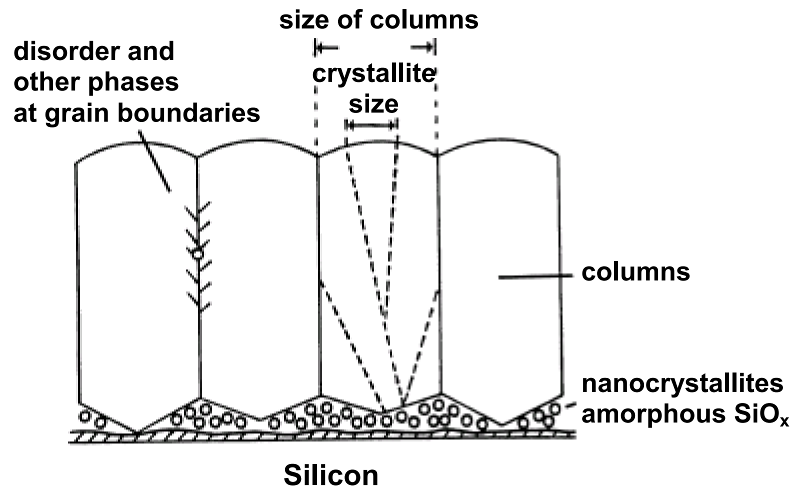

Figure 5.1 Schematic representation of the structure of sputtered ZnO films [64]

The stoichiometry of ZnO films was investigated by WDS as shown in Figure 4.10 and Table 4.5. The oxygen content of undoped ZnO increased with corresponding increases in O_2/Ar ratio during sputtering. This is likely related to both the increase in oxygen partial pressure as well as the lower deposition rate with higher O_2/Ar ratios. The slow deposition rate might provide oxygen atoms more time to incorporate into the films. Al doped ZnO films have higher oxygen content compared to the undoped ZnO films. This is consistent with the fact that Al dopants should be compensated by the formation of Zn vacancies leading to oxygen excess overall. By annealing at 700 °C, the undoped ZnO films approach the stoichiometric ratio (Zn:O = 1:1) suggesting that during deposition, they go down with a degree of oxygen deficiency.

5.2 The influence of processing conditions on sensor performance

ZnO is well known to behave as an n-type semiconductor even without donor doping due to oxygen deficiency induced during processing [44]. This is consistent with the response of the ZnO films examined in this work, i.e. decrease in resistance when exposed to the reducing gases H_2 and CO, and increase in resistance when exposed to the oxidizing gas NO_2.

First, the sensor response of ZnO films with Ar:O_2 = 3:7 and 7:3 are compared given their different physical and chemical properties. ZnO (3:7) exhibits higher sensitivity to the gases examined than ZnO (7:3). This may be related to the expected decrease in electron density in the more highly oxidized ZnO (3:7) as reflected in the higher resistivity observed, for example, at 420 °C in Figure 4.14. This, in turn, implies a higher depletion width, W in the ZnO (3:7). To illustrate the impact on sensor response I refer to the illustration in Figure 5.2. I assume a compact layer model since sputtered undoped ZnO films have highly crystalline and dense structures. For the thin films (about 300 nm) utilized in this study, the depletion width W is expected to represent a significant fraction of the total film thickness. Thus, modulation of W by exposure to different gases is expected to have a greater impact on the film resistance with the lower carrier density and therefore the greater depletion width.

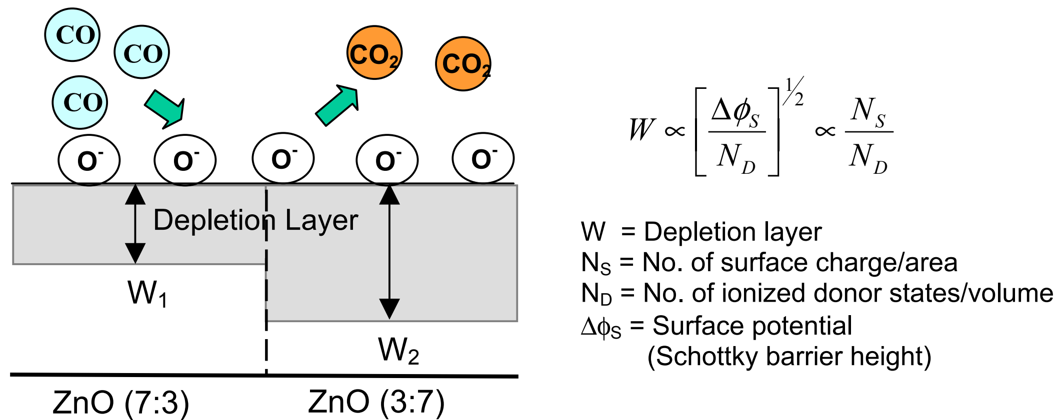

Figure 5.2 Schematic comparison of relative influence of adsorbed gases on the depletion layer width of ZnO prepared with different O_2/Ar ratios.

The depletion layer W is estimated using equation (2.7) and the dimensions of the ZnO micro arrays as shown in Figure 5.3. The ZnO micro array consists of 17 resistors with parallel connections since the total number of each interdigited electrode is 19. Thus, the resistivity of the ZnO films, ρ, will be defined as below:

$$R = \frac{1}{17} \times \rho \times \frac{l}{A} \quad (5.1)$$

$$\rho = 17 \times R \times \frac{A}{l} \quad (5.2)$$

Assuming the region between two parallel electrodes only acts as a resistor, the area (*A*) will be 1.7125 x 10^{-6} cm^2 (width of ZnO film (685 μm) x thickness of electrode (0.25 μm)) and the length (*l*) will be the distance between two electrodes (18 μm). Therefore, the conductivity, σ, will be defined as below:

$$\sigma = \frac{1}{\rho} = \frac{l}{17 \times R \times A} = \frac{18 \times 10^{-4}\, cm}{R \times 17 \times 1.7125 \times 10^{-6}\, cm^2} \approx \frac{62}{R} \quad (5.3)$$

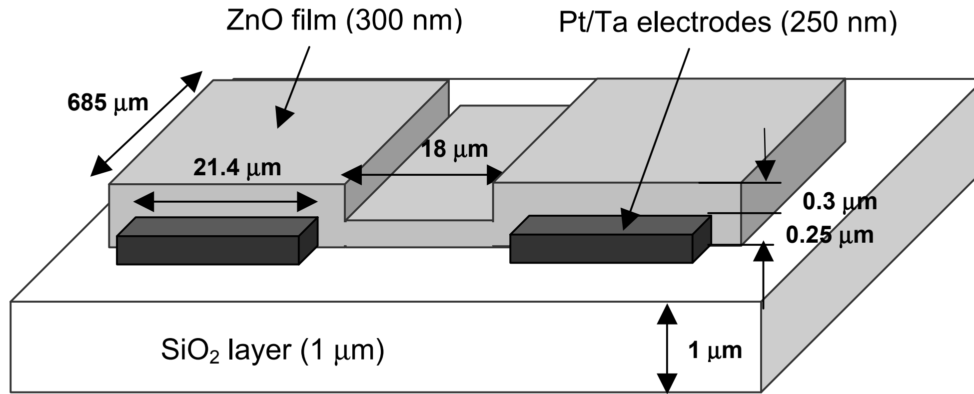

Figure 5.3 Schematic dimensions of ZnO micro arrays including ZnO film, two Pt/Ta interdigited electrodes and SiO_2 layer

At 420 °C, the resistance of the ZnO micro arrays is around 8 x 10^4 Ω for $Ar:O_2$ = 7:3 and 8.4 x 10^5 Ω for $Ar:O_2$ = 3:7. Thus, the conductivity of each is 7.8 x 10^{-4} S/cm and 7.4 x 10^{-5} S/cm respectively. This conductivity value is mainly contributed by electron since ZnO is an n-type electronic conductor. Thus, the charge carrier concentration (*n*) can be estimated using the following equation,

$$n = \frac{\sigma}{e\mu} \tag{5.4}$$

The calculated charge carrier concentration is around 10^{14} cm^{-3} for ZnO (7:3) and 10^{15} cm^{-3} for ZnO (3:7) using the mobility value (μ) of 5 cm^2/Vs [66, 67]. Finally, the depletion layer width is:

$$W = \frac{Q_S}{e \cdot N_D} = [\frac{2 \cdot K \cdot \varepsilon_O \cdot \Delta\phi_S}{e \cdot N_D}]^{1/2} \tag{2.7}$$

The calculated depletion width is around 1000 nm for ZnO (7:3) and 3000 nm for ZnO (3:7). The calculated depletion widths are large compared to the film thickness (300 nm). This suggests that the DC resistance measured during gas response experiments does not reflect the bulk resistance of ZnO but rather is controlled by Schottky contacts or grain boundary barriers. This will be discussed further when treating the AC impedance data.

ZnO films with $Ar:O_2$ = 5:5 and 3:7 showed very similar gas sensor performance when exposed to a various gases at different temperatures. This is consistent with their similar physical and chemical properties discussed in a previous chapter.

The influence of post annealing on these two ZnO films ($Ar:O_2$ = 5:5 and 3:7) can be easily observed in Figure 4.11. Undoped ZnO films annealed at 700 °C in air for 12 hours show reasonable gas response with low and stable baseline resistance while undoped ZnO films annealed at 500 °C show poor gas response with unstable baseline resistance. The higher resistance of ZnO films annealed at 500 °C may be related to their smaller grain size and higher oxygen content compared to the resistance of ZnO films annealed at 700 °C. The post deposition annealing at 500 °C may not be high enough to stabilize the structure of the ZnO films compared to their operating temperatures (300 – 500 °C). For example, the baseline resistance of ZnO annealed at 500 °C, which is higher than that of ZnO annealed at 700 °C, continuously decreases during gas response measurements at 420 °C as shown in Figure 4.11. This is not the case for ZnO films annealed at 700 °C.

The effect of Al doping on sensor responses is featured in Figure 4.11 and 4.16. Al doped ZnO films show measurable sensor response even when annealed at 500 °C. These characteristic features are directly related to the modification of properties of ZnO films induced by the addition of the foreign atom, Al.

The lower baseline resistance derives from the higher charge carrier concentration resulting from the donor nature of the substitutional Al^{3+} on Zn^{2+} sites. The resistance of the Al doped ZnO films increase with the increase of post annealing temperatures while the undoped ZnO films shows the opposite behavior. This may result from some Al ions migrating towards grain boundaries and segregating with the increase of annealing temperature. Indeed, the baseline resistance of Al doped ZnO films annealed at 500 °C increased continuously during sensor response measurements at 420 °C - see Figure 4.16 even though it had a measurable sensor response.

Al doped ZnO films show reasonable sensor responses even though they have lower resistance values than undoped ZnO. The baseline resistance and gas response of Al doped ZnO and ZnO with $Ar:O_2 = 3:7$ are listed in Table 5.1 from Figure 4.16. Although the resistance of Al doped ZnO annealed at 500 °C is smaller than ZnO ($Ar:O_2 = 3:7$) by about 3 orders of magnitude, their sensitivities are similar. The compact layer model with varied depletion layer, which was used for explaining the gas response of undoped ZnO films in Figure 5.2, is not consistent with these observations since in this model, the sensor film with lower resistance should have a weaker sensor response due to lower depletion width. However, the porous layer model should be considered rather than the compact layer model for Al doped ZnO films given their rough surface and porous microstructure. Figure 5.4 contrasts the gas sensing mechanisms operative in the compact and porous layer models. In undoped ZnO films, the gas sensing reaction is limited to the surface since the gas can't penetrate into the film. However, in Al doped ZnO, the gas can penetrate all of the volume of the film, and the gas sensing reaction will take place at the surface of each grain and grain boundary. Therefore, the sensitivity of Al doped ZnO films could be comparable or even higher even though they have lower baseline resistance.

Table 5.1 Gas responses of Al doped ZnO and ZnO with Ar:O_2 = 3:7 at 420 °C

	Al:ZnO at 700 °C	Al:ZnO at 500 °C	ZnO (3:7) at 700 °C
Baseline resistance (Ω)	6.1×10^4	4×10^2	3.6×10^5
R(Air)/R(100 ppm H_2)	6.0	2.0	2.2
R(Air)/R(50 ppm CO)	1.2	1.1	1.2
R(2 ppm NO_2)/R(Air)	-	1.3	1.3
R(Air)/R(50 ppm NH_3)	2.2	1.5	1.3

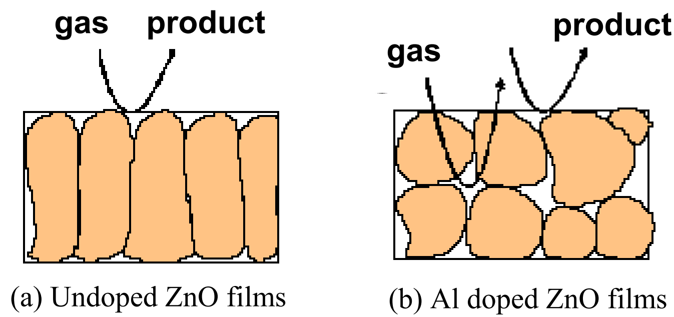

(a) Undoped ZnO films (b) Al doped ZnO films

Figure 5.4 Schematic view of gas sensing reaction in (a) Undoped ZnO films (compact layer) and (b) Al doped ZnO films (porous layer) [21] for ZnO micro array sensors

5.3 The electrical characteristics of ZnO thin film micro array sensors

The effect of processing conditions on the sensor response of ZnO thin films on micro array platforms has been discussed by evaluating only the overall DC resistance of the films. The resistance is a readily measured parameter and normally sufficient for purposes of comparing the performance of various sensors. However, for obtaining a more detailed understanding of the source of the response, this measurement alone is insufficient. Indeed, the overall resistance of thin film gas sensors represents a number of gas reactions which can take place at different locations including the surface, grain boundary and contacts and other interfaces. Figure 5.5 represents, schematically, various possible limiting current pathways and corresponding equivalent circuit elements representing a ZnO thin film micro array with interdigited Pt electrodes.

For purposes of understanding the source of gas sensitivity of a ZnO micro array, it is important that each of these contributions be investigated separately. In this study, AC impedance measurements, both with and without DC bias, have been utilized to assist in identifying the individual contributions to the sensor response. The measured AC spectra typically showed two semi-circular components, first a high frequency component extending from the origin and a second low frequency component at higher resistances.

In the ceramics literature, the high frequency semi-circle is commonly assigned to the "bulk" resistance of the grains [86, 87]. However, as observed in chapter 4.2.3, the diameter of the high frequency semi-circle is bias dependent demonstrating that this response is apparently non-ohmic, a feature normally attributed to interfacial processes. One possibility is the formation of Schottky barriers at the Pt-ZnO interfaces. As Pt has a higher work function of 5.7 eV than the work function of ZnO, 4.5 eV (both at room temperature), the formation of Schottky barriers is probable [88]. Figure 5.6 shows the energy band diagram for ideal metal semiconductor (MS) contacts between a metal and n-type semiconductor when the work function of the metal (Φ_M) is larger than the work function of the semiconductor (Φ_S) [89]. As shown in Figure 5.6 (c), applying $V_A > 0$ reduces the electron barrier in the semiconductor, and therefore allows a net flow of electrons from the semiconductor to the metal. Further increasing V_A leads to a rapidly rising forward bias current exponentially as shown in Figure 5.6 (e). On the other hand, applying $V_A < 0$ raises the electron barrier, and this blocks the flow of electrons from the

semiconductor to the metal. Some electrons in the metal are able to surmount the barrier, but the associated reverse bias current would be relatively small as shown in Figure 5.6 (e). The rectifying characteristics of Schottky diode are similar to those of the *pn* junction diode.

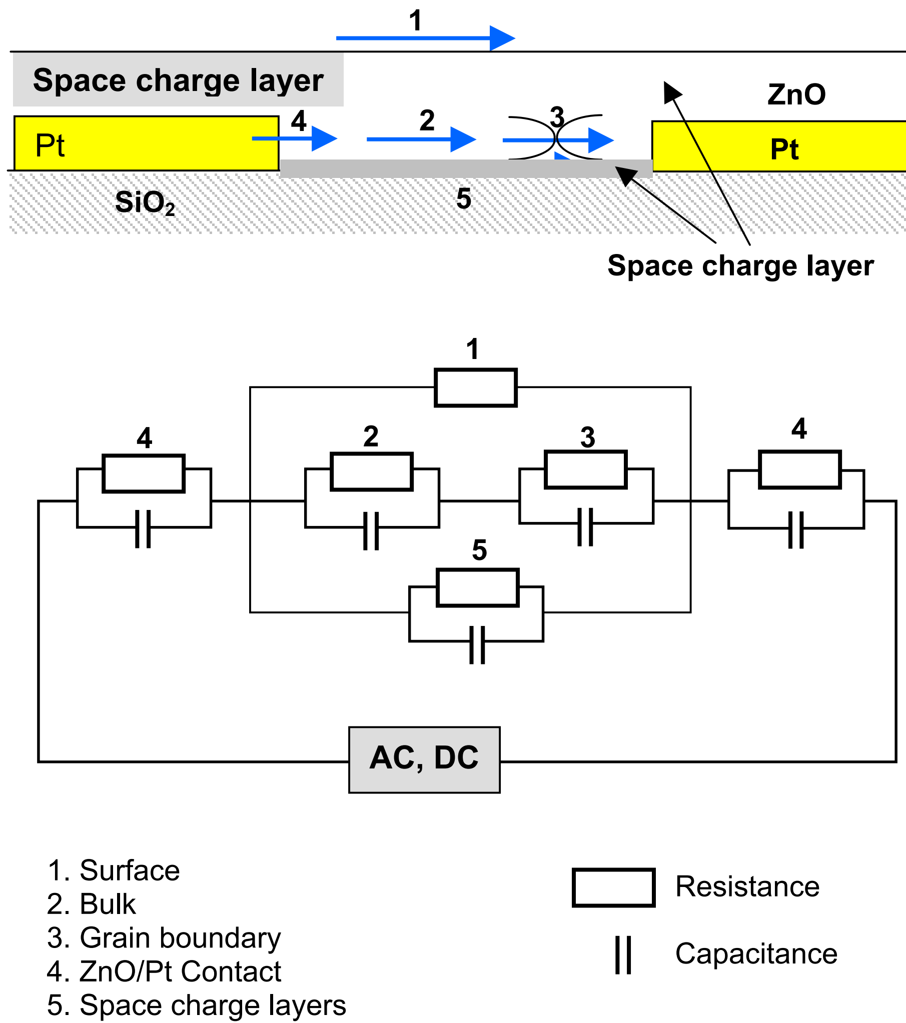

Figure 5.5 Schematic elementary contributions for current flow and equivalent circuits of ZnO thin films on micro array

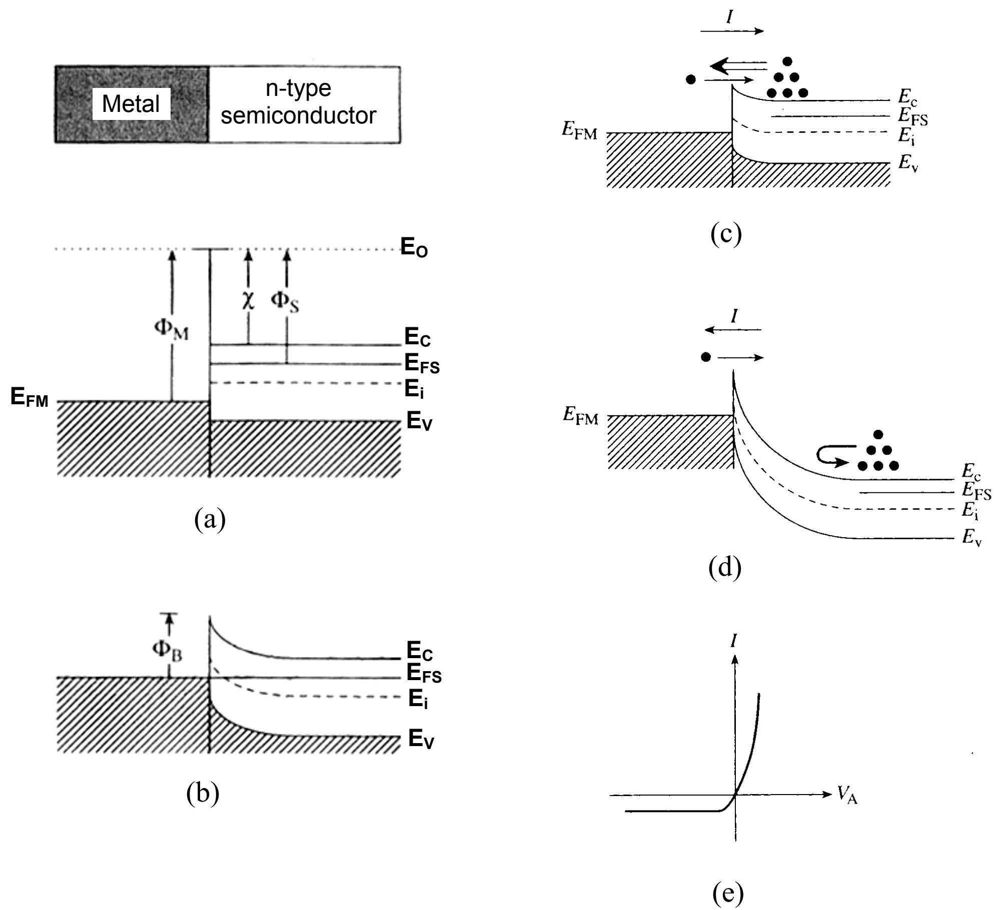

Figure 5.6 Energy band diagrams for ideal MS contacts between a metal and n-type semiconductor: $\Phi_M > \Phi_S$ system (a) an instant after contact formation, (b) under equilibrium condition, formed Schottky diode (c) Carrier activity when $V_A > 0$, (d) Carrier activity when $V_A < 0$ and (e) Deduced general form of the I-V characteristics [89].

Figure 5.7 represents the equivalent circuit of each sensor element with Schottky contacts at the two ZnO/Pt interfaces. Independent of the polarity of the applied voltage, one contact will always be in reverse bias thereby limiting the current to the reverse saturation current I_0 in the ideal case.

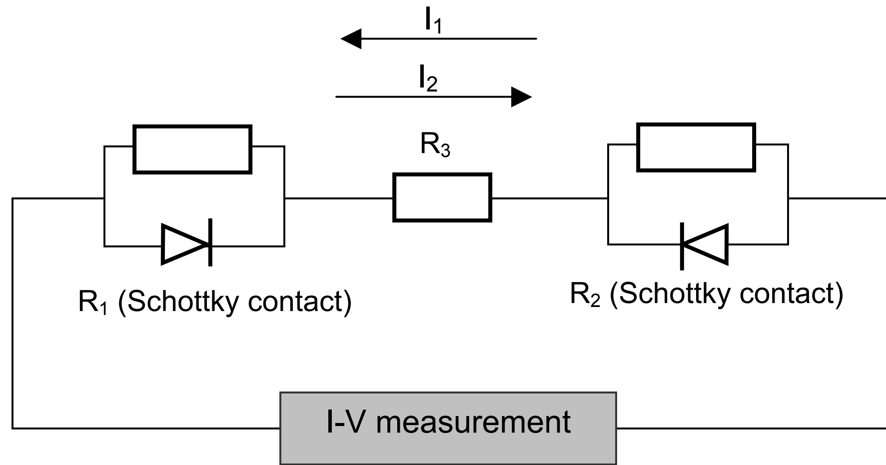

Figure 5.7 Simplified equivalent circuit of ZnO micro array sensors with buried Pt electrodes.

The back-to-back diode behavior of I-V curves measured for ZnO was also reported when Au electrodes were used as contacts [90]. Traversa et al reported that the I-V curves for ZnO pellets with two ohmic contacts were linear, and ZnO with two non-ohmic contacts had typical back-to-back diode behavior, while the I-V curves with one ohmic contact showed a diode behavior with rectifying character attributed to the presence of the Schottky barrier. Weimar et al [91] found, through two- and four-probe measurements, that the junction of Pt with SnO_2 formed a Schottky depletion layer, causing a large voltage drop at the contacts. This back-to-back diode behavior of SnO_2 film is consistent with the I-V characteristics obtained for the SnO_2 micro array examined in this study.

The capacitance derived from an evaluation of the peak frequency of the first semi-circle, ~5 pF, also suggests the existence of a depletion layer at the ZnO/Pt interface. The bulk capacitance is given by

$$C = \varepsilon\varepsilon_O \frac{A}{l} \tag{5.5}$$

with ε_o the permittivity in vacuum (8.854 x 10^{-14} F/cm) and ε the dielectric constant of ZnO (~8.75). Assuming the one ZnO sensing element as a capacitor with parallel electrodes in Figure 5.3, area (A) and length (l) will be 1.7125 x 10^{-6} cm^2 (width of ZnO

film (685 μm) x thickness of electrode (0.25 μm)) and 18 μm (distance between two interdigited electrodes), respectively, then one calculates:

$$C = 8.854\times10^{-14} F/cm \ \times 8.75\times\frac{1.7125\times10^{-6} cm^2}{18\times10^{-4} cm} = 7.37\times10^{-16} F \quad (5.6)$$

Since the ZnO micro array consisted of 17 sensing elements, the bulk capacitance will be around 1.25 x 10^{-14} F (1.25 x 10^{-2} pF). This calculated bulk capacitance is much below the magnitude of the measured capacitance (5 pF). Assuming a space charge width of 0.18 μm at the Schottky contact, one obtains a space charge capacitance of 1.25 pF, a value of the same order of magnitude as the measured value. It should, however, be noted that stray capacitances on the order of pF are not uncommon and that this alone should not eliminate the bulk resistance as the primary contributor to the impedance at high frequencies. This question is returned again below.

As reported in Chapter 4.2.3, a second semi-circle at reduced frequency (less than 10^3 Hz, 10^{-6} – 10^{-9} F) often appears after the application of a DC bias, with its diameter increasing with increasing bias. The second semi-circle at reduced frequencies is rarely reported, while the first semi-circle component has been frequently observed in the AC spectra of SnO_2 and ZnO sensors. Only one group [91] reported a second low frequency semi-circle when examining the impedance of SnO_2 thin films with interdigited Pt electrodes. They attributed this to the migration of charged particles (either surface species such as O_2^-, O^-, O^{2-} and OH^-, or bulk lattice species such as oxygen defects, V_O^{2+}). However, they did not perform any additional experiments or modeling to support their hypothesis.

In this study, in an attempt to identify the origin of the second semi-circle at reduced frequencies, the AC spectra was examined both with and without DC applied bias and following various pretreatments. As shown in Figure 4.26, 4.27 and 4.28, A DC bias applied during impedance measurements induces the formation of a second semi-circle but without much effect on the high frequency semi-circle, while bias pretreatment impacts both semi-circles. Figure 5.8 shows an equivalent circuit consistent with the observation of the two semi-circular components as well as a small offset of the semicircular elements from the origin of the impedance diagram. The resistance R_1 is attributed to a small parallel bulk and surface contributions to the total resistance (see 1 &

2 in Figure 5.5). R_2 and C_2 are attributed to the depletion layer at ZnO/Pt Schottky contact, and R_3 and C_3, either a DC bias induced depletion layer leading to a bias dependent constriction resistance or another interfacial structure such as the grain boundary with a bias dependent barrier height.

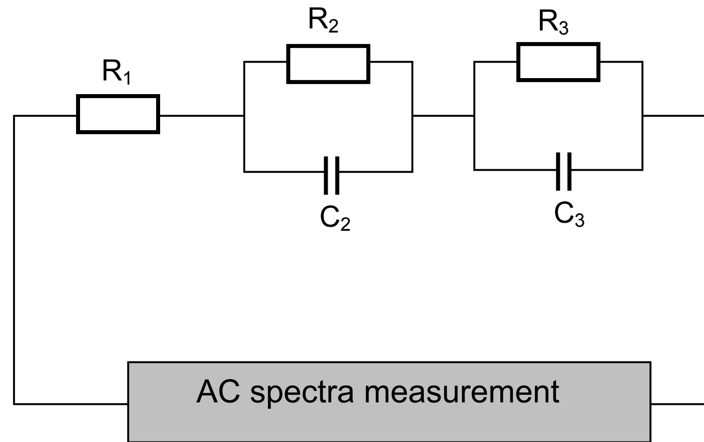

Figure 5.8 Equivalent circuits of ZnO micro array sensors with buried Pt electrodes during AC impedance spectra measurement.

First, considering the constriction resistance model, we refer to Figure 5.9. With near zero bias, the condition is as illustrated in Figure 5.9 (a). Here the Schottky contact resistance R_S dominates and is much larger than the film series resistance R_{ZnO}. Upon application of a large DC bias, the depletion width at the reverse biased junction increases as illustrated in Figure 5.9 (b). Also, the DC bias modifies the oxygen adsorption/desorption at the surface of each electrode regime. The oxygen adsorption reaction will be enhanced at one electrode while oxygen desorption will be enhanced at the other one. Thus, the former electrode regime will have enlarged depletion layer and this will act as constriction resistance. This voltage dependent constriction resistance could explain the generation and growth of the second semi circle under DC bias. At lower oxygen content (less than 0.01% O_2 in Ar), the second semi-circle is hardly observed, while it exists at higher oxygen content as shown in Figure 4.30. At a sufficiently low oxygen partial pressure, the constriction resistance will not be formed

since the number of adsorbed oxygen ions is inadequate to form a depletion layer with sufficient width. Due to the gradient in potential across the device, one could also imagine a corresponding gradient in the degree of oxygen adsorption on the surface. This will lead to the retention of a constriction resistance even after removal of the DC bias. This would also explain the observed hysteresis effects related to periodic field induced adsorption and desorption of surface oxygen, and the reduction in hysteresis at lower $p(O_2)$.

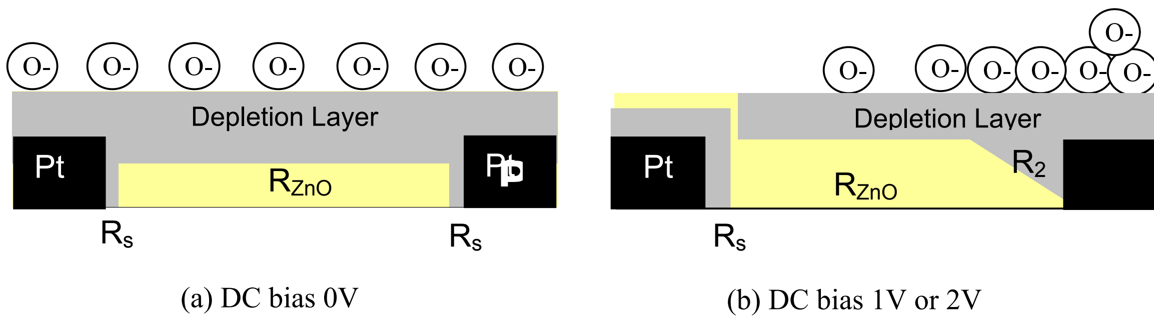

Figure 5.9 Model for DC bias effect on ZnO films: Depletion induced at reverse biased electrode on right combines with gas induced depletion layer from surface to form the constriction resistance R_2.

Several observed features are perhaps difficult to explain on this basis alone. First, the time constants associated with the growth and decay of the bias induced effects are on the order of hours. Gas adsorption/desorption is expected to be on a much shorter time scale. This feature is addressed again below when we discuss possible electromigration effects. Second, the capacitance associated with the low frequency semi-circle is very high (~ nF). At least a simple constriction resistance model would suggest a much lower capacitance.

Another possible explanation for the second low frequency semi-circle is a grain boundary contribution for which the grain boundary potential barrier height is dependent on the magnitude of the DC bias applied across it. Back to back barriers form at grain boundaries due to electrons from the adjacent grains being trapped at mid-gap states

localized at the grain boundaries. The barrier height Φ_B depends on the trapped charge density Q (Coul/cm^2), the dielectric constant ε, and the donor density N_D as

$$\Phi_B = \frac{-qQ^2}{8\varepsilon N_D} \tag{5.7}$$

If there is a high density of traps, upon application of the bias, electrons injected into the traps become trapped, given the high activation barrier for them to become detrapped once again. Thus, even following removal of the bias, the barrier Φ_B will, according to Eq. (5.7), increase.

This may be reflected in the growth of the low frequency semi-circle with applied DC bias. Upon removal of the bias, the electrons detrap at an emission rate, e given by

$$e \propto \exp(-\Delta E/kT) \tag{5.8}$$

where the proportionality constant includes contributions from the carrier cross section, mean thermal velocity, and effective density of states while ΔE represents the energy separation between the trap level and the carrier band [92]. The barrier, under these circumstances, should decay at the same rate. Figure 5.10 shows the modulation of grain boundary barriers by application of a DC bias [93]. As shown in Figure 5.10 (a), without bias, the system is in equilibrium as reflected in the flat Fermi level. Traps below the Fermi level are filled while traps above the Fermi level are empty, including the interface traps. Under applied bias, the occupancy of the interface states is disturbed and reflects the positions of the quasi-Fermi energies E_{F0} and E_{F1}. Thus, for example, during bias, the interface states between E_F and E_{F0} on the left hand side grain are filled. Immediately following removal of the bias, the grain boundary barrier is higher than under equilibrium conditions due to the increase in the number of filled traps at the interface, as shown in Figure 5.10 (c). With time, however, electrons occupying traps above E_F will be emitted to the conduction band, with the emission rate depending on the depth of the traps below the conduction band. This results in a reduction in the barrier height with time.

Such a model can also help explain the apparent difference in the transient response of the total impedance in Figure 4.39, region B, measured with and without the DC bias applied. First, under bias, we expect the resistance of the back-to-back diode to decrease and so the lower curve in region B is consequently lower in resistance. However, the

effective resistance of the barrier is much more strongly dependent on change in barrier height than the near zero bias component being monitored in the upper curve [94].

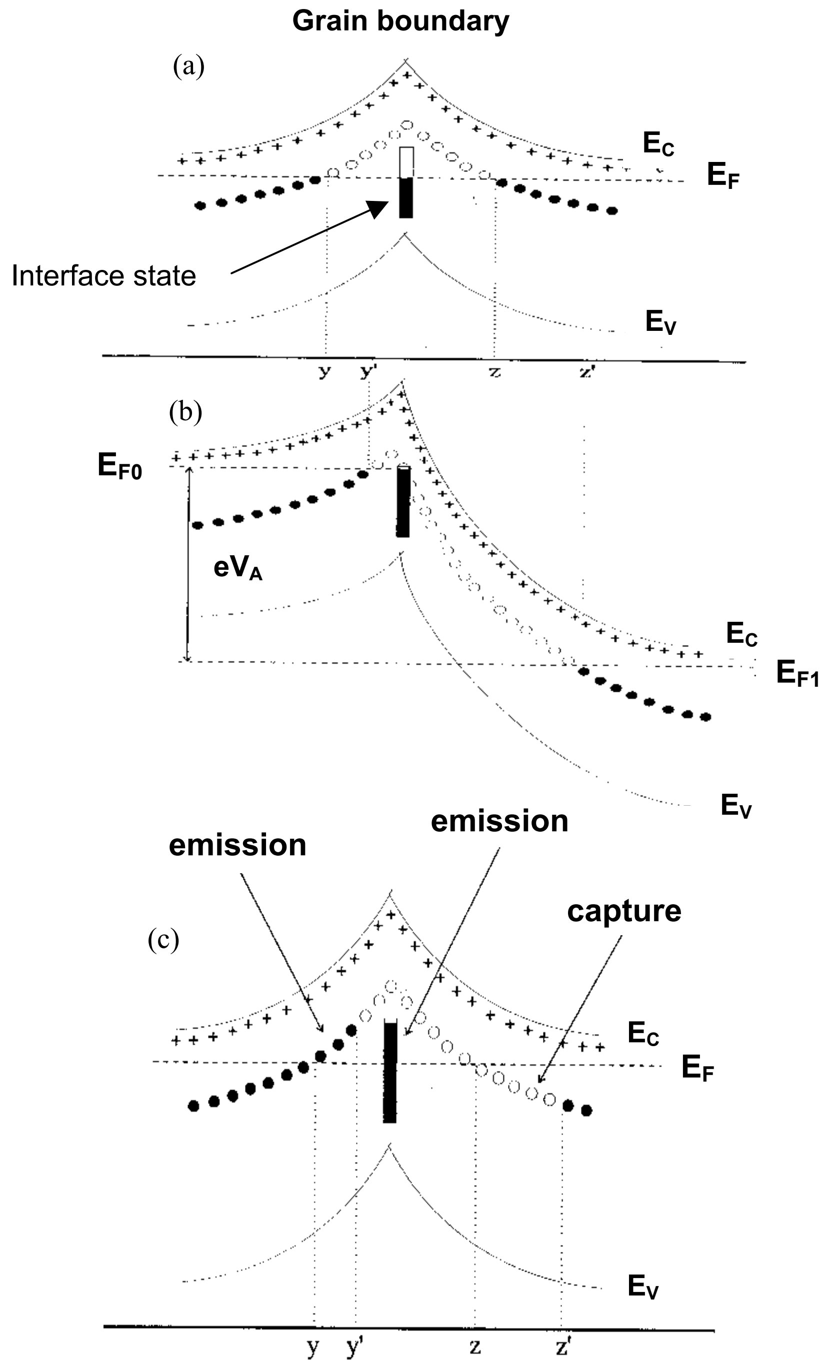

Figure 5.10 Modulation of grain boundary barrier by DC bias (a) Without bias, (b) Applying a DC bias, and (c) After removal of DC bias [93]

5.4 Time dependent sensor performance

The resistance drift of ZnO micro arrays has been observed during sensor operation. As shown in chapter 4.3, the drift is dependent on time and applied DC bias. These drift phenomena cannot be caused by degradation of the microstructure since the drift shows reversible behavior. Also, the modulation of the surface depletion layer by oxygen adsorption/desorption, the operating principle behind semiconducting gas sensors, cannot explain the observed results given that oxygen/desorption reaction is much more rapid than some of the transients observed in this study. For example, Figure 5.11 shows the typical gas response pattern of a commercial Figaro sensor when exposed to reducing gas, indicating sub-minute response time [95]. The response time of a CO sensor (TGS2440, thick film metal oxide semiconductor sensor) is roughly 35 seconds and the recovery of the sensor to 90% of the base level is within 150 seconds with exposure of 300 ppm CO.

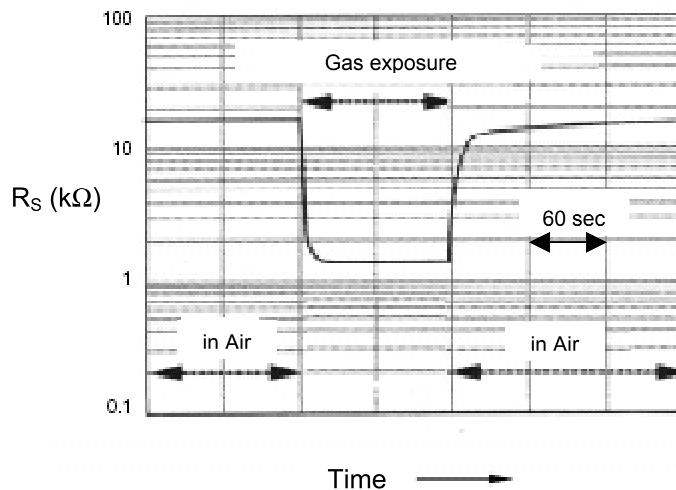

Figure 5.11 Typical sensor response of Figaro sensor [95]

Therefore, the long term resistance drift observed here is believed to be related to other processes which act to modify the electrical properties of ZnO sensors at the operating temperatures of 300 – 500 °C. When ZnO is exposed to an oxygen atmosphere, in general, three different reactions occur as shown in Figure 5.12. When ZnO is exposed to comparatively high oxygen pressure compared to the internal chemical potential of

oxygen, oxygen will be adsorbed on the surface and trap electrons, inducing a space charge region as;

$$\tfrac{1}{2}O_2 + 2e^- = O_S^{2-} \quad (5.9)$$

This adsorbed oxygen ion will transfer to the first lattice plane by exchange with an oxygen vacancy as;

$$O_S^{2-} + V_O^{\bullet\bullet} = O_O^X \quad (5.10)$$

Then, the oxygen will diffuse into the interior of the crystal or grain thereby bringing the material into equilibration with the atmosphere. During this *chemical diffusion*, charge neutrality is maintained by insuring that the oxygen ion migrates with the accompanying electron species. Thus, the oxygen migration into the ZnO film under oxidation serves to modify the electrical resistivity. Oxygen migration in ZnO is easily observed at elevated temperature (700 – 1000 °C). On a very long time scale, however, oxygen diffusion can occur even at the low temperature of sensor operation (300 – 500 °C) particularly along grain boundaries where diffusion is generally enhanced. Thus, if oxygen diffusion occurs to a certain extent during the sensor measurement, this will be a source of resistance drift.

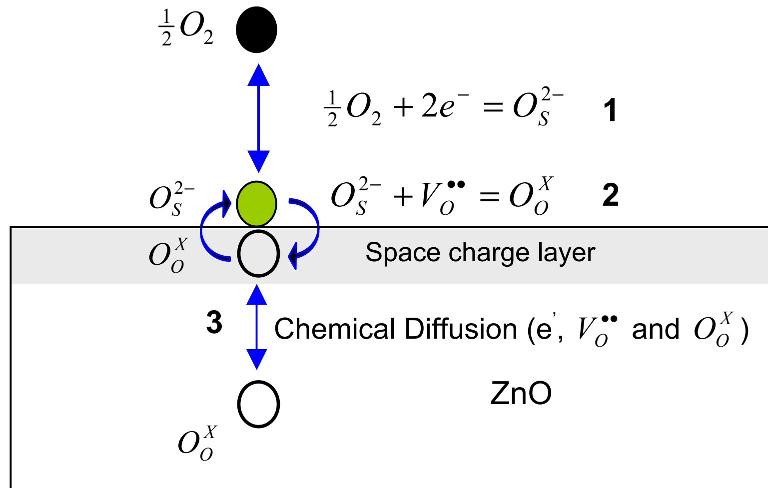

Figure 5.12 Response of ZnO with oxygen atmosphere with oxygen adsorption/desorption on surface (1), oxygen exchange on surface (2) and oxygen migration in ZnO (3)

As shown in Figure 4.33 and 4.35, the resistance shows the two distinctive transient behaviors induced by rapid changes in oxygen/argon mixtures. When ZnO is exposed to lower oxygen partial pressure, the resistance at first decreases nearly abruptly which is then followed by a slower drift of resistance on a time scale of hours. The source of the rapid response is expected to be due to the oxygen adsorption/desorption reactions on the surface of ZnO. The slow response is consistent with oxygen diffusion.

Resistance drift is rarely discussed since the majority of sensor research is focused on improving sensitivity. Two groups have reported on resistance drift behavior of SnO_2 sensors [96-99]. The Aldao group [96, 97] measured the resistance response of sintered SnO_2 upon exposure to an oxygen atmosphere from vacuum. It was observed that an immediate resistance change was followed by a slower drift of resistance even at temperatures of 200 – 300 °C. They proposed that oxygen diffusion into the grains was responsible for the slow drift process by affecting both the oxygen vacancy concentration and the Schottky barrier height.

The other group [98, 99] investigated the drift effect using a SnO_2 single crystal. They found that chemical diffusion of oxygen was sufficiently fast to cause the drift effect in SnO_2 sensors due to stoichiometry changes. According to the measured chemical diffusion coefficient ($D \sim 10^{-8}$ cm^2/sec at 500 °C), the stoichiometry of SnO_2 particles with sizes of 100 nm could be equilibrated in a few milliseconds [99]. Using numerical simulation with this diffusion coefficient, they estimated the characteristic time of the drift process and found that the estimated characteristic time was shorter than the actual characteristics times reported by Blaustein et al [97]. Thus, they suggested that the kinetics of the drift process in sensors were controlled by the surface exchange reaction rather than the chemical diffusion of oxygen.

For investigating the rate limiting step of the resistance drift in ZnO micro arrays, a one dimensional diffusion model is proposed as shown in Figure 5.13. When ZnO is exposed to the reducing environment, oxygen in ZnO will migrate to the surface (F_3). The diffused oxygen near the surface will transfer to the surface as adsorbed oxygen (F_2), and then desorb from the surface and diffuse into the reducing atmosphere (F_1). Oxygen migration will be proceed until the equilibrated stoichiometry of ZnO is attained. Figure 5.13 (a) shows the profile of oxygen concentration when steady state is reached. Usually,

the adsorption/desorption reaction of oxygen on surface is faster than the other two reactions.

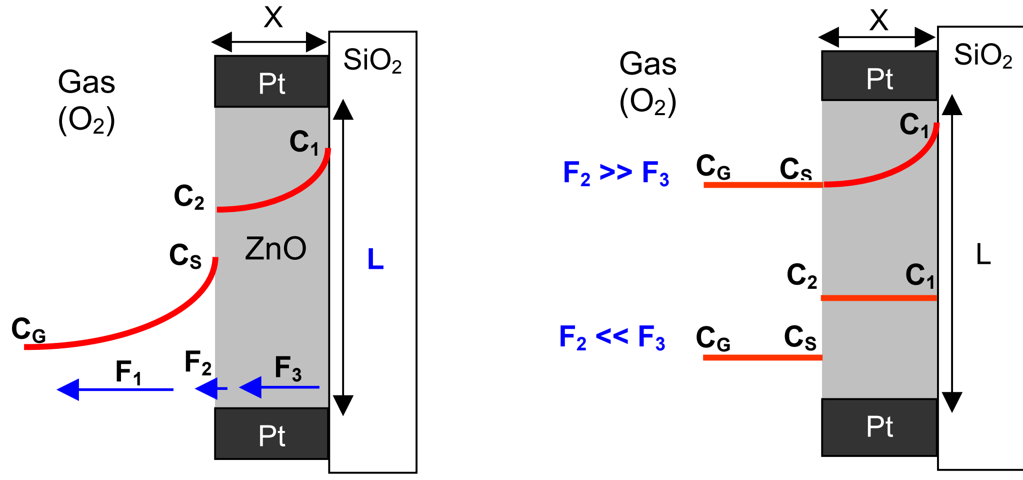

(a) When each reaction rate is similar, $F_1 \approx F_2 \approx F_3$

(b) When surface adsorption/desorption (F_1) is faster than the others and $F_2 > F_3$ or $F_2 < F_3$

$$F_1 = h_G(C_S - C_G)$$

$$F_2 = k_S C_2$$

$$F_3 = -D\frac{\partial C}{\partial x}$$

C_G = Concentration of oxygen in the bulk gas phase
C_S = Concentration of oxygen at the surface of ZnO in the gas phase
C_2 = Concentration of oxygen at the gas/ZnO interface in the ZnO
C_1 = Concentration of oxygen at the ZnO/SiO_2 interface in the ZnO

Figure 5.13 One dimensional diffusion model in reduction environment with the profile of oxygen concentrations

Assuming one of two reactions, surface exchange and diffusion, is the rate limiting step, the oxygen concentration will have different profiles as shown in Figure 5.13 (b). If the reaction rate is controlled by diffusion of oxygen inside the ZnO ($F_2 > F_3$), the concentrations of oxygen at the surface (C_S) and at the gas/ZnO interface (C_2) will be the same, and the oxygen concentration inside ZnO (C_1) will decay exponentially with diffusion length dependent on the oxygen diffusion coefficient. If the surface exchange reaction controls ($F_2 < F_3$), the oxygen concentrations in the ZnO film will be the same ($C_1 = C_2$). The concentration of oxygen on the interface (C_2) will be higher than that on

the surface (C_G), and the C_2 will decrease linearly with time. The resistance of ZnO is proportional to the oxygen concentration since the resistance is decreased decreases with the removal of oxygen, creating electrons and oxygen vacancies.

The resistance response of ZnO in Figure 4.35 exhibits two distinctive responses, an immediate response and a slower response. The slower response shows an almost linear drift behavior with time when ZnO is exposed to factor of 10 lower oxygen concentration (from 10% to 1%, 0.1% and 0.01%). It is suspected that the surface exchange reaction of ZnO would be the rate limiting step under reducing condition. However, the resistance drift of ZnO shown Figure 4.33 also exhibits an exponentially decay with time when ZnO is exposed to lower oxygen content atmosphere from air. For example, the resistance drift of ZnO in Ar from air initially shows an exponential decay. This means that the diffusion reaction would also participate in the reduction process as a rate limiting step. Thus, it is proposed that when the ZnO is abruptly exposed to a different atmosphere, e.g., from air to Ar or from air to 0.1% oxygen content, the resistance drift consists of two different rate limiting steps, i.e. surface exchange and diffusion. A detailed evaluation of the kinetics would require a more systematic measurement of the transient response upon change in $p(O_2)$.

The conductivity dependence on the oxygen partial pressure ($p(O_2)$) was also examined. The *n* value in equation (5.11) depends on the valence state of the defects and the nature of the defects dominant in the electroneutrality equation. For example, if the reduction reaction controls defect generation and the electron density is fixed by the number of oxygen vacancies formed, then the *m* value is 6 and 4 depending on whether the oxygen vacancies are doubly or singly charged.

$$\sigma \propto \exp\left(-\frac{E_R}{{}^{m}\!/_{2} \cdot kT}\right) \cdot P(O_2)^{-1/n} \tag{5.11}$$

The partial oxygen pressure dependence calculated in Figure 4.34 is around 1/2. This is much higher than 1/4 or 1/6. It is suspected that the oxygen adsorption/desorption on the surface strongly contribute to this low value of *n* at 420 °C since that of 4 and 6 are generally obtained associated with bulk phenomena at higher temperatures (700 – 1000 °C). At this high temperature region, diffusion and surface exchange of oxygen will be the predominant reactions since surface adsorbed oxygen tends to desorb around 560 °C

[28]. Seitz et al [11] reported a high partial oxygen pressure dependence of resistivity for undoped and indium doped ZnO with *n* values of ~ 2. They measured this value of *n* at 270 °C with a sintered ZnO pellet. The chemisorption of oxygen in the form, O^-, was believed to be responsible for this behavior. Considering the surface reaction involving O^-, oxygen adsorption reaction will be:

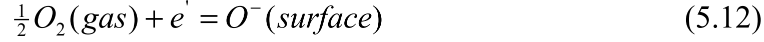

$$\tfrac{1}{2}O_2(gas) + e' = O^-(surface) \tag{5.12}$$

The equilibrium constant for the reaction is:

$$K_S = \frac{[O^-]}{P_{O_2}^{1/2} \cdot n} = K_S^O \cdot \exp\left(-\frac{E_S}{kT}\right) \tag{5.13}$$

Thus, the conductivity of ZnO, assuming near saturation of $[O^-]$ is:

$$\sigma \propto n \propto (K_S^O)^{-1} \cdot \exp\left(\frac{E_S}{kT}\right) \cdot P_{O_2}^{-1/2} \tag{5.14}$$

The oxygen partial pressure dependences in Figure 4.36 exhibit 1/3.2, 1/3.8 and 1/4.2 at the temperatures of 380 °C, 420 °C and 460 °C, respectively. In the experiment, ZnO (Ar:O_2 = 3:7) was exposed to reduced oxygen partial pressures continuously for 5 hours (from 10% to 1%, 0.1% and 0.01% O_2/Ar mixtures). The oxygen partial pressure dependence of about 1/4 can be related to the creation of single ionized oxygen vacancy via the bulk reaction as described in Chapter 2 or the chemisorption of oxygen in the form, O^{2-}. The surface reaction with O^{2-} will be:

$$\tfrac{1}{2}O_2(gas) + 2e' = O^{2-}(surface) \tag{5.15}$$

The equilibrium constant for the reaction is:

$$K_S = \frac{[O^{2-}]}{P_{O_2}^{1/2} \cdot n^2} = K_S^O \cdot \exp\left(-\frac{E_S}{kT}\right) \tag{5.16}$$

Thus, again assuming near saturation of $[O^{2-}]$, the conductivity of ZnO is:

$$\sigma \propto n \propto (K_S^O)^{-1} \cdot \exp\left(\frac{E_S}{2kT}\right) \cdot P_{O_2}^{-1/4} \tag{5.17}$$

However, experimental evidence suggests that the oxygen partial dependence cannot be explained by chemisorption of oxygen alone. Equation (5.14) and (5.17) are correct only after assuming that the surface is highly covered by oxygen, i.e., $[O^{2-}]$ and $[O^-]$ are remain essentially constant. This assumption, however, is not satisfied for conditions at

which the sensors were exposed to low oxygen partial pressures (e.g., 0.1 and 0.01% O_2 in Ar). Furthermore, it is difficult to see how the slow kinetics at these temperatures could be related to other than bulk controlled processes. Thus, the oxygen partial pressure dependence should be related to defect reactions involving oxygen vacancies and electrons as discussed in chapter 2.4.2. The source of the difference in the oxygen partial pressure dependences for the two compositions reported in Figure 4.34 and 4.36, however, remains unclear at this time and requires further study.

Figure 4.37 shows that an activation energy of about 1 eV characterizes the sensor response. This may include contributions from surface and bulk reactions. Seitz et al [11] examined the electrical response of surface and bulk component of undoped ZnO pellets. It was reported that the activation energies for bulk resistance is around 0.3 eV and boundary resistance is around 0.45 eV, respectively. Assuming that Eq. (5.11) applies, then the measured activation energy of 1 eV would correspond to $E_s/2$ or $E_s = 2$eV.

So far, time dependent resistance drift induced by changes in atmosphere has been discussed. Even though the temperatures of sensor operation are relatively low, oxygen chemical diffusion processes within the film do proceed but with an extended time scale. However, when a DC bias is applied to the ZnO micro array, time dependent resistance drift effects are again observed. Resistance drift in gas sensors induced by application of a DC bias has not been previously reported as far as I am aware. I discuss the DC bias effects on resistance drift and propose possible hypotheses to explain them.

With applying a DC bias, a resistance drift is induced even after completing a stabilization procedure for an extended time in air as shown in Figure 4.39 When the applied DC bias is removed, the resistance gradually decreases back to its original value. This indicates that the DC bias act as a driving force for reactions which serve to modify the electrical properties of ZnO. The resistance drift results in Figure 4.41 also support this assumption since the induced drift with 0.2V DC applied is much smaller than the drift induced by 1V DC. This time dependent DC bias effect is not limited to an air environment not only to ZnO. The SnO_2 micro array also exhibits the DC bias effects while, on the other hand, a CTO micro array exhibits only a very weak DC bias effect. This time dependent DC bias effect of ZnO was also observed in gas environments such as 100 ppm H_2 in air, 1% and 0.1% O_2 in Ar.

The applied DC bias creates high electric fields between the two interdigited electrodes even though the bias is only 1V. Considering the distance between the Pt electrodes (~20 μm), the 1V DC bias will induce an electric field equal to 0.5 kV/cm. This electric field is believed high enough to initiate various kinetic processes, e.g., migration of ions, which could serve to modify the resistance of ZnO.

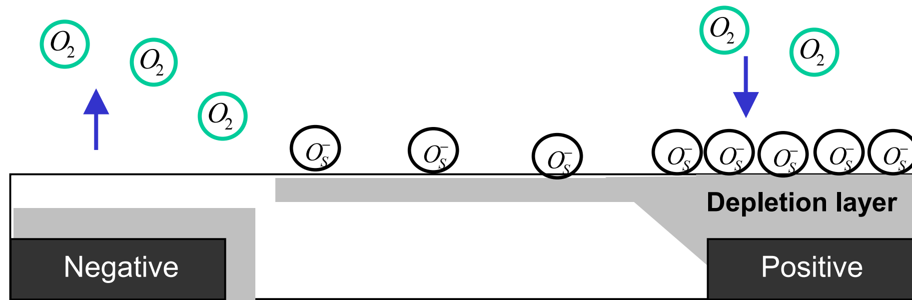

(a) After applying DC bias, t = 0

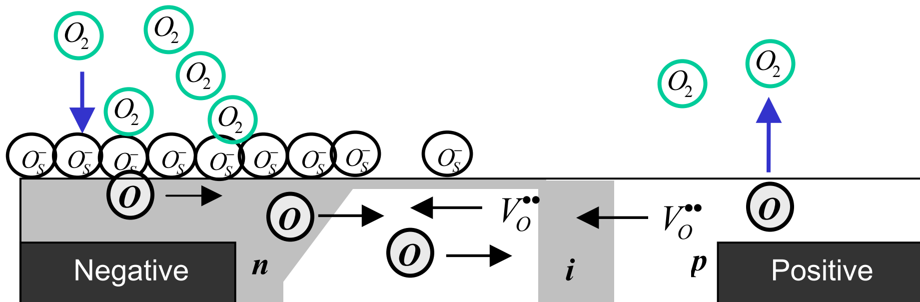

(b) After applying DC bias, $t = t_1$

Figure 5.14 Model for time dependent DC bias effect on the resistance of ZnO micro arrays: The constriction resistance R_2 will be increased with time since the DC bias would initiate the ion migration inside ZnO and will modify the electronic status of each electrode region.

In an attempt to explain the time dependent bias effect, we refer to Figure 5.14. As shown in Figure 5.14 (a), upon application of a bias, the enhanced depletion layer at the reverse biased junction and the surface space charge regime induced by oxygen adsorption at the surface form a constriction resistance, believed to be the source of the second semi circle. Also, the DC bias, creating a high electric field inside the ZnO, will

induce ion migration such as *by* $Zn_i^{\bullet\bullet}$ and $V_O^{\bullet\bullet}$. I already observed above that, even at the moderate temperatures of sensor operation, diffusion via ion migration proceeds within a reasonable time scale.

Therefore, on a time scale of hours, e.g., oxygen vacancies can be expected to migrate to the region with negative potential. The accumulated oxygen vacancies will enhance oxygen adsorption on the surface since they supply the electrons to the adsorbed oxygen as shown in Figure 5.14 (b) This, in turn, increases the space charge layer near the surface with the negative potential.

When the DC bias is removed, resistance relaxation is observed. This resistance drift can be related to the chemical diffusion of the migrated ions back to the equilibrium distribution. The time constant of this relaxation is calculated to be about 1.5 hours. Assuming the diffusion length as the distance between electrodes, the chemical diffusivity will be as below:

$$D = L^2 / t = (18\times10^{-4})^2 /(1.5\times3600) = 7\times10^{-10}\, cm^2 / \sec \qquad (5.18)$$

The estimated chemical diffusion coefficient of ZnO at 420 °C is even lower than that reported for that of SnO_2 at 500 °C (~10^{-8} cm^2/sec) [98].

Surface contact potential images in Figure 4.47 seem to support the DC bias-induced polarization effect. Even after two days passed following polarization by application of a 5V DC bias at 500 °C for 2 hours, each electrode regime exhibited a different surface contact potential. The regime with applied positive bias had a higher contact potential than that with negative bias. This suggests that the potential gradient is maintained due to a corresponding gradient in ion concentration.

Resistance changes induced by electromigration have been investigated by a number of researchers [100, 101]. Recent work by Rodewald et al demonstrated the use of spatially resolved microelectrodes to confirm and study electromigration effects in $SrTiO_3$. Figure 5.15 shows the spatial conductivity change of Fe doped $SrTiO_3$ by application of DC field (1 kV/cm for 90 min at 220 °C). Before application of a DC field, the Fe doped $SrTiO_3$ single crystal shows a uniform conductivity as represented in Figure 5.15 (c). However, after application of the DC bias, the conductivity takes on a distinctive conductivity profile. The profile consists of four characteristics regions: (1) an enhanced

conductivity region at the anode due to the accumulation of holes, (2) a sharp conductivity minimum due to the depletion of carriers, (3) a plateau that shows the conductivity of the sample before applying the DC bias, and (4) a region of sharp conductivity increase close to the cathode due to the accumulation of electrons. This suggests that applying DC field initiates the migration of oxygen vacancies. Similar studies are planned in the future on ZnO films to examine the role of electromigration in relation to field induced drift effects in sensors similar to the one studied here.

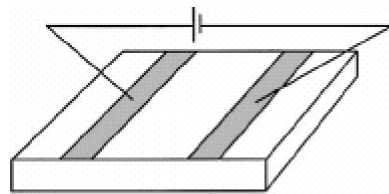

(a) Applied high field via two electrodes

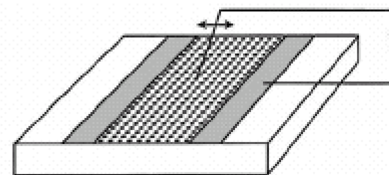

(b) Conductivity profile measurement

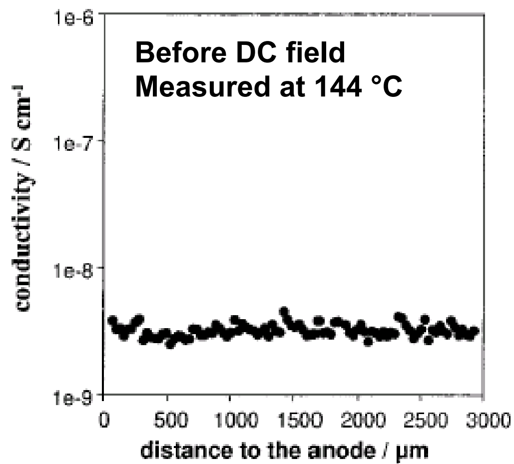

(c) Conductivity profile before applied field

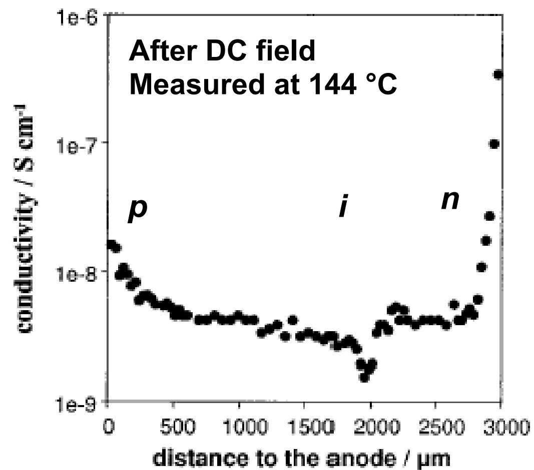

(d) Conductivity profile after applied field

Figure 5.15 Conductivity profile in a Fe doped $SrTiO_3$ single crystal obtained at 144 °C. Electric field (1 kV/cm) was applied via two electrodes for 90 min at 220 °C.

6. Conclusion and summary-key findings

In this study, the influence of thin film processing conditions and DC applied bias on the properties and gas sensing performance of sputtered ZnO micro array platforms has been investigated.

Reactive magnetron sputtering was used to deposit ZnO films by use of Zn target with controlled composition and microstructure. The thin film processing conditions such as O_2/Ar ratio, post annealing and Al dopants, influenced the physical and chemical properties of the ZnO films. The O_2/Ar ratio during sputtering impacted the stoichiometry as well as the microstructure and crystalline qualities of the undoped ZnO films. The undoped ZnO fabricated under higher oxygen partial pressures exhibited preferential c-axis orientation with more ideal crystalline structure and larger grain size due to the lowering in deposition rate. The slow deposition rate provides more time for Zn and O atoms to diffuse on the surface and to preferentially locate low energy sites in the crystal, resulting in enhanced crystalline structure and grain growth. These conditions also led to films with higher oxygen content Post deposition further enhanced crystalline quality and changed the stress induced in ZnO films from compressive to tensile. Little microstructural change was observed above 500ºC. This feature is important with regard to the elimination of one potential source of sensor aging.

Al doped ZnO films exhibited a mixed oriented crystalline structure as well as a much more porous microstructure with agglomerate shape of grains. This is believed to be due to migration of Al atoms toward the grain boundary, where they react with oxygen atoms and segregate as Al_2O_3. The segregated Al_2O_3 serves to prevent grain growth and the c-axis oriented structure of ZnO films.

ZnO micro arrays exhibited sensor response to various gases consistent with its n-type semiconducting behavior in both reducing and oxidizing atmosphere. Undoped ZnO films prepared with higher O_2/Ar ratio showed higher gas sensitivity than those with lower ratio. The ZnO with higher oxygen content had higher resistivity, implying a wider space charge layer induced by oxygen adsorption. Thus, the modulation of the space charge layer has a greater impact on the resistance of the ZnO films with buried electrodes, thereby exhibiting higher sensitivity. Even though undoped ZnO films annealed at 500 °C have higher resistance, they showed poor gas responses with unstable

baseline resistance. The annealing temperature of 500 °C was insufficient to stabilize the structure and composition of the undoped ZnO films while a 700°C anneal seemed to be sufficient in most cases.

Al doped ZnO films often exhibited superior sensor response even with much lower resistivities compared to undoped ZnO. The high sensitivity of Al doped ZnO is attributed to its porous microstructure. In Al doped ZnO, the gas can penetrate all the volume of the film with gas sensing reactions taking place at the surface of nearly all grains and grain boundaries, while, in the dense undoped ZnO films, the sensing reactions are restricted to the surface. Thus, Al doped ZnO films with porous microstructure have much higher sensitivity compared to the dense undoped ZnO films. The control of the film microstructure of sensor materials appears to be a more important factor than control of their stoichiometry. Thus, suggestions for improving the sensitivity of ZnO thin film gas sensors include: (1) introduce porous microstructure into the film, (2) increase oxygen content of the ZnO film, (3) increase annealing temperature, (4) dope ZnO with Al.

AC impedance measurements, both with and without DC bias, were utilized to assist in identifying the individual contributions to the sensor response. The AC spectra, in general, exhibited high and low frequency semi-circles, indicating that the resistance of the device is controlled or influenced by mainly two components. The sources of the first and second semi-circles are believed to be the Schottky contact at the ZnO/Pt interfaces and space charge induced constriction regions or grain boundary barriers, respectively. Both components respond to changes in gas environment.

The time dependent drift in resistance of ZnO films has been observed both with and without DC bias. Without apply bias, the ZnO micro array show a fast and slow response regime with both dependent on operating temperature. The resistance drift of the sensor response was shown to be related to a slow diffusion process upon variation in the O_2/Ar ratio during testing. Even though the temperature of thin film sensor operation is low, the bulk diffusion process still occurs but on a longer long-term scale. The oxygen partial pressure dependence and activation energy of sensor response were related to defect processes controlling the reduction/oxidation behavior of the ZnO. The controlling defect process appeared to be dependent on the processing history of the film.

In this study, time dependent DC bias effects on resistance drift are first reported. ZnO and SnO_2 micro arrays showed resistance drift induced by application of DC biases at the temperature of sensor operation in air, 100ppm H_2 and O_2/Ar atmosphere. However, Al doped ZnO and CTO showed considerably reduced resistance drift compared to undoped ZnO. The degree of drift was found to be proportional to the magnitude of the applied voltage. This resistance drift induced by DC bias is expected to contribute to the instability of thin film micro array sensors designed for practical application. The DC bias creates particularly high electric fields in these micro devices given that the spacing of the interdigited electrodes falls in range of microns. The high electric fields could initiate ion migration (e.g., oxygen vacancies) or modulate grain boundary barrier heights, inducing resistance drift with time. Possibly solutions for preventing the resistance drift induced by DC bias are to (1) lower the DC bias for measuring sensor response, (2) increase the spacing of the interdigited electrodes to reduce the electric field, and (3) lower the oxygen diffusivity by addition of appropriate dopants.

Technical implications:

- ZnO exhibits improved sensitivity to NO_2 – desirable in array
- Al doping provides improved sensitivity/stabilization
- Voltage induced aging effects identified in ZnO thin film sensor arrays are also important and relevant in SnO_2-based thin film sensor arrays.

7. Future work

The semiconducting thin film sensor is a promising candidate for sensor development given its sensitivity to many gases of interest and the ability to be integrated with MEMS and IC-based technology. However, the fundamental understanding of sensing properties of thin film sensor remains poor since an empirical optimization of sensor performance has focused on the use of simple DC resistance measurements. The effort to understand the sensor performance of ZnO thin film has been pursed using I-V characteristics and AC impedance spectra with or without DC biases. In this study, a strong induced DC bias resistance drift was discovered and investigated. While consistent models explaining the source of the field induced drift were propose, additional studies are required to define these processes more precisely. Suggested studies include (1) estimating the characteristics of ion migration using relaxation techniques and microelectrodes, (2) investigating the electrical profile between electrodes, (3) studying the role of grain boundary barriers, e.g., comparison between single crystal and polycrystal (4) in-diffusion studies to establish surface exchange and bulk/grain boundary diffusion as functions of composition and structure and (5) pursuing schemes to prevent or reduce the resistance drift induced by applied DC bias.

Reference:

1. P. T. Mosely and B. C. Tofield, Solid State Gas Sensor, Adam Hilger, Bristol and Philadelphia, 1987.
2. H. L. Tuller and R. Mlcak, *Advanced sensor technology based on oxide thin film-MEMS integration,* Journal of Electroceramics, **4 (**2000) p.415-425.
3. S. M. Sze, Semiconductor Sensors, John Wiley & Sons, New York, 1994.
4. National Research Council, Expanding the Vision of Sensor Materials, National Academy Press, 1995.
5. M. Jaegle, J. Wöllenstein, T. Meisinger, H. Böttner, G. Müller, T. Becker, C. Bosch-v. Braunmühl, *Micromachined thin film SnO_2 gas sensors in temperature pulsed operation mode*, Sensors and Actuators B, **57** (1999) p.130-134.
6. A. Pike and J. W. Gardner, *Thermal modeling and characterisation of micropower chemoresistive silicon sensors,* Sensors and Actuators B, **45** (1997) p.19-26.
7. G. Faglia, E.C., A. Cristalli, G. Sberveglieri and L. Dori, *Very low power consumption micromachined CO sensors,* Sensors and Actuators B, **55** (1999) p.140-146.
8. S. Semancik and R. Cavicchi, *Kinetically controlled chemical sensing using micromachined structures,* Account of Chemical Research, **31** (1998) p.279-287.
9. P. Esser and W. Göpel, *Physical adsorption on single crystal zinc oxide*, Surface Science, **97** (1980) p.309-318.
10. B. Bott, T. A. Jones and B. Mann, *The detection and measurement of CO using ZnO single crystals,* Sensors and Actuators, **5** (1984) p.65-73.
11. M. Seitz, F. Hampton, and W. Richmond, "Influence of chemisorbed oxygen on the ac electrical behavior of polycrystalline ZnO, Additives and Interfaces in Electronic Ceramics, Edited by M. F. Yan and A. H. Heuer, Cincinnati, Ohio, The American Ceramic Society (1982) p.60-70.
12. S. Pizzini, S. Pizzini, N. Butta, D. Narducci, M. Palladino, *Thick Film ZnO Resistive Gas Sensors,* Journal of Electrochemical Society, **136** (1989) p.1945-1948.
13. G. S. T. Rao and D. T. Rao, *Gas sensitivity of ZnO based thick film sensor to NH_3 at room temperature,* Sensors and Actuators B, **55** (1999) p.166-169.

14. H. Nanto, H. Sokooshi and T. Kawai, *Aluminum-doped ZnO thin film gas sensor capable of detecting freshness of seafoods,* Sensors and Actuators B, **13-14** (1993) p.715-717.
15. P. Mitra, A. P. Chatterjee, and H. S. Maiti, *ZnO thin film sensor,* Materials Letters, **35** (1998) p.33-38.
16. I. Stambolova, K. konstantinov, S. Vassilev, P. Peshev, and Ts. Tsacheva, *Lanthanum doped SnO_2 and ZnO thin films sensitive to ethanol and humidity,* Materials Chemistry and Physics, **63** (2000) p.104-108.
17. M. H. Huang, S. Mao, H. Feick, H. Yan, Y. Wu, H. Kind, E. Weber, R. Russo, and P. Yang, *Room-temperature ultraviolet nanowire nanolasers*, Science, **292** (2001) p.1897-1899.
18. R. P. Ried, E. Kim, D. M. Hong and R. S. Muller, *Piezoelectric microphone with on-chip CMOS circuits, Journal of Microelectromechanical Systems*, **2** (1993) p.111-120.
19. Y. Ito, K. Kushida, K. Sugawara and H. Takeuchi, *A 100-Mhz ultrasonic transducer array using ZnO thin films*, IEEE Transaction on Ultrasonics, Ferroelectrics, and Frequency Control, **42** (1995) p.316-323.
20. G. Sberveglieri, *Recent developments in semiconducting thin film gas sensor,* Sensors and Actuators B, **23** (1995) p.103-109.
21. N. Barsan and U. Weimar, *Conduction model of metal oxide gas sensors,* Journal of Electroceramics, **7** (2001) p.143-167.
22. Y. Chiang, D. P. Birnie, III and W. D. Kingery, Physical Ceramics; Principles for Ceramic Science and Engineering, John Wiley & Sons, Inc., 1997.
23. V. Guidi, M.C.C., M. Ferroni, G. Martinelli, L. Paglialonga, E. Comini and G. Sberveglieri, *Preparation of nanosized titania thick and thin film as gas sensors,* Sensors and Actuators B, **57** (1999) p.197-200.
24. M. Fleischer and H. Meixner, *Fast gas sensors based on metal oxides which are stable at high temperature,* Sensors and Actuators B, **43** (1997) p.1-10.
25. M. Fleischer, M. Seth, C. -D. Kohl and H. Meixner, *A selective H2 sensor implemented using Ga2O3 thin films which are covered with a gas-filtering SiO2 layer,* Sensors and Actuators B, **35-36** (1996) p.297-302.

26. P. Keller, H. Ferkel, K. Zweiacker, J. Naser, J. -U. Meyer and W. Riehemann, *The application of nanocrystalline BaTiO3-composite films as CO-sensing layers,* Sensors and Actuators B, **57** (1999) p.39-46.
27. J. Gerblinger and H. Meixner, *Electrical conductivity of sputtered films of strontium titanate*, Journal of Applied Physics, **67** (1990) p.7453-7459.
28. N. Yamazoe, J. Fuchigami, M. Kishikawa and T. Seiyama, *Interactions of tin oxide surface with O_2, H_2O, and H_2,* Surface Science, **86** (1979) p.335-344.
29. M. J. Madou and S. R. Morrison, Chemical sensing with solid state devices, Academic Press, Inc., London, 1989.
30. W. Göpel and K. D. Schierbaum, *SnO2 sensors: current status and future prospect,* Sensors and Actuators B, **26-27** (1995) p.1-12.
31. Y. Shimizu and M. Egashira, *Basic Aspects and challenges of semiconductor gas sensor,* MRS Bulletin, **6** (1999) p.18-24.
32. J. Wöllenstein, G. Plescher, G. Kuhner, H. Böttner, D. Niemeyer, and D. E. Williams, *Preparation, morphology and gas sensing behavior of $Cr_{2-x}Ti_xO_{3+Z}$ thin-films on standard silicon wafer,* IEEE Sensors Journal, **2** (2002) p.403-408.
33. D. Niemeyer, D. E. Williams, P. Smith, K. F. E. Pratt, B. Slater, C. Richard A. Catlow and A. M. Stoneham, *Experimental and computational study of the gas-sensor behavior and surface chemistry of the solid-solution $Cr_{2-x}Ti_xO_3$ ($x < 0.5$).* Journal of Materials Chemistry, **12** (2002) p.667-675.
34. V. Jayaraman, K. I. Gnanasekar, E. Prabhu, T. Gnanasekaran, and G. Periaswami, *Preparation and characterisation of $Cr_{2-x}Ti_xO_{3+d}$ and its sensor properties,* Sensors and Actuators B, **55** (1999) p.175-179.
35. A. Mandelis and C. Christofides, Physics, Chemistry and Technology of Solid State Gas Sensor Devices, John Wiley & Sons, Inc., New York, 1993.
36. P. Nelli, G. Falia, G. Sbervglieri, E. Cereda, G. Gabetta, A. Dieguez, A. Romano-Rodriguez, and J. R. Morante, *The aging effect on SnO2-Au thin film sensors: electrical and structural characterization*, Thin Solid Films, **371** (2000) p.249-253.

37. F. Lu, Y. Liu, M. Dong, and X. Wang, *Nanosized tin oxide as the novel material with simultaneous detection towards CO, H2 and CH4*, Sensors and Actuators B, **66** (2000) p.225-227.
38. J. Wöllenstein, J. A. Plaza, C. Cané, Y. Min, H. Böttner, H. L. Tuller, *A novel single chip thin film metal oxide array*, Sensors and Actuators B, **93** (2003) p.350-355.
39. M. Komatsu, N. Ohashi, I. Sakaguchi, S. Hishita, and H. Haneda, *Ga, N solubility limit in co-implanted ZnO measured by secondary ion mass spectrometry,* Applied Surface Science, **189** (2002) p.349-352.
40. S. Tuzemen, G. Xiong, J. Wilkinson, B. Mischuck, K. B. Ucer, and R. T. Williams, *Production and properties of p-n junctions in reactively sputtered ZnO,* Physica B, **308-310** (2001) p.1197-1200.
41. Y. R. Ryu, W. J. Kim, and H. W. White, *Fabrication of homostructural ZnO p-n junctions.* Journal of Crystal growth, **219** (2000) p.419-422.
42. A. E. McHale et al, Phase Equilibria Diagrams; Volume XII Oxides, The American Ceramic Society, Ohio, 1996.
43. T. B. Massalski, Binary Alloy Phase Diagrams; Volume 3, 2nd edition, ASM International, Ohio, 1990.
44. H. E. Brown, Zinc oxide; Properties and applications, International Lead Zinc Research Organization, Inc., New York, 1976.
45. http://www.elsevier.com/mrwclus/15/show/Main.htt, Encyclopedia of materials.
46. R. J. Brook, Concise Encyclopedia of Advanced Ceramic Materials, The MIT Press, Massachusetts, USA, 1991.
47. C. H. P Lupis, Chemical Thermodynamics of Materials, Prentice Hall, Singapore, 1993.
48. F. Seitz and D. Turnbull, Solid State Physics, Academic Press, United Kingdom, 1959.
49. G. W. Tomline, J. L. Routbort and T. O. Mason, *Oxygen diffusion in single-crystal zinc oxide*, Journal of American Ceramic Society, **81** (1998) p.869-876.
50. K. Ellmer, *Magnetron sputtering of transparent conductive zinc oxide: relation between the sputtering parameters and the electronic properties*, Journal of Physics D: Applied Physics, **33** (2000) p.R17-R32.

51. Y. Lee, Y. Kim and H. Kim, *Thickness dependence of microstructural evolution of ZnO films deposited by rf magnetron sputtering*, Journal of Materials Research, **13** (1998) p.1260-1265.
52. K. Chou and G. Liu, *Effects of excess zinc on the structure of reactively sputtered zinc oxide films*, Materials Chemistry and Physics, **37** (1994) p156-160.
53. Y. Zhang et al, *Crystal growth of undoped ZnO films on Si substrates under different sputtering conditions*, Journal of Crystal Growth, **243** (2003) p.439-443.
54. S. Maniv, W. D. Westwood and E. Colombini, *Pressure and angle of incidence effects in reactive planar magnetron sputtered ZnO layers*, Journal of Vacuum Science and Technology, **20** (1982) p.162-170.
55. S. Zhu, C. Su, S L. Lehoczky, P. Peters and M. A. George, *Pressure effects in ZnO films using off-axis sputtering deposition*, Journal of Crystal Growth, **211** (2000) p.106-110.
56. A. Barker, S. Crowther and D. Rees, *Room-temperature r.f. magnetron sputtered ZnO for electromechanical devices*, Sensors and Actuators A, **58** (1997) p.229-235.
57. S. Zhu, C. Su, S L. Lehoczky, P. Peters, M. A. George and D. H. Lowndes, *Surface texture and structure of ZnO films synthesized by off-axis sputtering deposition*, Journal of Materials Research, **15** (2000) p.1125-1130.
58. T. K. Subramanyam, B. S. Naidu and S. Uthanna, *Effect of substrate temperature on the physical properties of DC reactive magnetron sputtered ZnO films*, Optical Materials, **13** (1999) p.239-247.
59. Y. Yoshino, K. Inoue, M. Takeuchi, T. Makino, Y. Katayama and T. Hata, *Effect of substrate surface morphology and interface microstructure in ZnO thin films formed on various substrates*, Vacuum, **59** (2000) p.403-410.
60. V. Gupta and A. Mansingh, *Influence of postdeposition annealing on the structural and optical properties of sputtered zinc oxide film*, Journal of Applied Physics, **80** (1996) p.1063-1073.
61. Margie K. Reser, Phase Diagrams for Ceramists, 5th edition, The American Ceramic Society, Ohio, 1985.

62. T. Tsuji and M. Hirohashi, *Influence of oxygen partial pressure on transparency and conductivity of RF sputtered Al doped ZnO thin films*, Applied Surface Science, **157** (2000) p.47-51.

63. X. Q. Meng, W. Zhen, J. P. Guo and X. J. Fan, *Structural, optical and electrical properties of ZnO and ZnO-*Al_2O_3 *films prepared by dc magnetron sputtering*, Applied Physics A, **70** (2000) p.421-424.

64. I. Sieber, N. Wanderka, I. Urban, I. Dorfel, E. Schierhorn, F. Fenske and W. Fuhs, *Electron microscopic characterization of reactively sputtered ZnO films with different Al –doping levels*, Thin Solid Films, **330** (1998) p.108-113.

65. F. Haug, Zs. Geller, H. Zogg, A. N. Tiwari and C. Vignali, *Influence of deposition conditions on the thermal stability of ZnO:Al films grown by rf magnetron sputtering*, Journal of Vacuum Science and Technology A, **19** (2001) p.171-174.

66. T. K. Subramanyam, B. S. Naidu and S. Uthanna, *Physical properties of zinc oxide films prepared by dc reactive magnetron sputtering at different sputtering pressure*, Crystal Research Technology, **35** (2000) p.1193-1202.

67. F. S. Mahmood, R. D. Gould, A. K. Hassan and H. M. Salih, *DC properties of ZnO thin films prepared by rf magnetron sputtering*, Thin Solid Films, **270** (1995) p.376-379.

68. D. C. Look, J. W. Hemsky and J. R. Sizelove, *Residual native shallow donor in ZnO*, Physical Review Letters, **82** (1999) p.2552-2555.

69. G. Heiland, *Homogeneous semiconducting gas sensors*, Sensors and Actuators, **2** (1982) p.343-361.

70. L. F. Dong, Z. L. Cui and Z. K. Zhang, *Gas sensing properties of nano-ZnO prepared by arc plasma method,* NanoStructured Materials, **8** (1997) p.815-823.

71. J. Xu, Q. Pan, Y. Shun, and Z. Tian, *Grain size control and gas sensing properties of ZnO gas sensor,* Sensors and Actuators B, **66** (2000) p.277-279.

72. J. F. Chang, H. H. Kuo, I. C. Leu and M. H. Hon, *The effects of thickness and operation temperature on ZnO:Al thin film CO gas sensor*, Sensors and Actuators B, **84** (2002) p.258-264.

73. S. Basu, and A. Dutta, *Room temperature hydrogen sensors based on ZnO,* Materials Chemistry and Physics, **47** (1997) p.93-96.

74. H. Nanto, H. Sokooshi, and T. Usuda, *Smell sensor using aluminum-doped zinc oxide thin film prepared by sputtering technique,* Sensors and Actuators B, **10** (1993) p.79-83.
75. H. Nanto, T. Minami, and S. Takata, *Zinc oxide thin film ammonia gas sensors with high sensitivity and excellent selectivity,* Journal of Applied Physics, **60** (1986) p. 482-484.
76. A. K. Mukhopadhyay, P. Mitra, D. Chattopadhyay, and H. S. Maiti, *Influences of fabrication techniques and doping on hydrogen sensitivity of Zinc oxide sensors,* Journal of Materials. Science Letter, **15** (1996) p. 431-433.
77. H. Nanto, T., Morita, H. Habara, K. Kondo, Y. Douguchi, and T. Minami, *Doping effect of* SnO_2 *on gas sensing characteristics of sputtered ZnO thin film chemical sensor,* Sensors and Actuators B, **35-36** (1996) p.384-387.
78. N. J. Dayan, S. R. Sainkar, R. N. Karekar, and R. C. Aiyer, *A thick film hydrogen sensor based on a ZnO:* MoO_3 *formulation.* Materials Science and Technology, **9** (1998) p.360-364.
79. N. J. Dayan, S. R. Sainkar, R. N. Karekar and R. C. Aiyer, *Formulation and characterization of ZnO:Sb thick-film gas sensors,* Thin Solid Films, **325** (1998) p. 254-258.
80. K. Inoue and M. Miyayama, *Chlorine gas sensing properties of ZnO-CaO ceramics,* Journal of Electroceramics, **2** (1998) p.41-48.
81. A. Jones, T. A. Jones, B. Mann and J. G. Firth, *The effect of the physical form of the oxide on the conductivity changes produced by* CH_4*, CO, and* H_2O *on ZnO*, Sensor and Actuators, **5** (1984) p.75-88.
82. J. Wöllenstein, M. Scheulin, M. Jaegle, H. Böttner, *Gas-sensitive characteristics and morphology of reactive evaporated* V_2O_5 *thin films*, Proceedings of Eurosensors (2000) p.101-102.
83. H. Endres, H. D. jander, and W. Gottler "*A test system for gas sensors*." Sensors and Actuators B, **23** (1995) p.163-172.
84. B. D. Cullity, Elements of X-Ray Diffraction, 2nd edition, Addison-Wesley Publishing Company, Inc., US, 1978.

85. F. M. Serry, K. Kjoller, J. T. Thornton, R. J. Tench, and D. Cook, Electric force microscopy, surface potential imaging, and surface electric modification with the atomic force microscope (AFM), the website of Digital Instruments (www.veeco.com).
86. J. Fleig, *The influence of non-ideal microstructures on the analysis of grain boundary impedances*, Solid State Ionics, **131** (2000) p.117-127.
87. H. L. Tuller, *Ionic conduction in nanocrystalline materials*, Solid State Ionics, **131** (2000) p.143-157.
88. Y. Min, H. L. Tuller, S. Palzer, J. Wöllenstein, H. Böttner, *Gas response of reactively sputtered ZnO films on Si-based micro-array*, Sensors and Actuators B, **93** (2003) p. 435-441.
89. R. F. Pierret, Semiconductor Device Fundamentals, Addison-Wesley Publishing Company, Inc., United State of America, 1996.
90. E. Traversa and A. Bearzotti, *A novel humidity-detection mechanism for ZnO dense pellets*, Sensors and Actuators B, **23** (1995) p.181-186.
91. U. Weimar and W. Göpel, *A.c. measurements on tine oxide sensors to improve selectivities and sensitivities*, Sensors and Actuators B, **26-27** (1995) p.13-18.
92. D. V. Lang. *Deep Level Transient Spectroscopy: A New Method to Characterize Traps in Semiconductor*, Journal of Applied Physics, **45** (1974) p.3023.
93. Tomas D Chen, “Electrically Active Defects in Zinc Oxide”, Master Thesis, MIT, 1996.
94. A Rothschild, unpublished, personal communication.
95. http://www.figarosensor.com, Figaro Sensor Company.
96. M. S. Castro and C. M. Aldao, *Effects of sintering temperature on the oxygen adsorption in ZnO ceramics*, Journal of the European Ceramic Society, **19** (1999), p.511-515.
97. G. Blaustein, M.S. Castro and C. M. Aldao, *Influence of frozen distributions of oxygen vacancies on tin oxide conductance,* Sensors and Actuators B, **55** (1999) p.33-37.
98. B. Kamp, R. Merkle and J. Maier, *Chemical diffusion of oxygen in tin dioxide*, Sensors and Actuators B, **77** (2001) p.534-542.

99. J, Jamnik, B. Kamp, R. Merkle and J. Maier, *Space charge influenced oxygen incorporation in oxides: in how far does it contribute to the drift of Taguchi sensors*?, Solid State Ionics, **150** (2002) p.157-166.
100. S. Rodewald, J. Fleig, and J. Maier, *Resistance degradation of iron-doped strontium titanate investigated by spatially resolved conductivity measurement*, Journal of Ceramic Society, **83** (2000) p.1969-1976.
101. S. Rodewald, N. Sakai, K. Yamaji, H. Yokokawa, J. Fleig, and J. Maier, *The effect of the oxygen exchange at electrodes on the high-voltage electrocoloration of Fe-doped $SrTiO_3$ single crystals: A combined SIMS and microelectrode impedance study*, Journal of Electroceramics, **7** (2001) p.95-105.